Università degli Studi di Firenze
Scuola di Ingegneria
DIEF - Department of Industrial Engineering of Florence

PhD School: *Energetica e Tecnologie Industriali ed Ambientali Innovative*
Scientific Area: ING-IND/08 - *Macchine a Fluido*

Numerical modelling of partially premixed low-swirl flames for aero-engine applications

PhD Candidate: Ing. Leonardo Langone

Tutor: Prof. Ing. Antonio Andreini

CoTutor: Prof. Ing. Bruno Facchini

PhD School Coordinator: Prof. Ing. Giovanni Ferrara

XXXIV PhD School Cycle - 2018-2021

Università degli Studi di Firenze
Scuola di Ingegneria
DIEF - Department of Industrial Engineering of Florence

PhD School: *Energetica e Tecnologie Industriali ed Ambientali Innovative*
Scientific Area: ING-IND/08 - *Macchine a Fluido*

Numerical modelling of partially premixed low-swirl flames for aero-engine applications

PhD Candidate: Ing. Leonardo Langone

Tutor: Prof. Ing. Antonio Andreini

CoTutor: Prof. Ing. Bruno Facchini

PhD School Coordinator: Prof. Ing. Giovanni Ferrara

XXXIV PhD School Cycle - 2018-2021

To my family,

Acknowledgements

Before starting my dissertation, I would like to express my gratitude to Prof. Antonio Andreini and Prof. Bruno Facchini for offering me the possibility to give my contribution in this exciting research field and for allowing me to participate to the European Project and many other activities. I would like to thank especially Prof. Andreini for the coordination of the work and technical advice received in many discussions we had throughout these years. Then, I also would like to thank all the partners and the people involved in the CHAiRLIFT project for their scientific support and for all the things I learnt during this activity. Above all, I would thank all the academic partners for the work together regardless the difficulties of the COVID pandemic. The value of this experience is really invaluable. Last but not least, I would like to thank and wish all the best for all the other Ph.D. students and researchers in this project: Diego, Sven, Mohamed, Sara and Donato. I really hope to meet you guys again in future for new inspiring works such this!.

Abstract

The development of innovative aero-engine combustors has been devoted to drastically reducing pollutants emissions and improving engine performances in recent years. These aspects are not only crucial to meet the severe regulations imposed by ICAO-CAEP, but also to enable potential new engine architectures. Especially considering Nitrogen Oxidizes (NO_x) emissions, the most promising concept carried out so far is represented by Lean burn combustors, which however introduce several challenges in terms of flame stability.

A possible solution to this problem is the novel burner concept proposed in the EU project CHAiRLIFT (Compact Helical Arranged combustoRs with lean LIFTed flames). The proposal of this project sees the employment of low-swirl ultra-lean spray lifted flame with an inclined disposition of the burners. Both these concepts have been investigated separately at the Karlsruhe Institute of Technology (KIT). In particular, this type of flame has shown superior performances in terms of NO_x emissions a good resistance to Lean Blow-Off (LBO) occurrences, while avoiding flashback risks. The inclined arrangement of the burners, instead, establishes a macro-recirculation in the combustion chamber responsible for the transport of vitiated gas among the burners, promoting flame stability. Moreover, it contributes to reduce the need of cooling air and the overall weight. This ambitious project indeed requires proper tools to study flame interaction between adjacent burners in deep.

The present research effort is therefore devoted to numerically investigating the CHAiRLIFT concept through Computational Fluid Dynamics

(CFD) simulations. With this goal, both Scale Resolved (SR) simulations of the low-swirl burner in single sector configuration and Reynolds Averaged Navier-Stokes (RANS) simulations of the multiburner rig, currently under investigation at KIT, have been employed.

The numerical study of the multiburner configuration had a twofold objective: assess the numerical approach with the available data and support the experimental investigations, especially concerning the sensitivity to the tilt angle. The outcomes have shown that, in non-preheated conditions, the numerical simulation can fairly reproduce the spray lifted flames with a reasonable computational effort. Also, it points out that the best setup in terms of tilt angle for maximizing the exhausts recirculation lays between 20 and 30 degrees, which is a lower value concerning the original experimental investigation with high-swrirl flames.

Another point to be addressed is the turbulent combustion modelling in preheated conditions, which has shown to be more challenging from the modelling point of view. To this aim, the investigation is focused on the same burner in single sector configuration, operated with gaseous fuel. State-of-the-art numerical models for Large Eddy Simulations context are employed to understand how the flame is reproduced. The results highlighted that both the Flamelet Generated Manifold (FGM) approach and a modified version taking into account the stretch and heat loss effects are mispredicting the flame lift-off height. Instead, a good reproduction is achieved with the Thickened Flame (TF) model. Despite the good agreement of the latter approach, this suffers of some disadvantages in terms of chemistry description: aiming to overcome these issues, a hybrid TF-FGM approach is introduced and validated in the conclusive part of this work, with very interesting results in terms of lift-off and flame shape.

In the final part, the hybrid TF-FGM model is applied to the same configuration operated with spray together with dedicated spray boundary conditions carried out from the research activity of the COmplexe de Recherche Interprofessionnel en Aérothermochimie (CORIA) research team. The results pointed out that although the flame is still not perfectly predicted, a large improvement is reached concerning the combustion and

spray modeling approaches commonly present in the literature.

Contents

Nomenclature

Acronyms

$ACARE$	Advisory Council for Aeronautics Research in Europe
AMR	Adapted Mesh Refinement
BC	Boundary Condition
$CAEP$	Committee on Aviation Environmental Protection
CFD	Computational Fluid Dynamics
DAC	Double Annular Combustor
$ELSA$	Eulerian Lagrangian Spray Atomization
EU	European Union
FGM	Flamelet Generated Manifold
$ICAO$	International Civil Aviation Organization
ICM	Interface Capturing Method
IRQ	Interface Resolution Quality
IRZ	Inner Recirculation Zone
$K-M$	Kelvin-Helmholtz
LDI	Lean Direct Injection
LES	Large Eddy Simulation
LPP	Lean Premixed Prevaporized
LTO	Landing Take-Off
OPR	Overall Pressure Ratio

ORZ	Outer Recirculation Zone
PDF	Probability Density Function
$PERM$	Partial Evaporation and Rapid Mixing
PIV	Particle Image Velocimetry
PSR	Perfectly Stirred Reactor
PVC	Precessing Vortex Core
$RANS$	Reynolds Averaged Navier Stokes
RQL	Rich-Quench-Lean
S	Swirl Number
SMD	Sauter Mean Diameter
SPH	Smoothed Particle Hydrodynamic
$TAPS$	Twin Annular Premix System
TF	Thickened Flame
UHC	Unburned Hydrocarbon

Greeks

δ	Thermal Flame Thickness	$[m]$
ϵ	Turbulence eddy dissipation	$[m^2 s^{-3}]$
λ	air-fuel equivalence ratio	$[-]$
μ	Dynamic viscosity	$[kgm^{-1}s^{-1}]$
ν	Kinematic viscosity	$[m^2 s^{-1}]$
ρ	Density	$[kgm^{-3}]$
τ	Time Scale	$[s]$
χ_{st}	Scalar Dissipation Rate	$[s^{-1}]$
Δ	Gradient	$[-]$
Φ	Equivalence Ratio	$[-]$
Γ	FGM-EXT reduction coefficient	$[-]$
ω	Reaction rate	$[kgm^{-3}s^{-1}]$

Letters

A	Area	$[m^2]$
c	Progress Variable	$[-]$
c_p	Spec. heat capacity at const. P	$[Jkg^{-1}K^{-1}]$

D	Diameter	$[m]$
Da	Damköhler Number	$[-]$
E_a	Activation Energy	$[J]$
k	Thermal Conductivity	$[Wm^{-1}K^{-1}]$
k	Turbulent kinetic energy	$[m^2s^{-2}]$
Ka	Karlovitz number	$[-]$
$\dot{m}$	Mass flow rate	$[kgs^{-1}]$
p	Pressure	$[Pa]$
PFR	Product Formation Rate	$[s^{-1}]$
$\dot{q}$	Specific heat flux	$[Wm^{-2}]$
R	Specific gas constant	$[Jkg^{-1}K^{-1}]$
r	Radius	$[m]$
Re	Reynolds number	$[-]$
S_L	Laminar Flame Speed	$[ms^{-1}]$
S_T	Turbulence Flame Speed	$[ms^{-1}]$
T	Temperature	$[K]$
t	Time	$[s]$
$U/V/v$	Velocity	$[ms^{-1}]$
z	Mixture Fraction	$[-]$

Subscripts

0	Total
$adiab$	Adiabatic
air	Air
b	Backward
c	Chemical
c	Coolant
$comb$	Combustion
f	Fluid
$fuel$	Fuel
g	Gas Phase
is	Isentropic
ov	Overall

ref	Reference
t	Turbulent
w	Wall

Introduction

One of the main concerns nowadays regarding civil aviation is without any doubt the emissions and the sustainability coming from this sector. The demand for lower emission requirements has been one of the main drivers for all the research efforts done in the past years in this field, even if safety and reliability are always the most important airworthiness criteria and there is no exception for low emissions combustors design perspective.
This demand has resulted in intense research activity in the field of the Gas Turbine's (GT) combustion chambers, which other than meet increasingly stringent regulations in terms of pollutant emissions, should guarantee low weight, compact design and above all high reliability [1, 2], as summarized in Figure 1. Considering the flight mission operations per se, the main responsible for the formation of pollutants is the combustion process that takes place in the combustor, therefore great attention has been devoted to such component and its operative conditions among all the possible scenarios.

Regarding the pollutant related to an aero-engine, the main chemical species are represented by Nitrogen Oxides (NO_x), Unburned Hydrocarbons (UHC), CO and Particulate Matter (PM): a detailed explanation of their impact on the environment and human health can be found in the work of Liu et al. [1]. Especially regarding the NO_x, special attention has been paid during the years to the mechanism behind their formation and how to limit this without impacting too much the combustion efficiency [3].

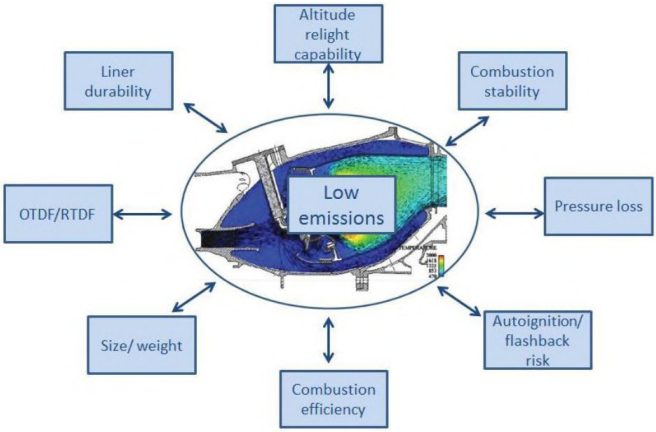

Figure 1: Modern aero-engine combustor requirements (OTDF/RTDF Overall/Radial Temperature Distribution Factor) adapted from [1].

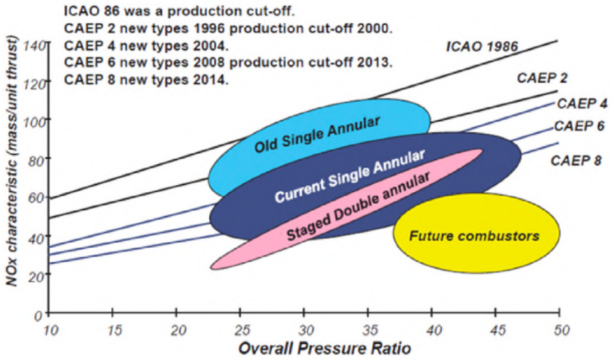

Figure 2: Low-emission combustors trends with NOx emission levels with respect to ICAO standards adapted from [1].

As shown in Figure 2, aircraft emissions are regulated by standards published and updated by the ICAO-CAEP, referring to the Landing Take-Off (LTO) cycle to simulate the aircraft operations below 915 m that include idle, take-off, climb-out and approach phases [4]. In addition,

ACARE collects a set of strategic guidelines for an environmentally-friendly development of civil aviation. Concerning this, ACARE imposes, first in Vision 2020 then in Flightpath 2050, a reduction of 75% and 90% per passenger kilometer respectively for CO_2 and NO_x emissions and a reduction of 65% for perceived noise [5]. Such implications related to air transportation have become more critical due to the current trends in aviation industries, resulting in an increase of OPR and TIT. Actually, these design factors promote NO_x production which is still one of the main critical aspects in the design of modern aero-engine combustors. Another important aspect to consider is related to Carbon Dioxide (CO_2) emissions. This chemical species is known for its impact as Green-House-Gas (GHG), thus contributing to global warming due to human activities. However, this product is an inevitable result of the combustion of fossil fuels. Indeed, the current regulations are not yet taking into account such chemical species as a pollutant.

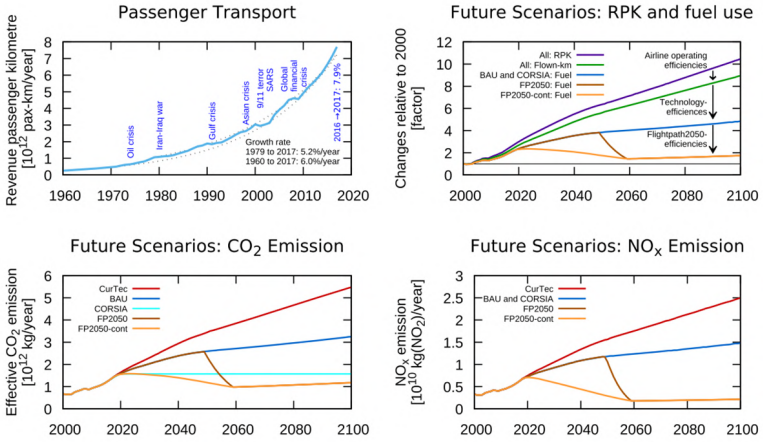

Figure 3: Overview on the global aviation transportation and related emissions for five scenarios adapted from [6]. BAU: Business as Usual; CurTec: Current Technology; CORSIA: Carbon Off-Setting Scheme; FP2050: Flight-Path 2050; FP2050-cont: Flight-Path 2050 continuous implementation.

A very recent study by Grewe et al. [6] reports also the possible scenarios in terms of NO_x and CO_2 depending on the future actions. These are depicted in Figure 5, where:

- *Current Technology* (CurTec) implies no technology improvements (referring to 2012 technology level);
- *Business-As-Usual* (BAU) stands for an increase for fuel efficiency without any specific aims to reduce the aviation climate impact;
- *Carbon-Offsetting Scheme* (CORSIA) is as BAU but with a carbon neutral growth from 2020 onward;
- *Flight-Path 2050* (FP2050) is as BAU, but including technology advancements, which are introduced according to Flightpath 2050;
- *Flight-Path 2050 continuous implementation* (FP2050-cont) As FP2050, but technology advancements are introduced earlier and a smooth transition is realised;

It should be notice that FP2050 and FP2050-cont differs in the speed of technology improvements.
These studies point out how only through the implementation of new technologies in principle should be possible to block a further increase of both NO_x and CO_2 emissions. Also considering the temperature changes reported in Figure 4, again is pointed out how the importance of a smooth transition toward more sustainable technologies is of paramount importance to achieve the desired goals. The previous considerations are particularly relevant if considering that the growth of the aviation sector, despite of the impact of the recent COVID-19 pandemic, is expected to further increase: this fact can be seen in Figure 5.

Keeping in mind the previous considerations, current thermal engines are clearly at a disadvantage with respect to novel electric propulsion concepts. In fact, a reduction of fuel consumption could be achieved only considering other aspect than the combustion process itself, such as reduction of weight and cooling air requirement [2]. Nevertheless, combustion

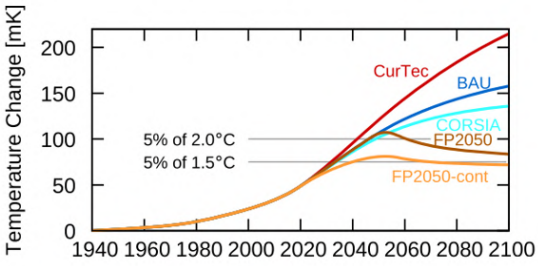

Figure 4: Near-surface temperature change of five scenarios including CO_2 and non-CO_2-effects from [6]. The horizontal lines indicate 5% of a 2 °C and 1.5 °C climate target.

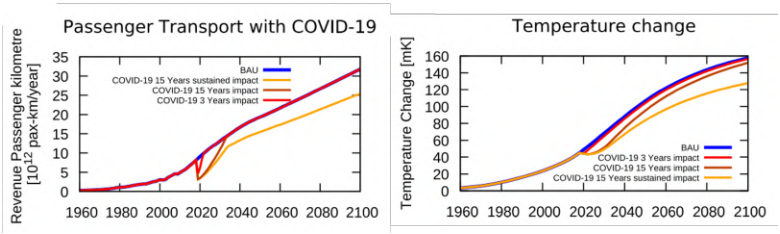

Figure 5: Impact on the passenger transport and temperature change from the COVID-19 pandemic from [6].

technologies are still of primary importance, especially concerning the potential use of alternative fuels, such as hydrogen [7] or Sustainable Aviation Fuels (SAF) [8, 9], which can be considered carbon-free or net carbon neutral. Furthermore, even new architectures such as hybrid electric-thermal propulsion systems would benefice from these improvements [10, 11].

Concluding, enabling low-NO_x technologies could be considered mandatory either as mid-term goal considering a transition to alternative systems or as integration with novel architectures. To this aim, in the years different solutions have been proposed [12, 13, 14] based on improvements of the current engines concepts. Also in recent years, many disruptive

concepts have been proposed such as the implementation of Moderate to Low (MILD) combustion for aero-engine applications [15], Trapped Vortex Combustion (TVC) [16] or Inter-Stage Burners [17]. Such very interesting concepts are providing different strategies to meet the goals in terms of pollutants, but still further investigations are required before their implementation in a real engine.
In this fashion, the present research activity would contribute to this process of improvement of the current combustors concepts.

Aim of the work

The main purpose of the present work is the numerical investigation of a novel concept of low-emission burner for aero-engine applications. Also, another important goal pursued within this research activity is the development and improvement of the required numerical modelling involving the combustion process and its interaction with the turbulent flow-field.
The mentioned burner is the object of the European project CHAiRLIFT, where lifted spray flames are employed with a specific disposition of the nozzles assuming a tilted configuration. This concept offers several advantages, which will be explained later in details, but above all, it aims to reduce NO_x emissions and improve flame stability. Surely, the use of lean combustors is not new with respect to the previous research activities, but the main challenge remains, that is guaranteeing the stability of the flame in all the operating conditions during the flight mission. The CHAiRLIFT concept would overcome this issue by establishing a macro-recirculation of hot combustion products in the burner which can improve the flame stability for very lean equivalence ratios.
This ambitious goal however requires large efforts in the investigation, since both experimental and numerical studies are required to understand the physics behind this type of lifted flame other than their mutual interaction in the burner when the tilted disposition is employed.
In the present work the investigation of the mentioned concept is car-

ried out through Computational Fluid Dynamics (CFD), which allows to include all the complex physical interactions occurring during the combustion process. Indeed, numerical modelling has gained more and more relevance especially considering the framework of GT applications [18, 19]. The main challenge here is the numerical modelling of the spray lifted flame employed in this burner concept. Despite of the fact that lifted flames have been investigated for years, as it will be discussed later, a complete understanding of the stabilization process is still missing. Moreover, this fact influence the related numerical modelling and eventually the reproduction of the flame is not trivial. Therefore, the present work would carry out a modelling strategy both accurate and affordable for these flames when applied to a real case scenario and potentially to a whole combustion chamber.
In this fashion this work represent one of few attempts available in the literature to model this type of low-swirl lifted flame employing gaseous fuel. Moreover, as far as the author is aware, it is the first numerical simulation on the same concept of flame operated with liquid fuel.
These steps are mandatory not only to gain a deeper insight on the complex physical phenomena occurring in the combustion chamber, but also to enable the investigation of the CHAiRLIFT burner when applied to a real case scenario.

Thesis outline

The numerical investigation of such novel combustor requires some steps, since several aspects are involved in terms of flow-field analysis, combustion process, numerical modelling and so on. Therefore, the entire study should be divided accordingly, aiming to separate each fundamental effect as much as possible. Keeping in mind the previously introduced challenges, the present work is structured as follows:

- **Chapter 1**: this chapter is devoted to the description of the state-of-the-art combustion chambers concerning aero-engine context. Here also the CHAiRLIFT burner features are described in details, aiming

to provide an overview of the benefits and constrains related to a modern GT's combustor to the reader;

- **Chapter 2**: here the main focus of this research activity, that is the low-swirl lifted spray flame investigated in previous experimental campaigns, is introduced together with the numerical tools needed for its investigation. Also here the issues related to its numerical modelling is reported for a complete understanding of the problem by the reader, explaining the context into which the numerical tools have been developed;

- **Chapter 3**: this chapter reports the investigations carried out so far on the multiburner configuration currently object of the experiments within the project. This part would investigate the impact of the tilt angle on the interaction between adjacent flames. A preliminary numerical setup is exploited as it is derived from the investigations on the fundamental single sector from the previous chapter. Additionally, some remarks concerning the numerical modelling are discussed, especially considering the real engine operating conditions;

- **Chapter 4**: here the same nozzle concept employed in the previous chapters and operated with gaseous fuel is the object of an extensive numerical campaign with scale resolving approaches. The goal is to understand which combustion model among the ones available in the literature is the most suitable in terms of accuracy and cost-effectiveness to investigate the low-swirl lifted flame. The use of gaseous fuel has a twofold objective since it allows to avoid the multiphase environment numerical modelling, hence it helps to better understand the physics involved in the combustion process alone. Also here, the implementation of the selected combustion model within a CFD commercial solver is reported and tested;

- **Chapter 5**: this chapter collects the outcomes of the previous ones and of detailed studies on the spray boundary conditions to carry

out the first numerical study, as far as the author is aware, on the low-swirl lifted flame when operated with liquid fuel. The first results of such study are described aiming to provide an overview of the improvements introduced and the challenges to be addressed to, since it is preparatory for a future application to the multiburner configuration;

Finally, a summary of the main achievements of this research activity is given together with conclusions and recommendations for future works.

Chapter 1

Low emissions combustor technologies

The reduction of pollutant emissions during a flight mission could be obtained through the improvements of many aspects concerning both the engine and its implementation in the airframe. However, how the combustion process is occurring within the engine will affect the presence of such chemical pollutant not expected from the combustion process, such as NO_x, UHC, and particulate matter.
The combustor is indeed responsible for these chemical species, since the combustion process converts chemical energy into thermal power. For this reason, during the years, several efforts have been devoted in the research to innovate and develop this component. This is particularly true for the emissions related to the NO_x species, which have a tremendous effects on both human health and the environment [1]. This pollutant is related to the presence of gaseous nitrogen in the air employed for the combustion process, and the chemistry behind its formation is quite complex. However, the most relevant mechanism production has an exponential dependence from temperature and it is referred in the literature as *Zeldovich mechanism* [20]. This represents a remarkable disadvantage since high operating temperature is beneficial for the CO and UHC reduction,

other than for the overall efficiency of the engine.
Furthermore, low temperature combustion is usually obtained with a reactive mixture composition with large air excess, or *lean* [3], which could negatively impact the flame anchoring in the combustion chamber. Keeping in mind all these aspects, in the following the state-of-the-art of concerning modern aero-engine combustors is discussed.

1.1 State of the art of aero-engine combustors

Considering the mentioned objectives, during the years two main strategies have been carried out in order to meet the desired goals and are currently in use:

Rich-Quench-Lean (RQL) combustors

This concept is adopted in the almost totality of the current aero-engines and it was introduced for the first time in 1980s in order to reduce NO_x emissions. The working principle is that a first rich burning primary zone ($\phi = 1.2 - 1.6$) is present close to the injector in order to ensure a stable flame anchoring, then followed by a sudden quenching of the flame thanks to the injection of air which reduce the equivalence ratio, then a final section where lean combustion ($\phi = 0.5 - 0.7$) is accomplished. The idea is therefore to skip the stoichiometric conditions which lead to the production of NO_x as shown in Figure 1.1.

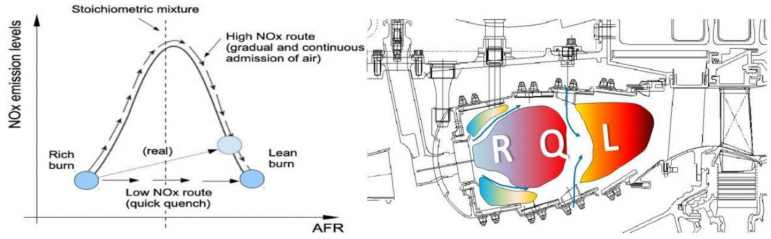

Figure 1.1: Rich-Quench-Lean combustor concept adapted from [21]

This concept is very popular for its safety and reliability, but it suffers of some disadvantages concerning the emissions reduction. First, local stoichiometry is not avoided completely, and actually the quenching section should be carefully designed to avoid this problem. Also, the final zone should guarantee a temperature high enough to oxidize CO and UHC generated in the primary zone under rich conditions. Finally, the design of the cooling system is challenging due to the large amount of air used for the quenching section, liner cooling has a lower amount of available air. Also, the PM generated in the primary zone before being oxidized in the last section, increase the radiative heat transfer in this region. Here a complete discussion of such concept is out of scope, while the interested reader is referred to [22, 23, 24] for further details;

Lean burn combustors

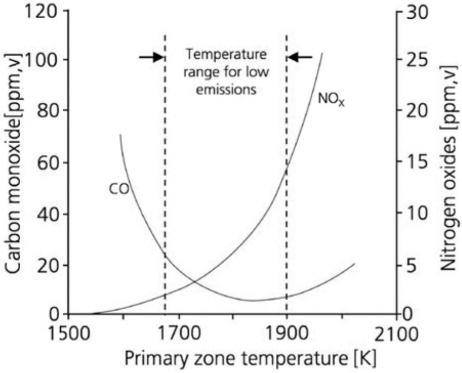

Figure 1.2: Lean burn combustor operating concept [25].

This technology represents the most promising technology to reduce the NO_x in the aero-engine framework. The idea behind this combustor is quite straightforward since it operates in a lean combustion regime from the beginning, that means within a range of equivalence ration between 0.5 and 0.7, corresponding to a flame adiabatic temperature of 1800 -

1900 K. This range should guarantee a trade-off between NO_x emissions and CO and UHC ones, as depicted in Figure 1.2.
The key to accomplish this lean combustion regime is the strict control of the reactive mixture equivalence ratio before the reaction zone. However, this fact is particularly challenging in an aeronautical combustor, where safety and stable flame anchoring should be guaranteed among all the operating conditions in the flight missions. In fact, due to the lean combustion regime, the flame is more prone to combustion instabilities such as Lean Blow-Off (LBO) occurrences [3]. Also, the preparation of the premixed reactive mixture is not trivial and could lead to further disadvantages as potential flashback risks [3].
Therefore, during the years several strategies have been carried out to mitigate the problems related to the implementation of the Lean burn concept in a real engine: the most popular are briefly described in the following.

Fuel staging

The most common strategy present in many current engines is represented by the use of staged combustion. Here, the air and fuel injection is controlled by different locations within the combustion chamber [26]: the staging consists of enabling and disabling these injection locations accordingly to the operating conditions, as depicted in Figure 1.3.

Figure 1.3: Staged lean burn combustion concept adapted from [27].

An example of staged combustion is represented by the *Double Annular Combustor* (DAC) developed by General Electric (Figure 1.4), where two different radial zones are present, namely the pilot zone and the main

zone. For low power conditions, only the pilot injectors is used, as it is designed to work with a relatively high equivalence ratio to ensure flame stability ($\phi \approx 0.8$). Instead, at high power settings also the main injectors are activated and a global lean equivalence ratio is reached in the combustion chamber, retrieving low NO_x and smoke emissions.

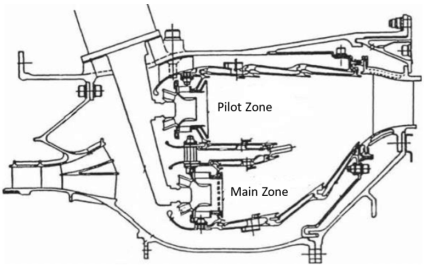

Figure 1.4: GE Double Annular Combustor (DAC) cross-section adapted from [27].

It should be said that this configuration introduces challenges in cooling due to larger dome surface areas and in controlling the exit temperature profile due to possible low mixing between the pilot and the main flows and, consequently, due to the presence of stoichiometric high temperature spots [1, 2]. This is indeed a first attempt to implement lean burn combustors within aero-engines, but it shows some limits in terms of emissions reductions due to the presence of the pilot zones, other than introducing some complexities in the systems and an increase of weight and dimensions which limits this application to medium-large size engines. Moreover, a different implementation of this concept is represented by the fuel staging within the same injector, as available in the Twin Annular Premixing System (TAPS) injector by GE. This can be considered an advanced injection system based on an internally piloted configuration [28].

As shown in Figure 1.5, the fuel staging is now occurring within the same nozzle, where two distinct zones can be recognized: one dominated by a premixed flame zone and an inner zone with a pilot flame to enhance

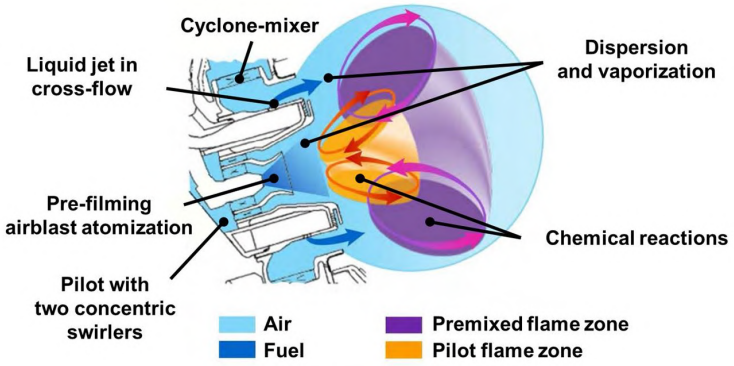

Figure 1.5: GE Twin Annular Premixing System (TAPS) concept [29].

stability and ignition of the main zone. This configuration is obtained thanks to a fuel split between two set of injection points, where the pilot injector is a simplex atomizer [30] placed in the center of the nozzle itself and surrounded by co-rotating swirlers [3], while the main injector consists of a radial inflow swirler (i.e., cyclone-mixer) and jet-in-cross-flow injection points arranged around the swirler body [29]. Similarly to the previous concept, the fuel split is set in agreement with the operating conditions, obtaining a good reduction of the NO_x emissions with a relatively compact system with respect, for instance, to the DAC system.
The drawbacks of this configuration are represented by the fact the pilot zones are somehow affecting the potential pollutant emissions, other than a not negligible complexity of the nozzle for this task.

Lean Premixed Prevaporized (LPP)

If the use of a pilot injector would be avoided, the preparation of the lean reactive mixture should be accomplished before reaching the reaction zone. Also, this mixture should guarantee a high degree of homogeneity to avoid the mentioned combustion instabilities.
In this sense, a possible technology is represented by the Lean Premixed Prevaporized concept [1], where three dedicated areas can be found [14]:

the fuel preparation duct for premixing and pre-vaporising, the combustion zone and the dilution zone.
These processes of mixing, fuel drop injection and evaporation have to be optimized to ensure suitable conditions for extremely lean burn when the resulting mixture is supplied to the combustion zone. The dilution zone further reduces the FAR in a similar manner to conventional combustors, as shown in Figure 1.6.

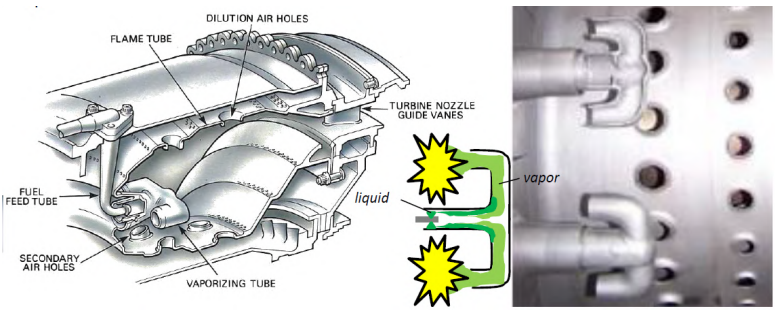

Figure 1.6: Lean Premixed Prevaporized (LPP) concept adapted from [27].

The main advantage of such concept is that the probability of NO_x formation is significantly reduced due to the low flame temperature and absence of hot spots in the combustion zone. This also benefits liner durability due to low flame radiation and lower service temperatures. However, the main drawback is the high risk of flashback which could occur within the fuel preparation duct [1, 14]. Indeed, a higher residence time within this plenum would lead to a better homogeneity of the reactive mixtures but also a larger susceptibility to auto-ignition phenomena.
Moreover, the mentioned risk is particularly enhanced by the high operating pressure adopted in the modern aero-engines. Indeed, the LPP concept is relegated to low-OPR engines (e.g., OPR $\leq$ 25) [1].

Lean Direct Injection (LDI)

The Lean Direct Injection concept, as indicated by its name, retrieve a lean operating point by directly injecting the fuel into the combustion chamber. In this fashion, the need for a dedicated device for the reactive mixture preparation is avoided with all the related drawbacks, but however a quick and high-quality air-fuel premixing should be achieved in a short distance before the reaction zone. This task is possible only with advanced injection systems since the liquid fuel must rapidly be atomized, evaporate and mix with the air before the reaction zone. This is particularly challenging since usually the aeronautical combustors are compact and therefore there is very few time before reaching the flame anchoring position.
Generally, this objective is retrieved thanks to the employment of a large amount of air and wide recirculation zones, which contributes to improve the homogeneity of the air-fuel mixture. Indeed, when this aspect is guaranteed, this system has the best performances with respect to the previously introduced ones, since it can both avoid the flashback risks and the hot spots due to local stoichiometric conditions. Other hand, this strategy is prone to combustion instabilities resulting in the LBO occurrences and increase of UHC and CO emissions [1].
To some extent, this approach is similar to what has already been introduced with the TAPS injector, at least if the pilot injector is excluded. Also, in the literature other concepts such as the Avio Aero Partially Evaporating and Rapid Mixing (PERM) concept (Figure 1.7) and the Rolls-Royce Lean Direct Injection (LDI) [1, 28, 31] have been investigated. Another very promising concept instead has been proposed by NASA with the Multi-Point Lean Direct Injection (MPLDI) system [1], where a sort of matrix constituted by a very large number of small injection points is used. However, concerning the data available in the literature, the latter concept has not been implemented in a real engine yet.

Keeping in mind this, the most challenging aspect of a LDI system is to design the injector, and many efforts have been put in the research also to develop proper methodologies to fulfill this aim [28, 33]. Also, it should

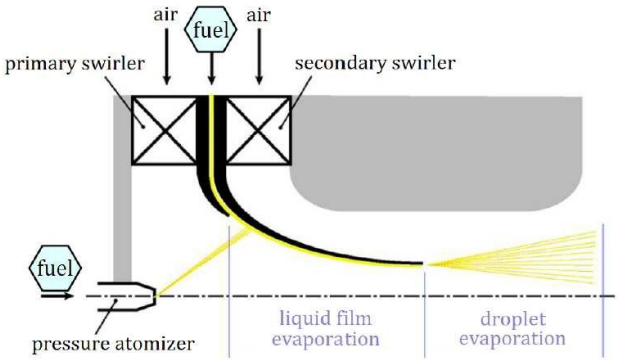

Figure 1.7: Avio Aero Partially Evaporating and Rapid Mixing (PERM) concept [32].

be mentioned that these systems devote a large amount of combustion air for the fuel injection, while a smaller amount with respect to other concepts is left for combustor cooling. Therefore, the adoption of a LDI system should accompanied with advanced cooling system able to ensure high performances with a reduced amount of air. As well as the injection system, many efforts have been put in the investigation of these devices [2, 34, 35]

Concluding remarks on the combustor technologies

Although the Lean burn combustors reserve certain advantages concerning the RQL concept in terms of emissions, their application is still limited due to the high complexities and potential safety and reliability issues. Their main problems remain the auto-ignition and flashback risks other than the possible LBO occurrences. Another important point is the high altitude relight capability, which is especially challenging for these systems [36]. A further aspect is that these systems are more prone to thermoacoustic instabilities, which is a phenomenon due to the coupling between combustor acoustic modes, pressure fluctuations in the flow field and unsteady heat release due to combustion instabilities. Here the risk

is to retrieve serious structural damages of the combustor casing. All in all, these aspects have contributed to limite the diffusion of the Lean burn combustors in civil air flights and thus the reduction of the emission planned by the ICAO for the future. This fact is even more important is considering the scenario where alternative fuels are employed. In this sense, a deeper insight into the combustion process occurring within the combustion chamber is mandatory also for innovative and disruptive future engine architectures.
Keeping in mind these aspects, in the following section a novel combustor concept will be introduced with the aim of avoiding or mitigating the mentioned issues, therefore allowing the implementation of the Lean burn concept within aero-engine applications.

1.2 The CHAiRLIFT burner

A novel strategy to overcome the issues introduced previously in the Lean burn framework is represented by the combustor concept proposed in the CHAiRLIFT project [37], under the European research program CleanSky2 Joint Undertaking.
The CHAiRLIFT acronym stands for *Compact Helical Arranged combustoRs with lean LIFTed Flames*, which resume the main features of such concept: the use of low-swirl flames with an inclined disposition of the burners, as shown in Figure 1.8). The goal is to allow the safe and stable use of ultra-lean spray flames without the need for pilot injectors or premixing devices. In this fashion, the inclination of the burner (from now on referred as *tilting angle*) will establish a macro-recirculation inside the combustion chamber responsible for the transport of hot combustion products from one burner to the next one.
The aim is to provide a sort of inherent piloting between adjacent burners, albeit without dedicated pilot zones. Moreover, the mentioned lifted spray flame already provides for very low level of NO_x emissions, as it will be explained in details. Considering the importance of these two concepts for the present study, in the following the main characteristics

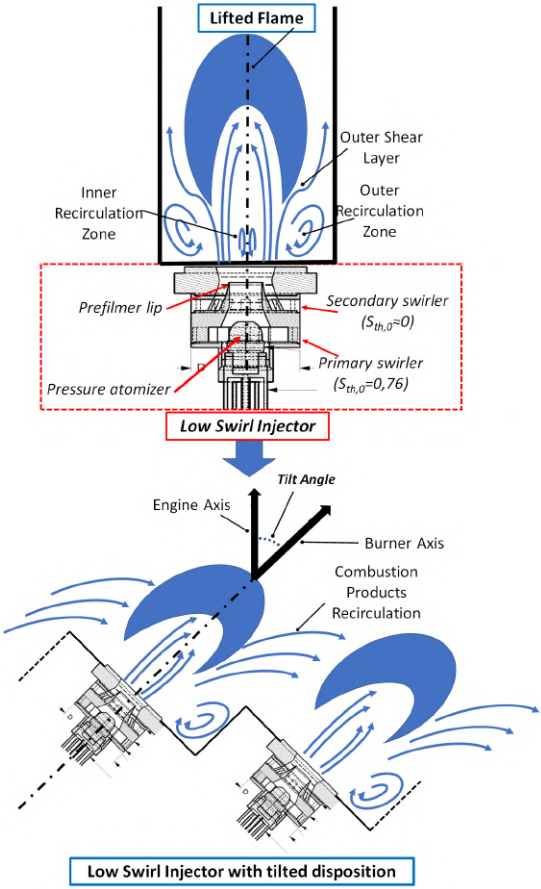

Figure 1.8: Conceptual sketch of the CHAiRLIFT architecture.

and developments for both such features are reported.

Low-swirl lifted flames

Generally speaking, a flame is defined *lifted* when the reaction zone is detached from the burner exit according to the definition given by Wohl et al. [38]. The distance between the burner dome and the flame base is often reported in the literature as Lift-Off Height (LOH) or Lift-Off Length. In contrast, when the reaction zone is anchored to the nozzle somehow, it is often referred in the literature as *rim-stabilized*.
According to this definition, however, a very large number of flames con be defined as lifted, while often the flame lift-off is more considered a scenario under specific operating conditions for a flame which normally should be attached to the burner rim [39].

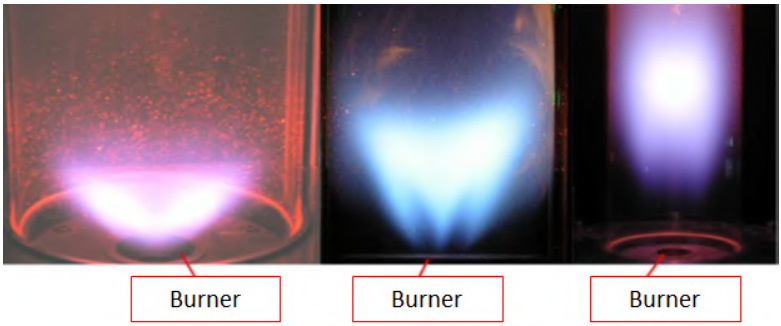

Figure 1.9: Examples of lifted flames (adpted from [40].

For the sake of clarity, within this work, "lifted flame" refers to a flame that is stably anchored in the flame tube remarkably away from the nozzle outlet in all the possible operating conditions (i.e., order of tens of millimeters). Therefore, if this definition is retrieved, only the last picture on the right in Figure 1.9 is considered a lifted flame here.
Lifted flames have been widely investigated in the scientific literature for years [38, 41] especially considering the jet of fuel in quiescent air configuration. Many studies have been carried out both concerning aca-

demic [42, 43] and industrial test cases [44] since this type of flame is involved in many applications such as gas turbines, industrial burners and internal combustion engines. Indeed, they are very common since offer some advantages such as they are easy to implement in a real burner and the nozzle experiences lower service temperature therefore easier maintenance. Above all, these flames drastically reduce the flashback risks hence increasing the safety and the reliability of the combustor, while recently they have gained interest since are related to lower NO_x emissions with respect to rim-stabilized flames [45, 46], when a proper air-fuel premixing is achieved.

It should be said that the literature on this topic is very large and a complete overview is out of the scope of the present work. Thus, accordingly with the objectives of the present research activity, only premixed flame suitable for modern GT's applications will be discussed. This means that only lifted flames employing swirled nozzle [3] are considered since this configuration has proven to reduce fuel consumption and emissions of pollutants through the enhancement of the air-fuel mixing [47, 48]. Generally, the idea behind the use of a swirled nozzle, or most commonly just swirler, is the establishment of recirculation zones, which are zones where the flow-field is reversed assuming negative axial velocities. These regions entrained and recirculated a portion of the hot combustion products to mix with the incoming air and fuel. This arrangement not only anchored the flame, but also provided the rapid mixing of fuel vapor, air, and combustion products needed to achieve high heat-release rates [3]. Flames anchored with this strategy are also called *Swirl-Stabilized* in the literature.

In this fashion, the occurrence of the flame lift-off is often related to the use of a low swirl number $S_{th,o}$ below 0.6 [49], where this quantity is defined as:

$$S_{th,o} = \frac{\dot{D}_i}{R_i \dot{I}_i} \tag{1.1}$$

being D_i the angular momentum flux, while I_i and R_i are respectively

the axial momentum flux and the inner radius of the prefilmer lip at the smallest section.
The swirl number is an indicator of the tangential velocity component magnitude in the flow-field: for instance, high-swirl nozzles are related to the establishment of a strong recirculation zone close to the burner axis, due to the collapse of the flow structures once it is issued from the nozzle itself, with a phenomenon called *Vortex Breakdown* [50]. Often, when a recirculation zone is present near the burner axis it is called Central Recirculation Zone or Inner Recirculation Zone (IRZ). On the contrary, the recirculation zones present between the external casing and the velocity jets is referred to as Outer Recirculation Zone (ORZ). It should be said also that the previous explanation is very general, while each nozzle could have its own arrangement of such zones. However, a common feature of low-swirl nozzle is that the so-called vortex breakdown is not occurring.
As far as the author is aware, only two concepts have been investigated and sometimes implemented in a real burner based on a stable low-swirl lifted flame configuration: the Lawrence Berkeley Nationals Laboratory's concept and the KIT-EBI's one. Also, it should be noticed that the discussion concerning the comparison between low-swirl injectors and high-swirl is not limited to the lift-off occurrence, and the interested reader is referred to [51, 52, 53, 54].

***Low Swirl Combustion* concept**

The first concept is the one carried out at the Lawrence Berkeley National Laboratory and later patented by Cheng R. and co-workers [55, 56, 57], referred in the literature as *Low Swirl Combustion* (LSC). In the years this concept has been also investigated by others [58, 59], and a specific test case named *Low Swirl Burner* has been developed jointly by Lawrence Berkeley National Laboratory, the Lund Institute of Technology and the Technical University Darmstadt [60]. A sketch of the LSI flame together with the reference burner is shown in Figure 1.10.

The LSB establishes a divergent turbulent flow of reactants, as de-

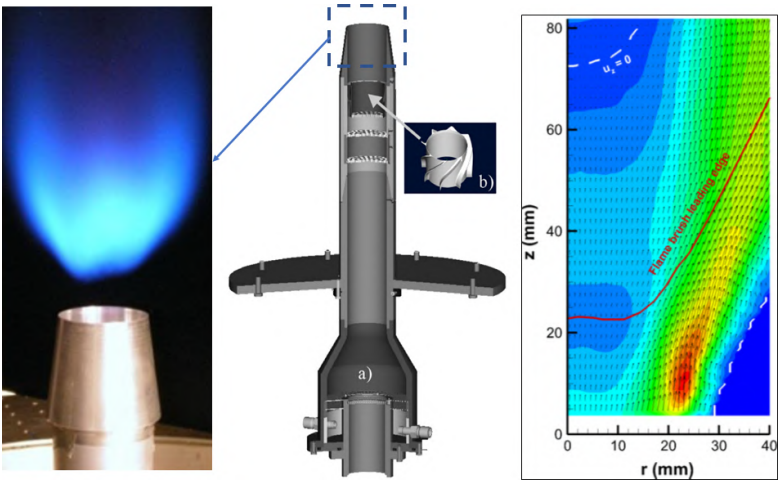

Figure 1.10: LSI flame (left) with LSI reference burner (mid) and related flow-field in the proximity of the nozzle exit (right), adapted from [58].

picted in Figure 1.10, that aerodynamically stabilized a detached freely-propagating premixed flame. This flame is suitable as well for confined and unconfined configuration and the outer swirling component of the mean flow interacts with the ambient air in the outer shear region [58]. The central region of the LSB, instead, is essentially isolated from the outer flow and it is devoid of complex large scale flow structures. Remarkably, the LSB flame does not require an additional energy source such as a pilot flame at very lean fueling conditions to maintain flame stability. Also, self-similarity of the divergent flow-field enables the LSB device to operate over a wide range of fuel mixtures, flow velocities, equivalence ratios, device pressures and fuel temperatures.
The LSB burner has been widely investigated both numerically and experimentally: thanks to its robustness it allows lean methane and hydrogen fuels to be studied at similar inflow and turbulent conditions [61].

Among these studies, an interesting one is the comparison between LSI (low swirl injector) and HSI (high swirl injector) in terms of emissions

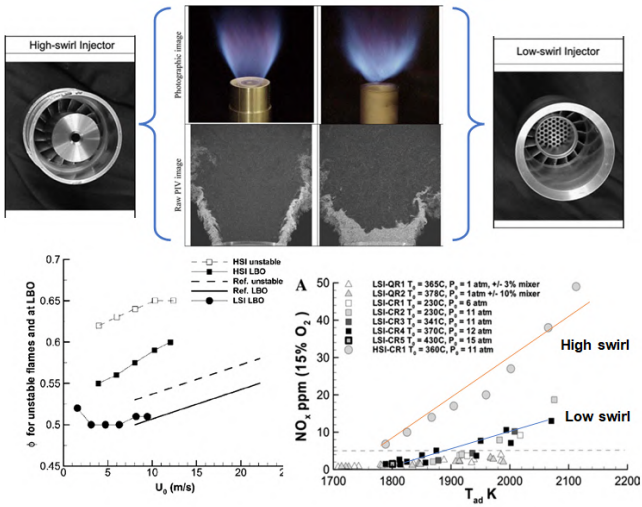

Figure 1.11: Comparison between LSI (low swirl injector) and HSI (high swirl injector) emissions adapted from [52].

and LBO limits carried out by Johnosn et al. [52]. The main results are reported in Figure 1.11, where the NO_x emissions are plotted against the theoretical adiabatic temperature for various operating conditions of the LSI and with a reference case of the HSI. In the same Figure, also the equivalence ratio limits against the inflow velocity are reported.

It can be seen that the LSI concept has superior performances in terms of NO_x emissions with respect to the HSI configuration in the reference conditions, but also for a wide range of operating conditions the emissions levels are relatively low, especially for a $T_{ad} \leq 1900K$. These results also imply that the LSI can operate farther away from LBO (higher theoretical adiabatic temperature) so that it may be less prone to combustion oscillations.

For the sake of brevity, in this study, only a brief introduction to this burner is given, however such interesting results justify the implementation into a real industrial burner [62]. Despite of these interesting results, it

could be expected that the implementation of Berkeley's burner within an aero-engine is much more complex since the requirement for a premixing duct, which somehow leads to the same issues of the LPP combustors introduced Section 1.1.

KIT-EBI's burner concept

The second concept employing a swirl stabilized combustor with a low-swirl lifted flame is the concept proposed by Zarzalis and investigated at the Engler-Buntler Institut (EBI) of the Karlsruhe Institute of Technology (KIT) [63]. In the years this flame have been investigated from the same research team with both gaseous and liquid fuels and under many different operating conditions [40, 64, 65, 66, 67, 68, 69, 70]. In this case, the working principle is the opposite with respect to the LSB concept, since here the nozzle produced a flow-field which presents a swirl component near the axis and full axial component moving away from it. In Figure 1.12 the working principle for this burner is shown.

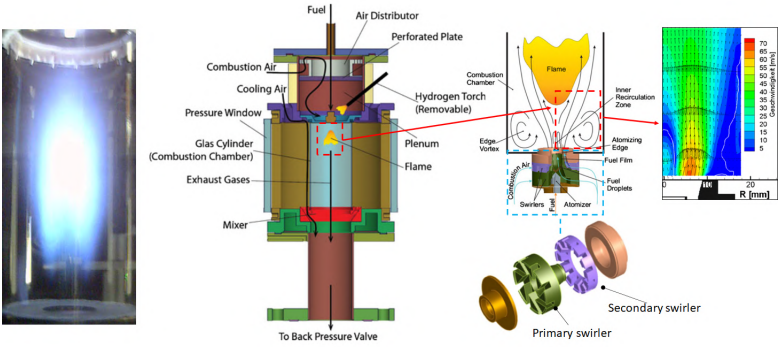

Figure 1.12: KIT-EBI's low-swirl burner concept (left), flame picture with working principle (mid) and related flow-field in the proximity of the nozzle exit (right), adapted from [40, 68].

With respect to the previous burner, this concept is particularly interesting since it employs a double-swirl radial injector derived from an

air-blast atomizer [30], also visible in Figure 1.12, where the primary swirler imposes a tangential component to the flow, while the secondary swirl includes only fully radial channels. In this fashion, the injector exhibits a weak IRZ, enveloped within high-stream velocity jets. Another relevant difference in comparison with the Berkely's burner is that the flame assumes an arrow shaped reaction zone [65], where the flame stabilizes on the outer shear layer of the swirling jet issuing from the nozzle. This highlights the importance of such region, and a detailed explanation will be given Chapter 2: however, it should be pointed out that this flame cannot be ignited without the confinement walls [65], which contributes to establish the ORZ and thus stabilize the flame.
Nevertheless, this concept remains quite straightforward to implement in a real engine due to its similarity with a currently employed injection system. Indeed this system can be considered formally a non-premixed injector since here separate ports for air and fuel are present, which actually operate as a premixed system. The experimental investigators in fact found that the air-fuel premixing is achieved within the LOH distance and a *premixed-like* combustion regime is finally obtained [65]. Hence, the interest for this type of flame is due to the very promising performances in terms of NO_x emissions for with respect to a classic attached flame [64, 65, 68].

In Figure 1.13 the emissions of NO_x and the stability limits for the KIT-EBI's burner operated with gaseous fuel [65] and liquid fuel [68] are reported. Concerning the gaseous flame, a direct comparison with an attached is present: it can be seen how this flame corresponds to lower emissions when operated at theoretical adiabatic temperature related to lean combustion regime in comparison with an attached flame. Also, The stability is improved, where the lifted configuration is extinguished for lower equivalence ratios again respect with to the attached one.
Another interesting study is the one carried out by Kasabov et al. in [67, 68], where the emissions and stability limits were measured for a wide range of operating conditions and injector's effective areas. Again, the lean combustion regime is characterized by extremely low levels of

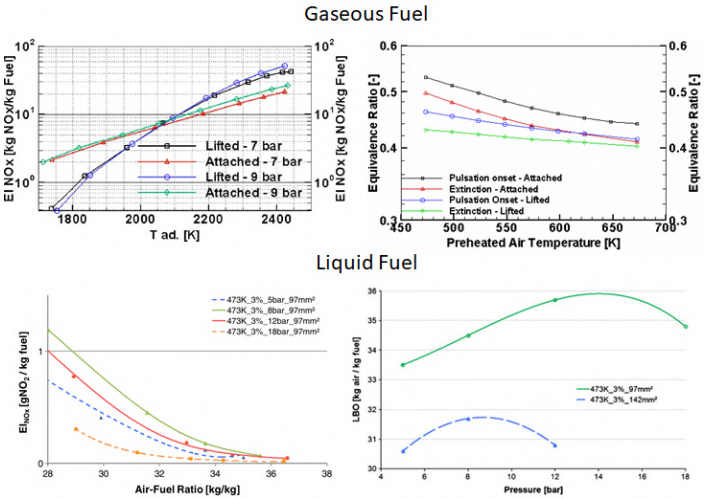

Figure 1.13: NO_x and stability limits for the KIT-EBI's burner operated with gaseous fuel (top) [65] and liquid fuel (bottom) [68].

emissions: this effect is even more evident at higher operating pressures, which are close to the ones employed in small-size engines (see Figure 1.13 bottom). According to the authors, this behaviour is due to the enhancement of the air-fuel premixing experienced in the LOH distance. In this sense an increased pressure will results in a longer LOH due to the increase of turbulence, hence the local quenching phenomena related to this [68].

Nevertheless, general conclusions are very hard to be found, since when liquid fuel is adopted, several physical phenomena are present. For instance, again from [68], an increase of temperature to intermediate level (from 473K to 573K) leads to lower NO_x emissions due to quicker evaporation of the fuel and thus a better premix, which avoids local stoichiometric points. However, a further increase up to 673K results in an increase of emissions due to a shift upstream of the flame position related to higher flame speeds.

Also, general considerations on the LBO limits are not trivial, since as shown in Figure 1.13, they are strictly related to the geometrical features of the nozzle and how this affects the ORZ. Still according to Kasabov [40], the jet from the nozzle is related to the effective area of this component and leads to a different extension of the ORZ and it affects the final flame stabilization, as visible in Figure 1.14.

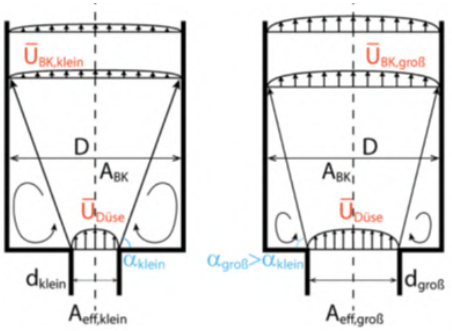

Figure 1.14: Effect of the nozzle effective area on the confinement ratio adapted from [40].

Finally, this type of injector has been recently the object of an investigation of sulfur combustion by Zhang et al. in [71]. This very interesting study compares the low-swirl injector developed at KIT-EBI with a high-swirl injector, finding that the former is able to achieve lower flame temperature and avoid the droplets hittinh the lateral confinement walls.

In conclusions, the KIT-EBI's low-swirl concept is extremely interesting under many points of view, especially concerning the objectives of the CHAiRLIFT project. Nevertheless, further investigation are required, especially considering an eventual implementation in a real aero-engine. Also, this section was dedicated mainly to provide an overview of the performances of this kind of low-swirl lifted flame in terms of LBO limits and emissions: furhter details concerning the stabilization mechanisms and the flame structure will be given in Chapter 2.

Inclined arrangement of the burners

The other key feature of the CHAiRLIFT concept is the inclination of the burners, often referred in the literature as *Short Helical Combustor* (SHC). This concept was originally proposed by some investigators [72, 73], then followed by some GT manufacturers [74, 75] in the years, where basically the same strategy was employed.
The underlying idea is that the burners axis are tilted by a prescribed angle with respect of the engine axis, so imposing a pre-rotation to the flow and thus a helical flow pattern for an annular combustion chamber. The expected advantages regard the possibility to increase the exhaust recirculation among adjacent burners promoting flame stability. Other important features are the reduction of the combustor length, which helps to reduce the overall weight of the engine and improves the structural characteristics. As well, the need for Nozzle Guide Vanes (NGV) at the turbine inlet is reduced, again contributing to reduce weight and also cooling air requirement. A sketch of the SHC concept can be seen in Figure 1.15.

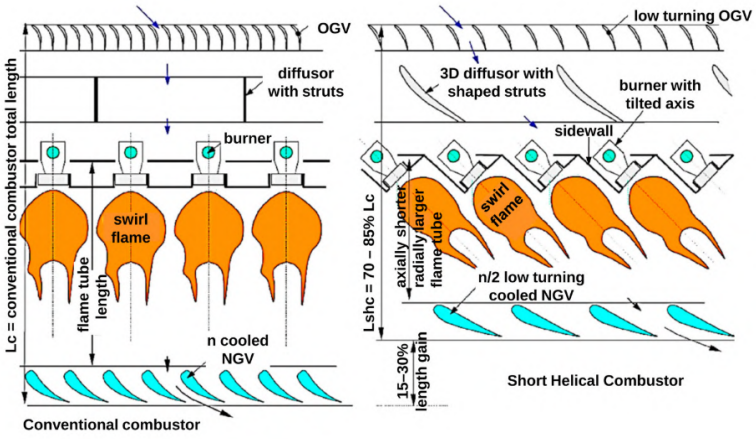

Figure 1.15: Schematic illustrations of the SHC concept from [76]

This combustor has been studied in detail at the Institut für Thermische Strömungsmaschinen (ITS) of the KIT by Ariabatar et al. [76, 77], with a dedicated campaign focused on the numerical analysis of the aerothermal characteristics of high-swirl flames. These very extensive studies analyse several aspects of such concept through CFD simulations in both cold and reactive conditions. In particular, Ariabatar and coworkers studied several arrangements of the swirler nozzles, in terms of their number and direction of the swirl component. The outcomes point out that a double annular configuration with a tilt angle of 45° and co-rotating swirlers leads to the best configuration in terms of gas recirculation and flow pattern at the combustor exit [76].
Another important finding was related to the interaction between the flame and the lateral confinement wall. In fact, the tilted arrangement imposes an asymmetrically confined by the sidewalls resulting in an unbalanced pressure field which ultimately affects the flow angle at the outlet and the presence of hot spots [77]. This effect is related to the impingement of the swirling jet on the lateral wall, which establishes the asymmetric pressure field: this, in turn, induces a resulting force in the opposite direction that affects the angular momentum of the flow, which is rapidly lost after the inlet of the burners. In the same study, it is reported that those issues were avoided by contouring the sidewall to locally accelerate the flow and decrease the pressure gradient in the tangential direction.

In another study by Hu et al.[78], the effects of the tilt angle for a single annular configuration were investigated through numerical simulations. Also, in this study, the CFM56 swirlers are employed as nozzles, where $S_{th,o}$ for the primary and secondary swirler are respectively 1.589 and 0.656.
One of the most interesting features is the presence of four different vortex modes depending on the tilt angle. These vortex modes affect the recirculation and the temperature field of the isothermal and the reacting flow. Beyond a specific tilt angle, a further increase is responsible for a reduction of the hot combustion products exchange among the burners.

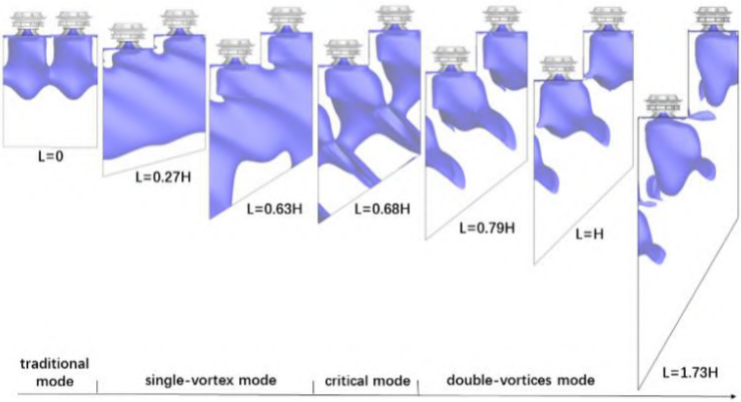

Figure 1.16: Recirculation of non-reacting flow in model SHC with different tilting angles (adapted from [78]).

This fact is very important since it highlights the non-linear behavior of the recirculation zones with the tilt angle increase, as shown in Figure 1.16. Moreover, a recent study by Zhang et al. [79] demonstrates that partially confined swirling flow such as the SHC can suppress the Precessing Vortex Core (PVC) [50] leading to a positive impact on the promotion of absolute instability.
The use of a tangential flow-field is also adopted by a novel combustor by SAFRAN Helicopter Engines (SHE) and referred to as Spinning Combustion Technology (SCT), reported in Figure 1.17.

This concept has been the object of numerical and experimental investigations [81], which pointed out its flexibility in terms of ignition and blow-off capabilities. To some extent, it can be considered an extreme application of the SHC concept, where the injectors are arranged in a manner as the reactive flow assumes a strong azimuthal component inside the annular chamber. In this fashion, the altitude relight [3, 36] is favoured due to the enhanced hot gas recirculation among the burners other than an extremely compact design of the chamber is achieved, helping to reduce the overall mass.

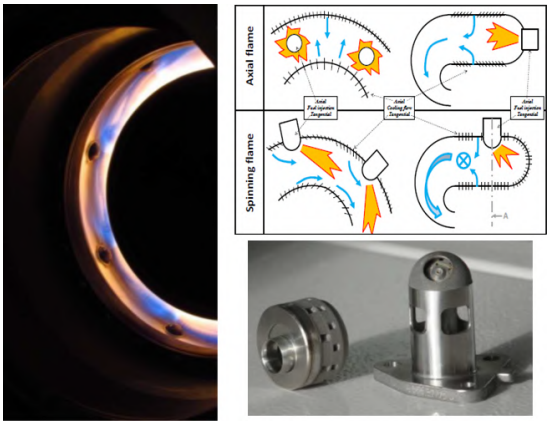

Figure 1.17: Spinning Combustion Technology concept by SAFRAN (adapted from [80]).

Although this concept is already exploited into the Airbus Helicopters H160 [80], the advantages in terms of NO_x are not reported, other than the scalability of this approach to larger engines should still be tested.

Concluding remarks

In this chapter the main challenges of low emissions combustor for aero-engine applications have been introduced together with some strategies which potentially can improve the Lean Burn combustors implementation. In this sense, the novel combustor concept proposed in the EU project CHAiRLIFT could contribute to this goal. This combustion chamber actually, operates as LDI concept but avoiding the use of pilot injectors, thus to the NO_x emissions related to such devices. As well, this chamber will allow a compact design saving weight a reducing the overall size of the engine and cooling air requirement with respect to the current RQL and Lean burn combustors with fuel staging.
The CHAiRLIFT concept has been investigated recently by Shamma [82] and Hoffman [83] together with respective co-workers. The numerical

study in [83] shown that low-swirl flow strongly interacts with the sidewall of each burner and it experiences a deflection towards this direction due to an asymmetric pressure field. Therefore the angular momentum flux of the helical flow at the combustor outlet is increased compared to the nominal tilt angle of the burners. Other important parameters have been found to be the distance of the jet to the sidewall and the position of the inner and outer liners. Hence, the ratio of nozzle diameter to combustor diameter is crucial for the recirculation characteristics.
The numerical and experimental study in [82] has confirmed again that unwanted flow deflection of swirled flames with tilted arrangement is avoided by using low swirl. The most interesting outcome is the remarkable high LBO limits for non-piloted burners, observed for all investigated configurations. The multiburner configurations were observed having a superior stability range in contrast to the typical decrease in stability of high-swirl multiburner reported in the literature. Such behaviour could be related the transfer of hot exhaust gas from the neighboring burner to the flame base of the adjacent burner for the inclined configuration and due to recirculation zones enhancement in inline configuration, which is essential for the stabilization of the lifted flames.
Moreover, the tilted burner disposition and the low-swirl lifted flames are certainly two fundamental aspects of this project, but however other disruptive technologies are investigated in this work such as the ion probe measurements for the LBO precursors detection and the plasma discharge for the combustion instabilities suppression [84, 85, 86, 87]. Concerning the latter, plasma enhances combustion by promoting at the same time the production of heat, radicals and excited species. Some specific configuration of the plasma discharges, as Nanosecond Repetitively Pulsed (NRP) discharges can control combustion instabilities [88].
Summarizing, the CHAiRLIFT concept seems very promising under many points of view, but it requires a deeper understanding of the physics behind the stabilization of a lifted flame. In this fashion, numerical simulations could allow a detailed investigation, supporting and enhancing the parallel experimental investigations. Moreover, numerical approaches could avoid

the need for intrusive experimental techniques, which could affects the measurements itself. In the following chapter, the main characteristics of a single sector low-swirl flame are described. Particularly attention is devoted to the numerical approaches required for their modelling, since their importance in the investigation of the CHAiRLIFT burner.

Chapter 2

Fundamental stabilization mechanisms for a low-swirl lifted flame

In Chapter 1 the potentialities of the low-swirl lifted flame investigated at KIT-EBI research centre have been introduced in order to provide an insight of their role in the CHAiRLIFT burner. Here, the focus is on their stabilization mechanisms and how this affects the subsequent numerical modelling. This chapter also introduced to the single sector test case investigated previously in [40, 64, 65, 66, 67, 68, 69, 70] and its numerical model within the present work.

2.1 Flame characteristics

The main feature of this low-swirl flame is clearly the lift-off occurrence, which places the flame stably downstream the nozzle exit. The region before the main reaction zone has a paramount importance, since here the mixing between fuel and oxidizer is accomplished while the ignition is prevented, hence the flame reattachment. This kind of stabilization is allowed by the upstream transport of hot vitiated gas from the principal reaction zones due to the ORZ towards the early region of the main

swirling jet, as already pointed out in Chapter 1.

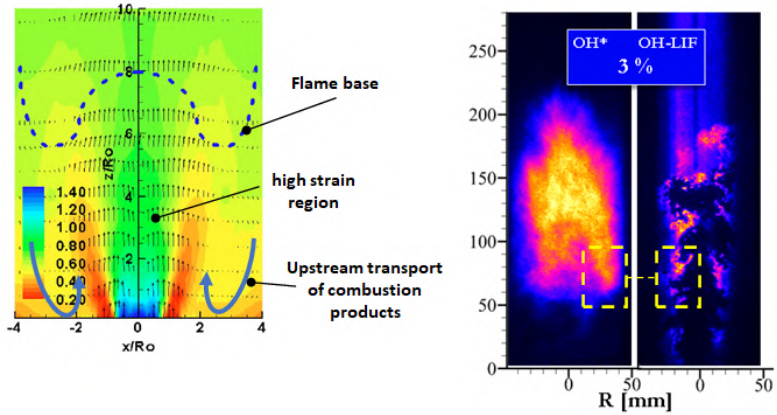

Figure 2.1: Experimental map of equivalence ratio with reported the main regions of the flame adapted from [65] (left) and instantaneous maps of OH chemiluminescence and OH-PLIF adapted from [70] (right).*

The description of such stabilization mechanism is confirmed by the experimental investigations where a large and exhaustive set of sensitivity analyses have been carried out to point out the influence of main operating parameters such as inlet temperature, operating pressure, pressure drop across the nozzle and air-fuel equivalence ratio λ [65, 69, 70] and conceptualization of the described stabilization mechanism is depicted in Figure 2.1. Thanks to these studies, the following general conclusions about the flame stabilization process can be drawn:

- Elevated temperatures at the jet base have a great impact on the flammability limits since they increase the laminar burning velocity significantly. This means that this kind of flame for this configuration has a higher resistance to lean blow-out;

- Four regions are observed in the flame: i) pre-combustion area, ii) combustion zone, iii) outer recirculation area, and iv) a post-flame region. Particularly interesting is the fact that the maximum tem-

perature on the combustion zone corresponds to the 80% of the adiabatic temperature, while in the post-flame region the temperature approaches constant levels and equals the adiabatic combustion temperature. This fact points out that the combustion zone is experiencing a relevant heat loss, which should explain the lowered reactivity occurring in the pre-combustion area, hence the lift-off of the flame;

- The recirculation of hot gases has a dominant role in the stabilization of the flame: when removing chamber confinement the flame cannot be stabilized in any operating conditions.

- The validity of a premixed-like stabilization process of the flame seems to be confirmed by the absence of auto-ignition phenomena, at least with gaseous fuel, according to the experimental investigators. The observed flame front does not point out the typical triple flame structure suggesting an auto-ignition process, while, as observed in Figure 2.1-Right, the instantaneous concentration of OH provided by PLIF reveals pockets of reacting mixture in the early region of the swirling flow (pre-combustion area), despite local high flow velocity and extremely lean mixture do not allow flame to stabilize.

Finally, the flame topology shows an arrow-like shape, where the flame base is anchored on the outer shear layer of the swirling jet: such morphology is very similar to a tribranchial flame structure, even if proof of its existence is not supported by the local equivalence ratio and flow-field [65].
Another interesting finding is that the influence of the confinement walls is not only limited to the establishment of the ORZ, but also to the temperature of recirculating gas has a primary role in the ignition of the incoming fresh mixture [64]: the heat transfer from hot gas surrounding the jet and its core is related to the entrainment of hot gas pockets due to Kelvin-Helmholtz instabilities at the jet surface (see again Figure 2.1-Right).
This fact highlights also the importance of the heat losses through the confinement walls, which could cool down the transported products thus

postponing the mixture ignition and elevating the lift-off height.

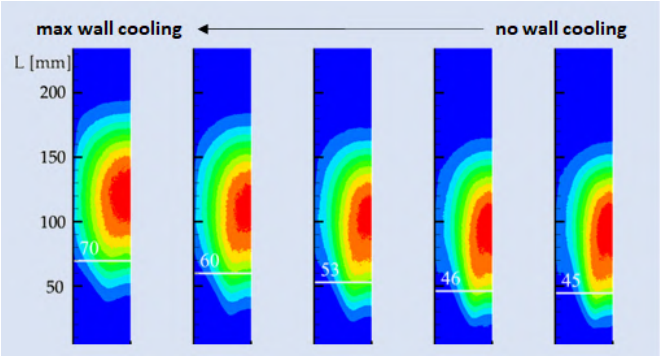

Figure 2.2: Experimental map of OH chemiluminescence for various levels of wall cooling from [70].*

This aspect was observed also by Sedlmaier in [70] and shown in Figure 2.2, where OH* chemiluminescence maps are reported for various cooling flow rates: as it will be explained later in detail, the OH* excited radical can be seen as an indicator of the on-going reaction, hence it shows the position of the reaction zones. From this figure, it is clear the effects of the wall heat losses since the flame elevates with the increase of cooling flow and furthermore such increase becomes non-linear when the flame interacted with the walls, enhancing the heat transfer.
Other parameters which affect the LOH magnitude are related to the operating conditions [68, 69] and the already mentioned confinement ratio [40]. All these aspects contribute again to the fresh mixture pre-heating before the flame front or influence the turbulence levels in the lift-off region. In conclusion, the lift-off region is dominated by several physical effects, which in turn directly control the turbulent flame speed and ultimately the stabilization position for the flame.

2.2 Numerical modelling in isothermal conditions

Although many experimental investigations have been performed on this low-swirl lifted flame in recent years, a complete understanding of the flame stabilization mechanism is still missing. In this regard, a reliable and accurate numerical approach revests an important role within the present investigation, especially considering an implementation within the SHC concept as explained in Chapter 1, where a strong three-dimensionality and asymmetry of the flow-field are expected.
In fact, considering the low-swirl flame object of this study, as far as the author is aware, very a few numerical works have been carried out on this nozzle concept: a first study by Kern et al.[89] and a more recent one by Sedlmaier [70]. In both cases, the numerical simulations have shown a misprediction of the reaction zone position, leading sometimes to the flame reattachment. This fact points out the challenges related to the numerical modeling of these flames.
This section is therefore devoted to introduce the numerical setup employed to investigate the single sector configuration and the outcomes in terms of flow-field prediction in isothermal (i.e., non-reactive without fuel injection) conditions: these results are reported also in [90].
Later, the flow-field information will be employed in Chapter 3 for describing the boundary conditions in the multiburner configuration, other than in Chapters 4 and 5 the numerical setup will be derived from the one described in the following.

Single Sector tese case and numerical model

Here, the test case reported in the latest investigations carried out by Sedlmaier is taken as reference [70]. This is similar to the one by Kasabov introduced in Chapter 1, but now the nozzle is modified to operate also with gaseous fuel. To this aim, methane is introduced thanks to a dedicated slot, as shown in Figure 2.3, and the injection location is just upstream of the prefilmer lip.
The combustion air is collected in a plenum chamber placed upstream

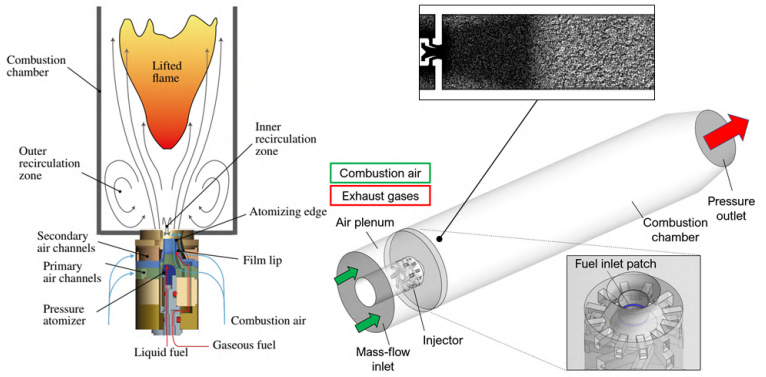

Figure 2.3: Sketch of the investigated rig adapted from [69] (left) and numerical domain for the investigations in [90] (right).

of the nozzle, once being pressurized and preheated according to the specific operating conditions. Therefore, the air enters in the nozzle, where it is split between the two swirlers: the largest amount is delivered to the secondary channels, while the air passing through the primary one experiences a preliminary mixing with the fuel. The two air streams are gathered after the prefilmer lip edge in the nozzle diffuser, hence they are introduced in the flame tube. It is worthy to point out that a homogeneous premixing has yet not occurred at this position.

Overall low-swirl conditions at nozzle outlet are obtained by large difference in the swirl number imposed by primary and secondary channels. Primary swirler has eight channels, where the swirl number assumes a value of $S_{th,o} = 0.76$, while the secondary swirler, with twelve radial channels, has $S_{th,o} \approx 0.0$: resulting overall $S_{th,o}$ is well below 0.4. For this test case, the effective area of the nozzle is equal to 131 mm^2 $\pm$ 4 mm^2.

The flame is confined in a cylindrical combustion chamber equipped with double-walled quartz-glass optical access. The overall length of the chamber is 320 mm (where 280 mm is the length of the optical window) and an inner diameter of 89 mm. A constant cooling air flow is supplied into

the walls cavity for such reactive tests employing methane: a preliminary quantification of the heat losses has been carried out by measuring the cooling air temperature at the cavity outlet and reported in [70].
A prior characterization of the flow-field coming from the nozzle has been carried out from isothermal operating conditions. LDA measurements are available both in terms of contours and velocity profiles for specific axial positions in the injector near field. It should be pointed out that this low swirled field results also in a low frequency PVC: for the cold flow conditions a frequency of 3-4Hz has been identified by the authors and further data are available in [70].
In the present research activity, a first numerical investigation of this nozzle has been conducted with spatially-filtered compressible Navier-Stokes equations for the Large Eddy Simulation (LES) approach using the solver ANSYS Fluent 2019-R1 [91].
The subgrid stress tensor due to the filtering operation has been closed through the Dynamic Smagorinsky-Lilly model [92] for its reliability and low computational cost. In this approach, the eddy viscosity μ_t is related to the resolved strain rate $\overline{S}$ as:

$$\mu_t = \rho L_s^2 |\overline{S}| \tag{2.1}$$

Here, L_s and $\overline{S}$ are, respectively, the characteristic SGS mixing length and the traceless symmetric part of the square of the velocity gradient tensor defined as:

$$L_s = min\left(\kappa d, C_s V^{1/3}\right) \tag{2.2}$$

$$|\overline{S}| = 2\sqrt{\overline{S}_{ij}\overline{S}_{ij}} \tag{2.3}$$

where κ is the von Karman constant, d is the local distance to the closest wall, C_s is the Smagorinsky constant and V is the cell volume. C_s is dynamically computed based on the information provided by the resolved scales of motion.
Finally, both spatial and temporal second order numerical schemes have been adopted.

The numerical simulations have been performed on two different conditions: an isothermal one, in order to characterize the injector flow-field behavior, and a reactive one. While the latter will be discussed in Chapter 3, once the turbulent combustion modelling is introduced, this section focused on the isothermal conditions: these are summarized in Table 2.1.
The numerical domain, shown in Figure 2.3, includes the entire flame tube to fully represent the unsteady turbulent effects in the combustion chamber. A cylindrical plenum has been added to simulate the air supply condition upstream of the nozzle, as well as a convergent duct at the outlet for the exhaust tube. A preliminary simulation has been performed on a coarse mesh (4M of tetrahedral elements), then applied on a refined grid corresponding to 10 M of elements. From the coarse domain to the refined one, the number of elements within the nozzle diffuser diameter passes from 16 to 52.
The isothermal simulation adopted a physical time step of $1 \cdot 10^{-5}$ s, while for the reactive simulation the value of the time step corresponds to $1 \cdot 10^{-6}$ s. The final averaging time window covers a physical time of 0.2 s for the isothermal case, which corresponds to a approximately 8 times the Flow Through Time (FTT) of the first 100 mm of the combustion chamber, where the flame is positioned. Both configurations employ mass-flow inlet and pressure outlet as boundary conditions, as shown in Figure 2.3. Walls are modeled with no-slip conditions and five prismatic layers have been employed for near-wall flow treatment through scalable wall functions.

Operating pressure p_0	101325 Pa
Air inlet temperature T_0	323 K
Nozzle pressure drop $\Delta p_{nozzle}/p_0$	3 %
Equivalence ratio ϕ	-

Table 2.1: Operating conditions adopted in the numerical simulations on the single sector in isothermal conditions.

Flow-field results for the isothermal configuration

The first assessment has concerned the correct representation of the flow field in cold conditions, aiming to validate the numerical setup with the detailed LDA measurements available from the experimental campaign. In particular, by considering this configuration, the focus is on the representation of the fundamental flow-field and the related turbulent structures, regardless of the combustion processes possibly occurring in the flame tube. The comparison between CFD and EXP data is reported both in terms of radial profiles of velocity at given axial positions and contours maps: three different axial positions have been considered for the velocity profiles extraction, according to the available experimental data.
Also, here only the profiles for the finer mesh are reported for the sake of brevity. Similarly, the radial component is not reported since its low magnitude with respect to the other components is expected to have a lower impact on the final flame stabilization.

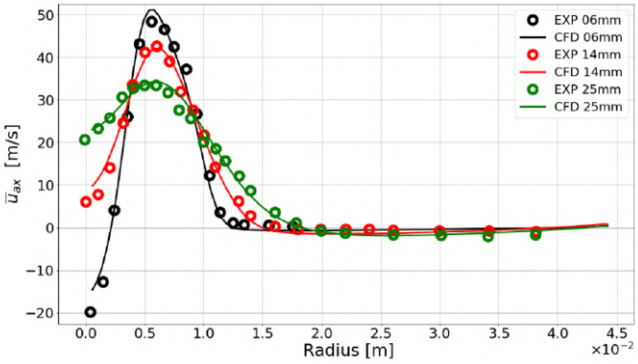

Figure 2.4: Comparison between numerical and experimental data in isothermal configuration: mean axial velocity radial profile at 6, 14 and 25 mm.

Concerning the mean axial component of velocity, results are in good agreement with the experimental data, showing an appropriate representa-

tion of the characteristic flow-field of the nozzle. It is clearly pointed out the limited aperture of the annular jet due to the the low swirl number. Swirling jet penetrate maintaining the radial location of its peak velocity within 10 mm: at higher radii the velocity decays to slightly negative values, leading to the characteristic outer recirculation zone. Also the IRZ is well reproduced, with its reduced extension both in terms of axial and radial positions, as expected for this type of injector.
As shown in Figure 2.5, the IRZ is embedded within the high-velocity streams issuing from the nozzle. Instead, the ORZ has a relevant axial extension, since it almost reaches the end of the contour maps, up to 90 mm. In the same figure, it can be seen also how the swirling jet maintains a relatively high magnitude up to 50 mm: after that, the jet diffuses gradually in both the axial and radial direction.

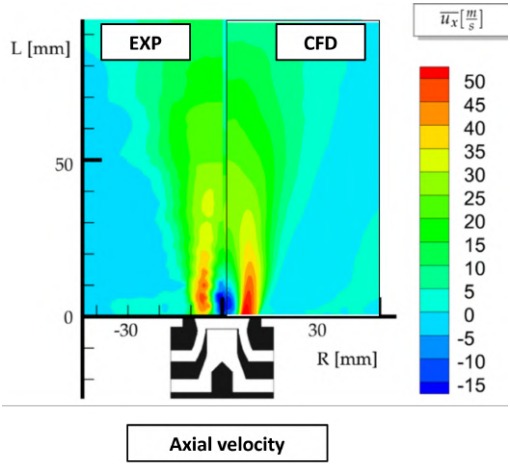

Figure 2.5: Nozzle near field contours maps (up to 90 mm) of mean axial velocity in isothermal conditions. Left: experiments; Right: CFD.

Regarding the axial velocity fluctuations it can be seen that the larger values can be found again in the inner region within 15 mm, with the presence of a main fluctuations peak within 5 mm, and a second lower one within 10, then decaying moving towards the ORZ. Here, the second

peak is slightly underestimated by the numerical simulation, especially for the closest axial positions.

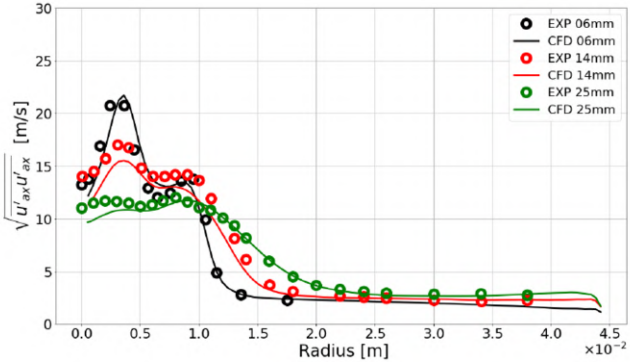

Figure 2.6: Comparison between numerical and experimental data in isothermal configuration: mean fluctuations of axial velocity radial profile at 6, 14 and 25 mm.

Regarding the mean tangential component of velocity profiles in Figure 2.7, it can be seen its overall lower magnitude with respect to the axial one, as expected considering the low-swirl nozzle.
A peculiarity of this injector is that, similarly to the axial component, a peak of tangential velocity can be found in inner regions, followed by almost zero values between 7 and 10 mm, due to the presence of the non-swirled air steams outgoing from the secondary channels. In the ORZ, this component is slowly decaying, but still maintain the same orientation of the swirling flow of the inner region. For this component, the numerical results are showing a quite good agreement with the experimental data, showing only an overall small underestimation of both the peaks in the inner region within 15 mm.

The mean tangential velocity maps in Figure 2.8 clearly show the aforementioned double velocity peak in the radial direction. Also, as already highlighted for the axial component, the higher values for this component are below the 50 mm in the axial direction, then slowly decaying. From the maps the discrepancy between the experimental data

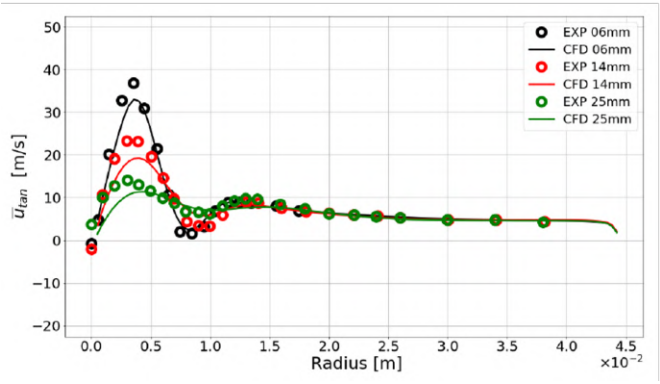

Figure 2.7: Comparison between numerical and experimental data in isothermal configuration: mean tangential velocity radial profile at 6, 14 and 25 mm.

in terms and numerics in terms of the secondary peak is more visible, since the latter case is less extended in the axial direction.

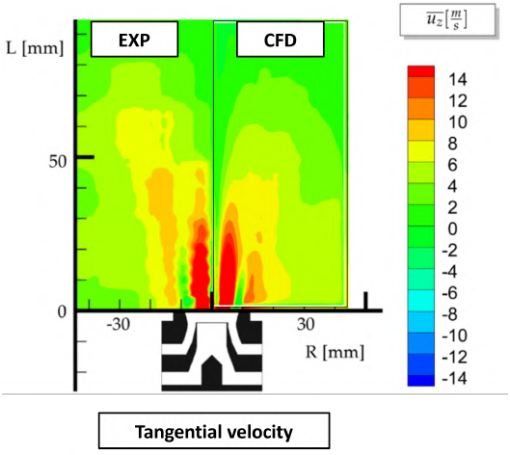

Figure 2.8: Nozzle near field contours maps (up to 90 mm) of mean tangential velocity in isothermal conditions. Left: experiments; Right: CFD.

If the tangential velocity fluctuations in Figure 2.9 are considered, a general lack of accuracy is present: the trend along the radius is substantially similar to the one observed experimentally, but the discrepancy between CFD and EXP data reaches up to the 30% of the expected value, in the innermost region within 15 mm from the axis.
A possible explanation for these results can be addressed to a not proper discretization of this region of the flow, pointing out that a more refined mesh should be employed within the nozzle and its near field.

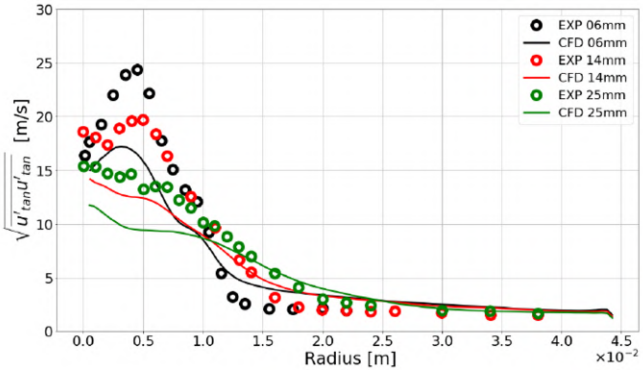

Figure 2.9: Comparison between numerical and experimental data in isothermal configuration: mean fluctuations of tangential velocity radial profile at 6, 14 and 25 mm.

Nonetheless, considering the still high computational cost for the isothermal simulation and a substantially quite good agreement regarding the mean velocity components, these results can be considered acceptably good for the further reactive simulation. Investigation on this lack of turbulent components is left to further works in order to better understand their influence.

Concluding remarks

This chapter discussed the main experimental findings carried out by the previous investigators on the low-swirl flame in single sector

configuration. Moreover, the importance of the recirculating combustion products, other than of the regions responsible for their transport has been highlighted. Once again, it should be highlighted how recirculating gas are crucial for the flame stabilization, especially considering their temperature, as it will be shown in Chapter 4. Regarding this, the correct reproduction of the turbulent structures stabilizing the flames is expected to have a great impact. In this regard, the preliminary attempt to reproduce the flow-field in cold conditions has shown a good agreement with the available experimental measurements. Moreover, all the features described previously in Section 1.2 seems adequately represented. The next chapter will introduced therefore the multiburner test case modelling, while exploiting the results from this chapter for the boundary conditions modelling.

Chapter 3

Multiburner numerical investigations

The previous chapters aimed to introduce the CHAiRLIFT burner concept and the rationale behind this novel architecture. Furthermore, an overview concerning the low-swirl lifted flame investigated in the years at KIT-EBI, in terms of stabilization mechanisms and flow-field characteristics were provided.
In this chapter, the multiburner of the CHAiRLIFT project, currently object of the experimental campaign at KIT-EBI [82], is investigated through numerical simulations with a twofold intent: the assessment of the numerical setup for the multiburner investigation and the support to the experimental campaign, especially concerning the tilt angle for the linear array of burners.
In the following sections a first introduction to numerical modelling and the experimental test rig is given, while some conclusions are reported for various tilt angles: these results are reported also in [93]. Also, the challenges due to different operating conditions will be introduced at the end of this chapter for potential further investigation.

3.1 Multiburner test rig

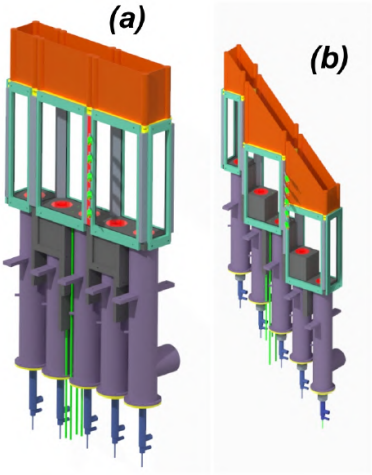

Figure 3.1: Schematic of modular burner array at different inclination angle; where (a) inline case (θ= 0°) and (b) inclined case (θ= 45°), from [82].

The experimental rig here considered is the burner in multi-sector configuration shown in Figure 3.1 and reported in [82]. A linear array consisting of five burners is employed to study the interaction between adjacent flames in terms of flow-field and temperature distribution. To this aim, several configurations are tested in which the burner's axes are inclined of a given tilt angle value θ, to understand how it affects the combustion process when gathered with low-swirl lifted spray flames. For each tilt angle a corresponding axial shift h, which identifies the height of the step, is defined to reproduce the aforementioned effects.
Each burner consists of a combustion chamber with a square cross-section of 100x100 mm and an axial extension of 300mm confined by four quartz-glass windows which provide optical access for the measurements in the flame interaction regions. The chamber operates at atmospheric pressure

without the presence of any cooling devices, meaning that wall temperature is determined only by the interaction with the hot gas and any possible heat loss occurring through the chamber walls.
During the tests, the pressure drop across the nozzle and the global equivalence ratio could be modified, other than the air preheating at the inlet. The airflow is collected in a plenum before being introduced inside the chamber through nozzles with a nominal effective area of 319 mm^2. Apart from this, the injector is in all respects equal to the one described in Chapter 2 and employed in [40, 70]. In this case the nozzle operates with liquid fuel, therefore in the center of the nozzle is placed a pressure atomizer that provides the liquid fuel (JET-A1) to the prefilmer where the liquid film is formed before being disintegrated. This point marks the beginning of the atomization process, taking place between the two air streams and generating the spray which feeds the main reaction zone. Therefore, fuel and air mix before reaching the flame front, all along with the lift-off distance.
Concerning the final section, the test rig is designed to operate with two different configurations of the outlet. In the first one, the flow expands in the ambient without any constraint (refereed as *open case*) while in the second one, an outlet contraction is employed to prevent air ingestion from the surrounding ambient (referred as *contraction case*). Among the available experimental conditions, the specific boundary conditions considered in this numerical work are resumed in Table 3.1.

Operating pressure p_0	101325 Pa
Air inlet temperature T_0	296 K
Nozzle pressure drop $\Delta p_{nozzle}/p_0$	3 %
Equivalence ratio ϕ	0.47
Fuel type	Spray (JET-A)

Table 3.1: Operating conditions adopted in the numerical simulations for the multiburner configuration.

Regarding the experimental measurements, temperature fields maps on the diagonal plane and on the outlet section are available, as well as

OH* chemiluminescence maps.
In [93], the test rig has been investigated through multiphase reactive simulations of the full-rig for various test rig configurations, summarized in Table 3.2. A set of preliminary simulations on a reduced periodic domain for the Inline configuration has been performed to tune the modelling settings, since the effects of the flow deflection is not present. For the sake of brevity, only the final setup adopted on the full rig configuration is here reported. Moreover, Inline and 45DEG simulations on the full rig have a twofold target: validate the numerical modelling with the available experimental data and understand the tilt angle effect of the gas recirculation. Then the 20 and 30DEG simulations with the contraction have been performed to investigate and seek the best setup of the burner. The CFD calculations have been conducted with the ANSYS FLUENT 2019R3 suite: where not specified, the numerical models concerning turbulence, combustion and spray description are reported in [91] together with the related literature references.

Case	θ $[deg]$	h $[mm]$	***Open case***	***Contraction case***
Inline	0	0	●	○
20DEG	20	36.39	○	●
30DEG	30	57.73	○	●
45DEG	45	100	●	●

Table 3.2: Test rig configurations in the numerical investigations.

Domain and Boundary Conditions

A sketch of the computational domain with a visualization of the main boundary conditions especially for air inlets is reported in Fig. 3.2. Here, the nozzle is partially removed aiming to reduce the overall number of elements and the computational efforts. The air inlets present therefore two different patches, respectively for the outer swirler and the inner one. Also, the position of the flames can be visualized thanks to the isosurfaces of the source term of the progress variable divided over the density (i.e., Production Formation Rate, PFR): it can be observed how the outlet

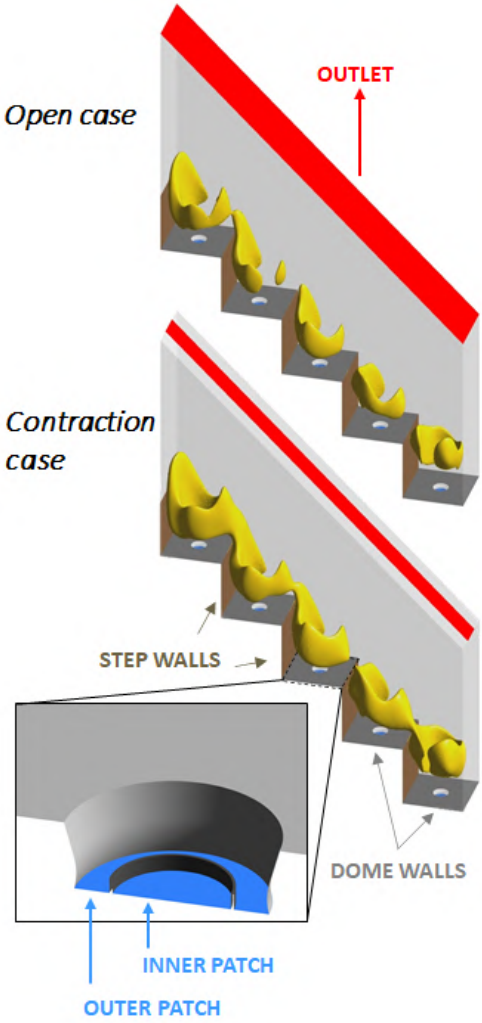

Figure 3.2: Computational domain with an iso-surface of product formation rate for the 45DEG case with and without the contraction [93].

configuration affects the flame shape and the test rig flow-field. Regarding this point, further details will be given in the results section. For the post-processing the *Z-coordinate* indicates the main stream direction while the *X-coordinate* runs through all the burners. For convenience, the origin of the reference frame is set in the top center of the first chamber (upper left in Fig. 3.2). For all the simulations, as previously mentioned, the experimental rig has been modeled starting from 2 mm upstream of the prefilmer lip up to the burner outlet. A fully unstructured mesh has been generated with polyhedral elements and comprehensive of local refinements in the nozzle region and the main reaction zone: an equivalent sizing respectively of 0.3 mm and 0.7 mm has been imposed.

Moreover, a buffer zone has been simulated after the outlet section to reproduce the external ambient surrounding and the possible recirculation. Finally, 5 prismatic elements have been used near the walls to obtain an overall number of elements of 18 million. A sketch of the polyhedral mesh for the Inline case is shown in Figure 3.3.
Regarding the two air patches highlighted in Figure 3.2 (inner and outlet inlets), a target mass flow rate corresponding to the conditions of Table 3.1 has been imposed. This boundary condition consists of an adapted radial profile derived from previously LES carried out on the same nozzle with smaller effective area [90] described in Chapter 2.
Here, it is assumed that the trend in the radial direction concerning mass flow distribution and turbulent quantities are the same for the two nozzles. Instead, the absolute value of the delivered airflow will be larger for the actual nozzle due to the larger effective area, for the same operating conditions. Therefore, the final profile is up-scaled with to respect the prescribed overall value of air mass flow. These assumptions will be verified and improved once PIV measurements of the injector's flow-field will be available. Moreover, considering the previous studies performed on the single sector configuration by Kasabov [40] for nozzles with different effective areas, only minor discrepancies with the real physics of the problem are expected by following this approach.
For the outlet patch, the atmospheric pressure is imposed while all the

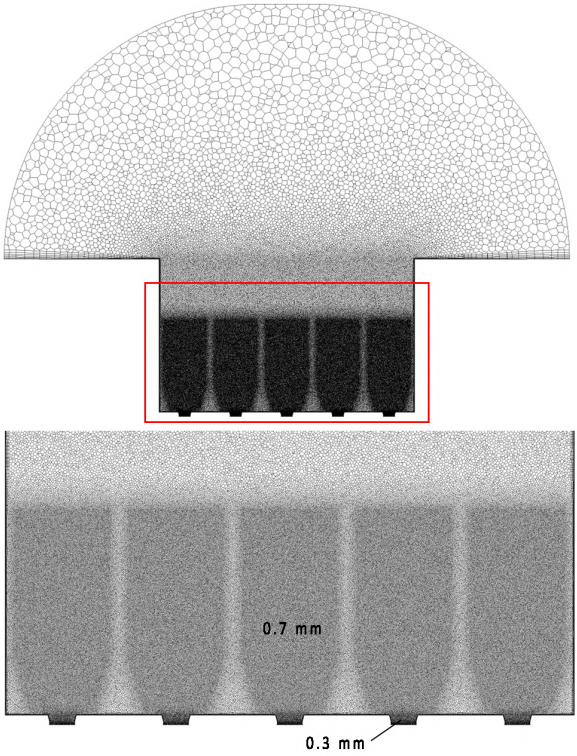

Figure 3.3: Mesh grid for the Inline case [93].

walls are treated by imposing the no-slip condition for the momentum. For the thermal boundary conditions, due to influence on the flame, the wall temperature of such walls is set to 1000 K. On the other hand, for the walls in the nozzle region, an adiabatic condition is imposed due to the minor influence on the flame.

3.2 Numerical setup for spray turbulent combustion modelling

Most published investigations on lifted flames are focused on diesel-like injectors and gaseous laboratory test-cases [45]: both configurations differ from a modelling point of view from the lifted flame expected in aeroengine applications faced by CHAiRLIFT.
This means, for instance, that the models adopted in the context of diesel spray combustion are not directly employable in current investigations. The most evident differences are the operating conditions (very high initial pressure of fuel injection) and a simpler geometry and an intrinsic time varying fuel injection process. Furthermore, diesel lifted flames involve dense spray whereas aeroengines work with dilute ones and the flame is mainly premixed in gas turbine combustors and definitely not premixed in diesel engines.
Another important difference is that flame location in diesel engines is governed by the spray cone and momentum while in aeroegines it is governed by fluid dynamics of the air flow [30]. In such conditions, liquid breakup is extremely fast and the generated spray is finely atomized, as it will be shown in Chapter 5. The combustion initiation is related to the so called ignition delay time and the developed flame is often modelled as non-premixed. Low swirl lifted flames selected for GT combustion in CHAiRLIFT are different: fuel injection is continuous and based on the airblast concept with longer and wider spray dispersion which results in a more homogeneous mixture capable to establish a well premixed flame. In fact, a premixed-like flame stabilization process is likely to occur in CHAiRLIFT concept and much more similarities are expected with the operation of gaseous lifted flames [45].
In the CHAiRLIFT concept, the most important modelling requirements are the proper description of turbulent mixing and of spray dispersion, which can be properly handled only by adopting Scale Resolving CFD (LES or Hybrid-LES). In particular the use LES and tabulated chemistry models such as the Flamelet Generated Manifold (FGM) [94] or with

the Thickened Flame (TF) model [95] has proven to accurately describe turbulent spray flames ranging from rich burn up to ultra lean conditions [33, 96, 97]. Despite the differences previously underlined, the successful use of FGM model to predict flame lift-off and auto-ignition [98] in a diesel-like spray flame, suggests that the model can also be effectively employed for the investigation of the lifted lean flames.
Nevertheless, it should be said that these flames are particularly challenging to be reproduced since the many physical effects involved in their stabilization, as explained in Chapter 2. Furthermore, the present investigation considers the whole test rig, which has a tremendous impact on the required computational efforts. All in all, in order to perform the sensitivity to the tilt angle and to carry out a preliminary assessment of the numerical modelling, a simplified description of the turbulence is required as well as cost-effective turbulent combustion models at this stage.
For this task Reynolds Average Navier-Stokes (RANS) turbulence context is considered for this numerical work with the k-ϵ Realizable model [99] for the turbulence description: this approach has been successfully applied in the literature with an overall moderate impact on the computational cost.
The other two main concerns are the spray boundary conditions, since the presence of a multiphase flow due to the liquid fuel, and clearly the combustion modelling. The next paragraphs are devoted to an introduction to such modelling choices, since their impact on the test rig simulations.

Spray boundary conditions modelling

The Discrete Phase Method (DPM) has been used to track the fuel droplets inside the domain in which the gaseous phase is treated as a continuum whereas the dispersed liquid phase is tracked in a Lagrangian framework. The spray boundary conditions have required a large part of this work for their calibration since their impact on the final solution. The liquid fuel injection is considered only from the prefilmer lip, while the whole atomization process along the prefilmer surface has not been

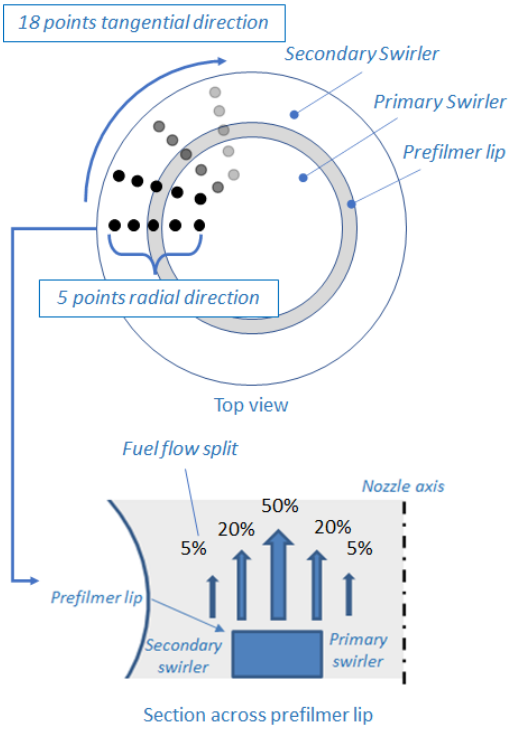

Figure 3.4: Conceptual sketch of the injection points position across the prefilmer [93].

included since the tremendous impact on the computational cost [28, 33, 36]. At this point, it is assumed that the primary breakup of the liquid film is already accomplished: concerning this, the impact of this strategy will be discussed in Chapter 5. Therefore, the injection has been distributed in several points placed 1.2 mm downstream the prefilmer lip to reproduce the spray spreading due to the unsteadiness of the flow field. A sketch of the injection points in the proximity of the prefilmer can be seen in Fig.3.4.

The total fuel mass flow rate is derived according to test point equivalence ratio and air mass flow (Table 3.1). Additionally, a flow split is applied in

Injection spray characteristic	
Spray distribution	Rosin-Rammler
SMD	63.5 μm
q	2.23
Cone angle	0 °
Droplet velocity	5 m/s
N° points in radial direction	5
N° points in tangential direction	18

Table 3.3: Characteristics of spray injection.

the radial direction as 5%-20%-50%-20%-5% of the fuel flow for a given tangential position, from the outermost to the innermost point. Each single injection point employs a Rosin-Rammler distribution [30] where the Sauter Mean Diameter SMD and Spread parameter q are derived with a correlation present in literature and suitable for prefilmer atomizer[100]. Droplets are injected with a temperature of 300 K and an initial low velocity, assuming that droplets are rapidly relaxed to the carrier phase velocity.
All the mentioned characteristics for the spray injection are resumed in Table 3.4. This procedure has been preliminary evaluated with the available spray measurements from the previous experimental campaign [68] and it will be further improved once MIE scattering experimental measurements will be available. The discrete and carrier phases are considered with a two-way coupling and secondary breakup has been modeled with the Taylor Breakup Analogy (TAB) model [101, 102], which is referred in the literature and in the technical manuals [91] to a be good choice for low Weber number injectors.

Combustion modelling

Concerning the objectives of this numerical study, a cost-effective and reliable approach for turbulent combustion modelling suitable for RANS is mandatory. In this regard, flamelets-based models with tabulated chemistry are good candidates [103].

Injection spray characteristic	
Spray distribution	Rosin-Rammler
SMD	63.5 μm
q	2.23
Cone angle	0 °
Droplet velocity	5 m/s
N° points in radial direction	5
N° points in tangential direction	18

Table 3.4: Characteristics of spray injection.

The use of the laminar flames libraries for the turbulent combustion modeling through the use of Probability Density Functions (PDF) for the description of the turbulence effects was originally proposed by Bradley et al. [104, 105]. The underlying idea is that combustion occurs in a flamelet regime where the flame front is only distorted by the turbulence and it could be described locally by laminar one-dimensional flames.
Considering the partially premixed combustion framework, one of the most popular approaches is the Flamelet Generated Manifold model [94] where a number of these flamelets are solved at pre-processing and the associated thermochemical trajectories parametrized in a look-up table as a function of two variables, the mixture fraction z (as defined by Bilger [106]) and the progress variable c. In this work, the progress variable is defined as $c = Y_c/Y_c^{eq}$, where $Y_c = Y_{CO} + Y_{CO_2}$ is the un-normalized progress variable and Y_c^{eq} is its value at equilibrium. The turbulence-chemistry interaction is taken into account by pre-integrating the look-up table using presumed β-shaped PDF (or $\beta - PDF$): the reactive process is described through the mean values of the scalar and their respective variances (i.e., $\widetilde{z}$, $\widetilde{c}$, $\widetilde{z}''^2$, $\widetilde{c}''^2$).
Hence, Assuming a statistically independence of z and c in the me, a generic turbulent quantity $\tilde{\psi}$ is computed as:

$$\tilde{\psi} = \int\int \psi(c,z) P(\widetilde{c}, \widetilde{c}''^2) P(\widetilde{z}, \widetilde{z}''^2)\, \mathrm{d}c\mathrm{d}z \tag{3.1}$$

where ψ is the corresponding laminar quantity. Therefore, two trans-

port equations are solved for mean values of mixture fraction and unnormalized progress variable:

$$\frac{\partial \overline{\rho}\widetilde{z}}{\partial t} + \frac{\partial \overline{\rho}\tilde{u}_j\widetilde{z}}{\partial x_j} = \frac{\partial}{\partial x_j}\left(\overline{\rho}D_{eff}\frac{\partial \widetilde{z}}{\partial x_j}\right) \tag{3.2}$$

$$\frac{\partial \overline{\rho}\widetilde{Y}_c}{\partial t} + \frac{\partial \overline{\rho}\tilde{u}_j\widetilde{Y}_c}{\partial x_j} = \frac{\partial}{\partial x_j}\left(\overline{\rho}D_{eff}\frac{\partial \widetilde{Y}_c}{\partial x_j}\right) + \overline{\dot{\omega}}_c \tag{3.3}$$

where $\overline{\dot{\omega}}_c$ is the mean source term of progress variable provided by the PDF table.
Additionally, two furher transport equations are solved for the variances: for the sake of brevity these equation are not reported here, while the interested reader is referred to [91].

Finally, the look-up table is queried for retrieving information about the chemical species and the flame. In this work, the progress variable source term $\dot{\omega}_c$ is modeled with a Finite Rate approach, that is the source term is taken directly from the flamelets library: this term governs the flame propagation and its correct estimation is of primary importance.

The Luche's mechanism [107] consisting of 91 species and 694 reactions has been employed for the chemistry modelling, where the n-decane ($NC_{10}H_{22}$) is used as surrogate of the JET-A fuel employed in the experimental tests. The 1D laminar flame simulations adopts $T_{mix} = T_{fuel}c_{p,fuel}z + T_{ox}c_{p,ox}(1-z)/c_{p,mix}$ as inlet temperature for the mixture, where T_{fuel} is assumed equal to T_{ox} and accordingly to the test conditions of Table 3.1, as well as for the operating pressure. Also, considering again the actual operating conditions, diffusive flamelets have been found to better describe the flames since the low air temperature limits the evaporation in the first part of the combustion chamber, hence the premix of the reactive mixture.
One of the main advantages of this approach is that detailed chemistry could be used during the pre-processing operations, thus allowing to have information of a large number of chemical species with a low computational effort at run time. However, the critical aspect consists of how this table is computed and for this reason different strategies have been

proposed [108, 109], based on different 1D structures. Concerning this aspect, some further remarks on the influence of these on the final results can be found in Appendix A for the point with gaseous fuel from the experimental campaign by Sedlmaier in [70].
Improving the accuracy of such model implies employing a look-up table with many different parameters, which could reduce the advantage of a low computational effort. It should be noticed that this approach is similar to the one employed in the previous numerical works [70, 89] for the same nozzle operated with gaseous fuel, but here the chemistry was reduced a priori to one reaction pathway, and only 6 species were involved: according to the authors, this fact is not impacting the final results unless the combustion occurs in lean conditions.

3.3 Results and discussions

In this section, the numerical simulations carried out on the full-rig configuration are reported and compared with the available experimental data. Other than validating the numerical model, the aim is to understand how a lower burner can improve the combustion stability of an upper one by the exchange of quantities (e.g. combustion products flow and related enthalpy) and how the tilt angle θ influences it.

Temperature field

The temperature field is strongly related to the outlet section configuration, especially when the tilt angle is increased. For this reason, the 45° tilt angle has been simulated for both the open and the contraction cases on the outlet plane. In this framework, the presence of an adequate buffer zone beyond the multi-burner casing itself is mandatory, since it allows the reproduction of the recirculation zones observed in the experimental campaign.

In Figure 3.5 the axial velocity is shown for the CFD simulations on the midplane, for both the open case and the one with the contraction and with zero axial velocity isoline superimposed. From this it can be

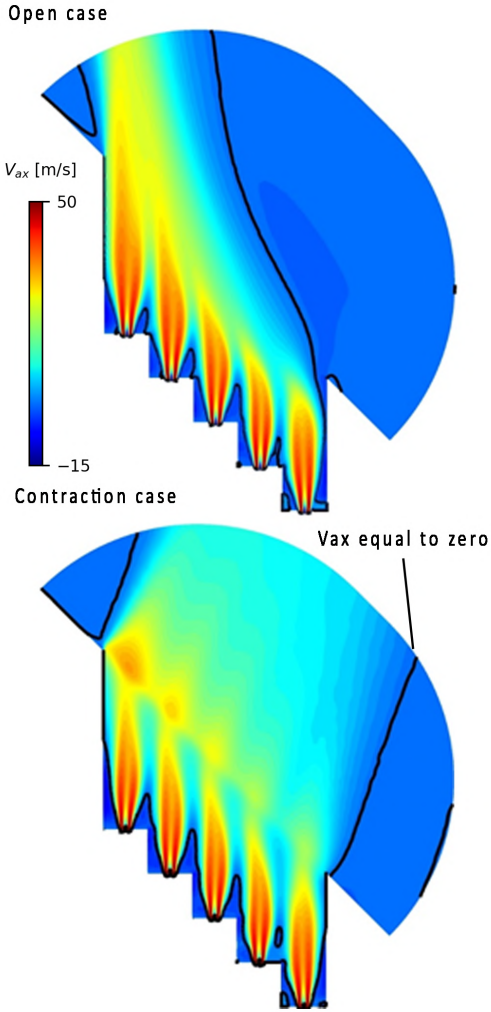

Figure 3.5: Axial velocity maps for the 45DEG configuration. Bottom: contraction case. Top: open case. Zero axial velocity isolines are superimposed.

observed how the presence of the contraction at the outlet is affecting the flow field in the entire burner. Both the configurations reproduce the high-velocity swirling jet issuing from each nozzle.
The tilted configuration promotes a cross-flow from the lowest burner to the highest: it can be observed that a non-axisymmetric flow-field is present with respect to each burner axis. This fact can be seen looking to the tip of the swirling jet, now deflected towards the side wall direction, as concluded also by Hoffmann et al. in [83].
Such effect is desired since promotes the hot exhaust gas recirculation, hence the flame stability. On the other hand, a strong three-dimensionality of the flow-field is present, and thus the complexity of the object of study. This fact also highlights that the finite configuration of the test rig, which is confined with lateral walls near the highest and the lowest burner, has a relevant impact on the final flow field. Concerning this point, by looking at the axial velocity maps for the open case configuration (top contour in Figure 3.5) the lowest burner is not supplied with a cross-flow by an eventual adjacent burner, so flow separation occurs on the lateral walls. This fact imposes a large recirculation zone that draws air from the outlet section.
Again in this picture, considering the case with contraction (bottom contour in Figure 3.5), it can be seen that the presence of this component influences the flow-field by avoiding the mentioned separation in the final part of the multi-burner. The exhausts are accelerated in the direction normal to the contracted section, hence the ambient air ingestion is avoided, as pointed out in the investigations in [82].
Keeping in mind this, in Figure 3.6 a comparison between numerical and experimental data in terms of temperature fields at the outlet section and on the diagonal of the 3rd burner is shown respectively for both Inline and 45DEG configurations. Concerning the diagonal plane, experimental measurements have been taken with thermocouples along this direction, between 50 and 250 mm in the axial direction as depicted in the sketch. It can be observed that the low-swirl lifted flame under these operating conditions (i.e., with no preheating) presents a compact inner cold region

of the swirling jet, which mixes with the surrounding hot gas downstream, thus reaching higher temperatures. The reaction zones are placed side of the jet in correspondence of the higher temperature regions, as it will be shown in the next paragraph.

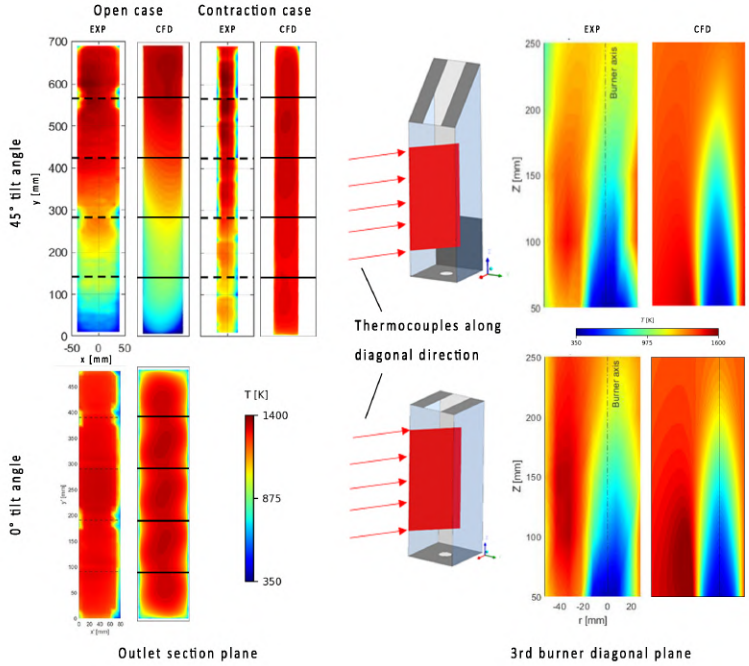

Figure 3.6: Comparison between CFD and EXP data for the temperature field at the outlet section plane and the diagonal plane for both Inline and 45DEG cases.

The considerations about flow recirculation at the outlet section are confirmed in Figure 3.6, where the experimental maps of the temperature field on this plane are compared with the numerical results, again for both configurations analyzed for the 45DEG. The open case shows a cold zone in correspondence of the lowest burner, which could not be related to the exhaust gas temperature, but clearly is due to cold ambient air ingestion.

Moving to the next burners, the temperature increases, since the effect of the recirculation is less and less visible. This behavior is completely recovered by also the CFD simulation, pointing out the good capability of the numerical in the reproduction of the main flow-field features occurring here.
Similarly, it can be seen how the presence of the contraction leads to a more uniform temperature field, where only minor ingestion of air is present in the proximity of the lowest burner, as highlighted by the lower temperature for the highest part of the outlet. Again, the numerical model is in good agreement with the experimental measurements, where also here the trend of the temperature is well reproduced moving from the lowest burner to the highest. Some differences between the numerical results and the experimental ones can be observed since a lower temperature is present in the experimental maps near the lowest burner, as well as the peak temperature is higher in this case between the 4th and the 5th burner. Instead, the CFD results are more uniform on all the outlet sections, where peaks of temperature are not reproduced: this behavior could be explained considering the RANS description of the turbulent field, where the effects due to large-scale mixing are under predicted.
The comparison in terms of temperature field on the diagonal plane of the 4th burner for the 45DEG configuration again reproduces the cold jet from the nozzle in the proximity of the burner axis: this is affected by the flow deflection previously mentioned, as visible in the EXP map.
The CFD simulation is also showing the cold jet structure near the burner axis, but the mixing with the hot exhaust occurs much earlier, and a uniform temperature field can be seen around 250 mm. Also, the jet appears less deflected concerning the experimental results, again due to the limits of the RANS approach in the representation of a swirl-dominated flow. Nevertheless, the main features of the temperature field are reproduced, such as the high-temperature region's side of the cold jet and the cold zone ending at around 140 mm.
If the Inline case is considered, for both these planes, the agreement between CFD and experiments is improved with respect of the 45DEG:

especially in the diagonal plane, approximately the same length of the coldest zone can be observed, as well as the mixing between cold jet and hot exhaust occurs in the same way around 250mm. CFD still is missing minor aspects, such as the slight offset of the main jet concerning the burner axis and the lower temperature present on the right-side region of the map.
These facts could be related to the RANS description of the flow-field, which mispredict the swirling flow in the combustion chamber, other than a not optimal description of the thermal wall boundary conditions, affecting the temperature in the side region. Also, It should be noticed that only the open case is present since this disposition of the burner does not promote any cross-flow, thus the related recirculation.

OH* chemiluminescence maps

The OH* chemiluminescence maps from the experimental campaign allow to visualize the ongoing reaction occurring in the burner, as already pointed out in Chapter 2. Since the OH* radical is not present in the employed chemical mechanism, a qualitative comparison is carried out considering the product formation rate previously introduced. Such comparison is often present in the literature, since both can be considered as indicators of the ongoing reaction.
Also, the contours are line-of-sight integrated and the LOH is evaluated as the axial position where the 10% of the global light emission is reached, according to [68, 82]. Indeed, it should be pointed out that a well-established definition of LOH in literature is not yet available, since many works are based on evaluation of the OH species concentration, instead of the the excited species OH* light emission, to detect the flame base: usually, the position of the base is placed where the OH concentration exceeds a specified threshold [42, 110]. The definition here adopted is preferred since it takes into account the hot main reaction zone, while simply considering hot combustion product concentration might be misleading due to the recirculation field near the nozzle exit [68].
The comparison between CFD and EXP data is reported in Figure 3.7:

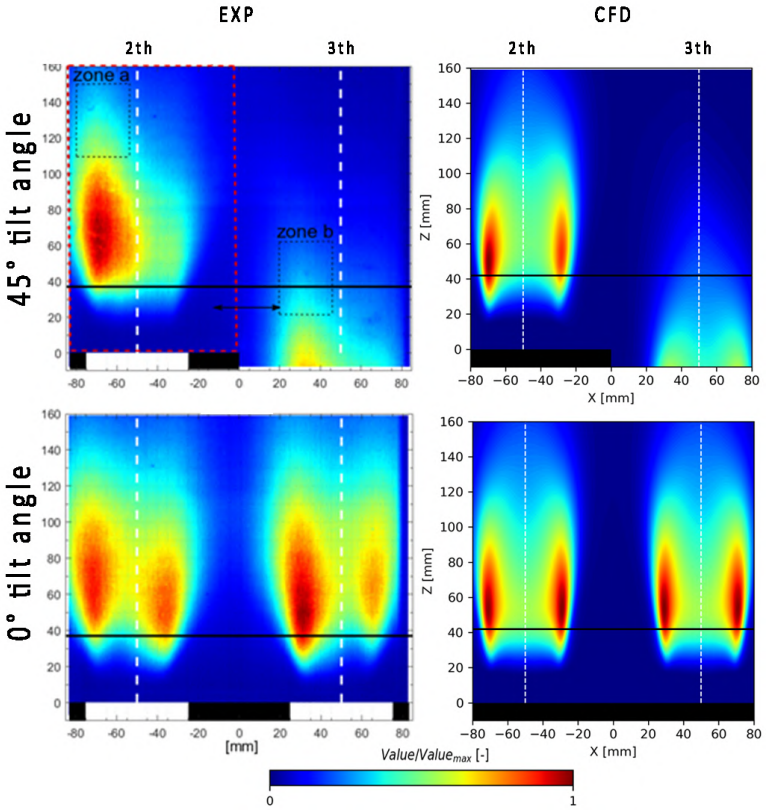

Figure 3.7: Comparison (line of sight integral) between experimental OH emission intensity map adapted from [82] and PFR maps from CFD for the 2rd and 3th burner. Top: 45DEG. Bottom: inline.*

here it is clearly visible the lift-off region devoid of reaction between the flame base and the nozzle exit. The numerical simulations successfully predict the stabilization position of the flames for both configurations, as shown from the LOH around 40 mm. Also, the CFD maps present a misprediction of the spread of the reaction zones due to the RANS approach here employed, which is not correctly reproducing the large

scale mixing and the entrainment of hot combustion products.
Nevertheless, considering the Inline rig, the flame shape is fairly well reproduced. An approximately axisymmetric shape can be observed from both numerical and experimental contours, where the main reaction zones are symmetric with respect to the burner's axis and appears as two different branches occurring on the swirling jet outer shear layer.
Instead, the 45DEG case exhibits a strong asymmetry of the main reaction zones with respect to the burner axis. A peak of reaction is present close to the sidewall region, while on the open side it is relatively weak. The simulation seems able to reproduce a reaction peak on the left side of the burner, in agreement with the EXP measurements. However, a non-negligible peak of the reaction is present also in the open side, unlike the experimental measurements. This fact could again be due to the misprediction related to the RANS approach, which is not correctly reproducing the flow-field in this region, and thus the effects of the potential wake related to the adjacent sidewall edge.
Although this fact, it can be concluded that the numerical model is able to reproduce the principal characteristics of the combustion process occurring in the multi-burner configuration, even if some limitations are present due to the modeling strategy applied to the turbulence and the combustion processes. As a concluding remark, this simulation can be employed effectively to understand the macro effects on the flame interaction due to different tilt angles, while a detailed investigation of the ongoing reactive process will require more complex models and a more detailed description of the boundary conditions.

Tilt angle effects

The numerical models introduced in the previous paragraphs have shown a good agreement with the experimental data, thus justifying the use of the same settings for the investigation of further tilt angles.
Since measurements are not available, the idea here is to provide an estimation of the tilt angle impact on the hot gas recirculation through the numerical simulations. Considering this, the investigated tilt angles

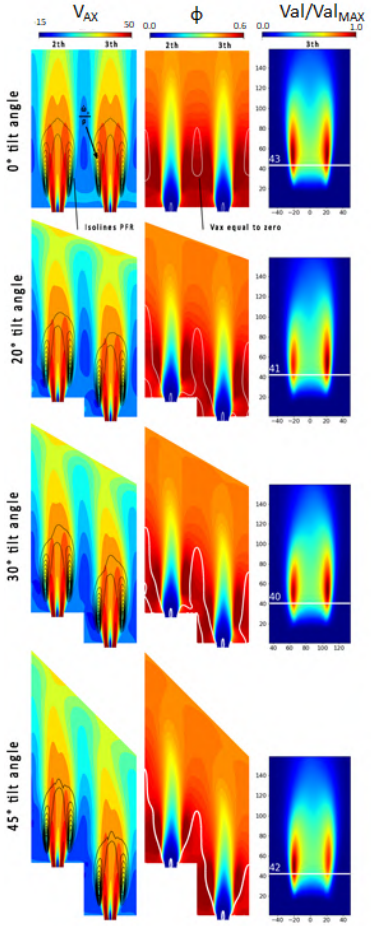

Figure 3.8: Contour maps of axial velocity, equivalence ratio (2rd and 3rd burners) and line of sight integrated maps of PFR (3rd burner) for the investigated tilt angles. The number in the figures stands for the LOH value in mm.

have been the 20° and 30° for the contraction case. In Figure 3.8, the contour maps corresponding to the 2nd and the 3rd burners are reported in terms of axial velocity and equivalence ratio. Also, the line-of-sight integrated maps of product formation rate normalized over the maximum are shown for the visualization of the reaction zones.
Firstly, all the configuration reports the same stabilization position, where the LOH assumes values between 40 and 43 mm. Still considering the previous analysis, the main reaction zones again appear at the side of the swirling jet, but a not trivial behaviour is present concerning the most reactive side. Although the limits pointed out in the previous paragraph concerning the position of these zones, it could be concluded that these regions are related to the outer shear layer between swirling jet and ORZ, as already pointed out in the previous studies for this type of flame on the single sector both experimentally [68] and numerically [90].
This fact could be observed from the axial velocity maps, where the black isolines identify the production formation rate. Accordingly to the line-of-sight-maps, the higher concentration of PFR isolines is present on the outer shear layer, where a high gradient of axial velocity is present. This is true for all the configurations, where the main difference concern only the shape and extension of the recirculation zones, as depicted from the zero axial velocity isolines superimposed on the equivalence ratio maps. An interesting finding is that the ORZ is not only present in correspondence of the sidewall, but also on the open side, and seems to interact with the lower burner with a backward transport of combustion products. This very particular situation is present for each tilt angle and could be related to the strong three-dimensionality of the flow field for this test rig. Eventually, also the Inline case, which should not present any ORZ occurrence due to the absence of walls for this view is showing some recirculation zones. Again this fact could be explained considering the presence of complex recirculation zones due to the optical windows.
Another very important point is the fact that the 45DEG configuration, which was described in the previous work on the SHC concept [76] as the most promising in terms of flame stability, with this kind of nozzle and at

least the present operating conditions is exhibiting an overall lower value of equivalence ratio, thus vitiated products transport. This fact seems related to a specific operational mode, where the flame actually is less interacting with the next burner and the sidewall operates as a barrier among burners, similarly to what has been observed in [78] for high-swirl injectors.

This point could be observed also in Figure 3.9, where the equivalence ratio, the temperature and the x velocity components are reported for the planes of the interface between 2nd and 3rd burners. It should be noticed that according to the reference system reported in the test case section, a negative value of the x velocity is associated with the mass flow from the lower burner to the higher one. Also, for each map, the dashed line represents the position of the sidewall edge.
It can be observed that the Inline case has a strong presence of hot vitiated products on these interfaces, at an axial position approximately in correspondence of the flame position. The absence of the sidewall helps in this sense, but at the same time a very little transverse transport is present, as it can be seen from the x velocity map, where low values are assumed on this plane. Nevertheless, it is interesting to see that is anyway present a transport of recirculating products entering in the plane between 0 a 50 mm, and vice versa on the other side, due to the swirled flow field of each burner.
The situation is reverted if the 45DEG configuration is considered. A strong transverse transport is present, promoting a mass flow from the lower burner to the higher one in the proximity of the optical windows. As already pointed out in Figure 3.8, a backward component of velocity is present near the sidewall edge, moving combustion products back to the lower burner. However, this configuration for the present operating conditions seems less functional, since the hot combustion products remain confined below the sidewall edge, hence limiting the interaction among adjacent burners. Finally, the 20DEG and the 30DEG are a sort of trade-off between the previously described configuration. An appreciable cross-flow is present according to the velocity maps.

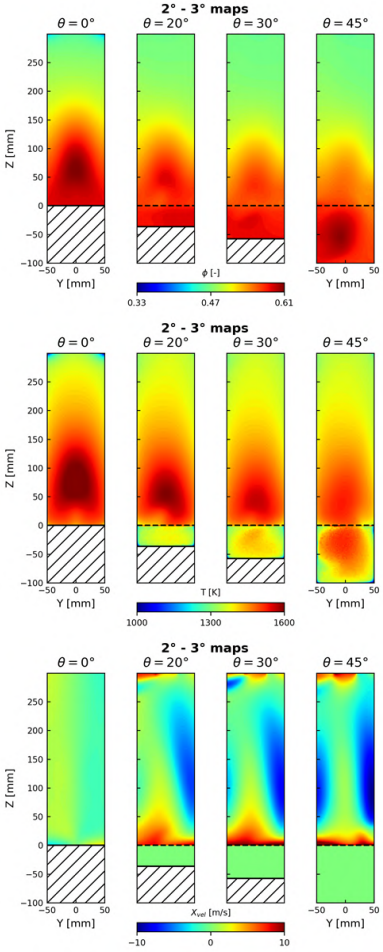

Figure 3.9: Contour maps of equivalence ratio, temperature and x-velocity on the interface planes between 2nd and 3rd burners, for the investigated tilt angles. The dashed horizontal line is the sidewall height h.

Also, the velocity is assuming a higher value between 0 and 50 mm, where the tangential flow of two consecutive burners are coherent, while

it is weakened between -50 mm and 0 mm, where these two fields are interacting one against the other. Also, the higher values of equivalence ratios, therefore of the vitiated products are above the sidewall edge and similarly the temperature field. This points out that these lower values of the tilt angle could be more suitable for the application of the CHAiRLIFT concept.

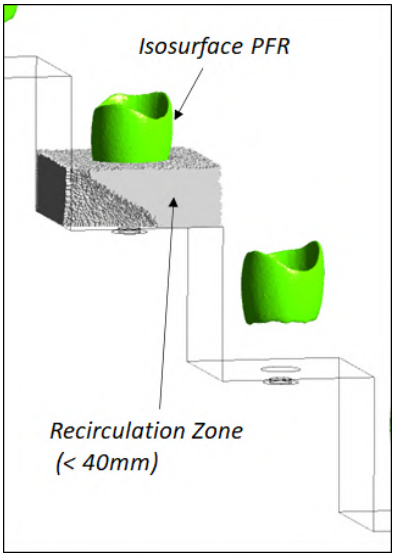

Figure 3.10: Recirculation zones sketch with isosurfaces of production formation rate (45DEG case).

Finally, some consideration can be drawn considering a series of parameters for evaluating the performance of the configuration numerically investigated so far. In this fashion, the extension of the recirculation zones as well as the volume averaged temperature in these regions is evaluated for the tested tilt angles. Also, only such regions included within 40 mm from the burner dome are considered, therefore in the lift-off region, as depicted in Figure 3.10. It is expected that these zones acts as a reservoir of hot vitiated products and participate in flame stabilization. Moreover,

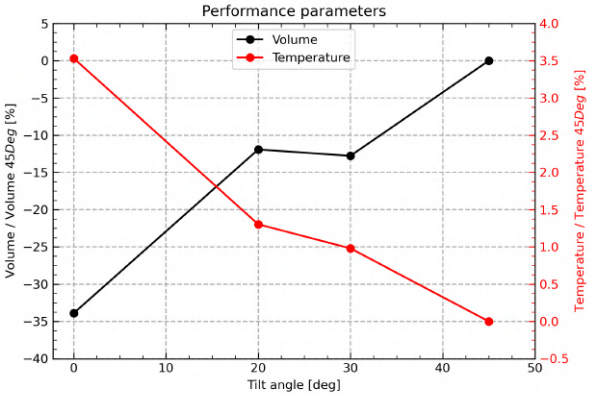

Figure 3.11: Recirculation zones extension and related volume averaged temperature for the investigated tilt angles.

only the mid burner is considered, assuming it could be considered as the one less influenced by the lateral confinement.
The results are reported Figure 3.11 and adimensionalized on the 45DEG value. These results confirm the previous observation since the Inline case has the smallest extension of the recirculation regions but also the highest temperature with respect of the 45DEG configuration. The 20DEG and 30DEG case are instead comparable and present a good extension of the recirculation zones, especially with respect to the Inline case. Meanwhile, also the average temperature is better than the 45DEG configuration, even if not so far from this value.

3.4 Extension to preheated conditions

In this chapter so far the CHAiRLIFT test rig in multiburner configuration has been numerically investigated for different values of the tilt angle. The whole rig has been modeled in order to understand the mutual interaction of adjacent flames when low-swirl lean lifted spray flames are

arranged with a tilted disposition of the burners.
These studies have shown that the numerical modeling strategy, allows reaching a good agreement with the experimental data when the full rig configuration is considered. The numerical simulations point out that tilting angles between 20° and 30° could lead to a stronger recirculation and in general better flame stability. A further improvement will be represented by the review of the employed boundary conditions once PIV measurement of the flow-field will be available from the ongoing experimental activity.
However, it should be noticed that some difficulties can potentially arise when preheated test points are considered, which are clearly more representative of a real engine cycle. In this situation, the combustor is expected to operate in a full premixed mode, since the higher air temperature will allow the earlier evaporation of the droplets and thus reach an air-fuel fully premixed mixture before the flame front.
This scenario is desired concerning the goal of the CHAiRLIFT project but leads to some challenges from the numerical modelling point of view. Actually, premixed combustion is found to be more sensitive to heat loss and aerodynamic stretch of the flame front with respect to the non-premixed one [103]. For the same reason, lean burn combustors are more susceptible to combustion instabilities, as described in Chapter 1. Indeed, the latter case, concerning the current burner, is more related to spray distribution in the chamber, since the position where it evaporates and mixes with the air determines the stabilization position of the flame.
Excluding the influence of the liquid fuel, the modelling of turbulent premixed combustion for a low-swirl lifted flame remains still difficult. This is even more true if a cost-effective approach from the computational efforts point of view is desired. Last but not least, concerning this research activity, detailed information in the involved chemistry, especially concerning the NO_x formation should be included. Summarizing, the FGM approach should fulfill many of these points, but its effectiveness concerning the description of a lifted flame in preheated conditions should be assessed before.

Operating pressure p_0	400000 Pa
Air inlet temperature T_0	573 K
Nozzle pressure drop $\Delta p_{nozzle}/p_0$	3 %
Equivalence ratio ϕ	0.52
Fuel type	Gaseous (Methane)

Table 3.5: Operating conditions adopted in the numerical simulations on the single sector in reactive conditions.

An example for such behaviour can be observed considering the LES investigation carried out in [90], which followed the isothermal investigation introduced in Chapter 2.
In this case methane was employed as fuel with for an overall air-fuel equivalence ratio of $\lambda = 1.91$ (i.e., $\phi = 1/\lambda \approx 0.52$), while the operating pressure was set to 4 bar and an air inlet temperature T_{in} to 573K. The pressure drop across the nozzle instead was maintained at 3%, as in the isothermal conditions. These conditions are summarized in Table 3.5. This test point has been selected among the ones available in [70], where also instantaneous images of OH-PLIF were available other than OH* chemiluminescence maps.

This numerical investigation employed the FGM model with freely propagating flamelets for the manifold, and an extended version of the FGM (referred as FGM-EXT) able to include the local quenching effects due to stretch and heat loss. Thanks to this modification, the latter model can reduce the reaction rate source term (i.e., $\dot{\omega}_c$) from the one of the unmodified FGM to 0, corresponding to the local quench occurrence. A detailed description of such approach will be given later in Chapter 4.
The GRI3.0 detailed mechanism [111] with 325 reactions and 53 species is used for the table computation through freely propagating premixed flamelets and it is discretized with $64x32$ points in terms of respectively z and c. In Figure 3.12-Left the numerical results are presented as line-of-sight integrated maps and compared with the EXP data, where the LOH is evaluated as in Section 3.3.

The measured LOH of 70mm is missed by both numerical models pre-

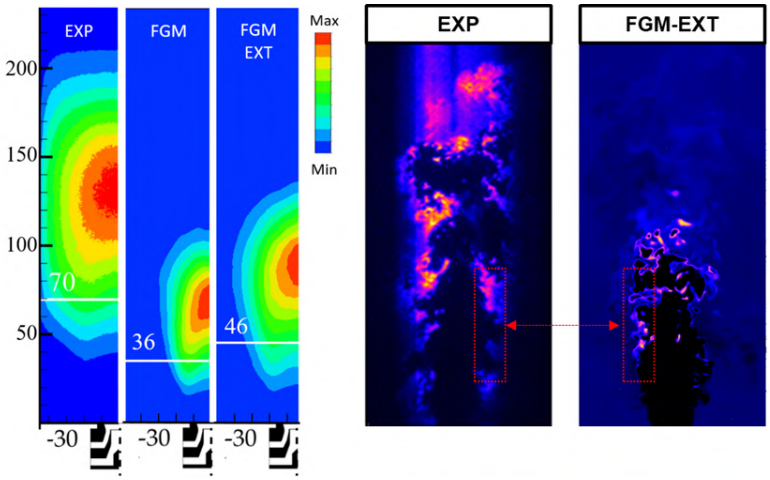

Figure 3.12: Left: Comparison (line of sight integral) among experimental OH emission intensity map and PFR maps obtained from the unmodified FGM approach and the corrected approach[90]. The number in the figures stands for the LOH value in mm. Right: Instantaneous snapshot of EXP measured OH-PLIF maps and OH mass fraction from CFD (first 200 mm of the flame tube). The red boxes highlight the OH radical presence at the flame base.*

dicting respectively 36mm and 46mm. The underestimation of the LOH is a result of the reactivity over-prediction concerning the real physics of the problem, which results in a flame stabilizing more upstream with respect to the expected position. This fact is also confirmed by the shape of the flame: the numerical approaches show a reduced length of the flame both in the axial and radial direction, while from the experimental contours, the flame is far longer and reaches the confinement walls. Nonetheless, the use of the stretch and heat loss correction allows a prediction closer to the experimentally observed flame shape and an increased value of the LOH compared to the classic approach. This implies the importance of including quenching effects for a correct representation of the flame.
Concerning the reproduction of the stabilization process, a set of compre-

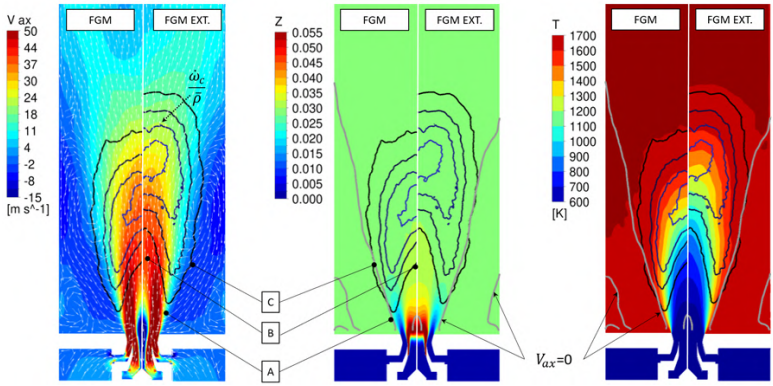

Figure 3.13: Contours of mean axial velocity (left), mean mixture fraction (mid) and mean temperature (right) in reactive case. the solid grey line stands for the zero axial velocity isoline while the progress variable source term isolines are reported for the flame visualization. Labels A, B and C refer to the flow regions described in the text.

hensive contour maps are reported in Figure 3.13 and Figure 3.12-Right. The former reports the averaged flow-fields, reported for both the approaches in Figure 3.13, in terms of axial velocity, mixture fraction, and static temperature. Here, the isolines of the normalized source term of the progress variable per unit mass are superimposed on the iso-contours, showing the flame position on that plane. Additionally, the axial velocity iso-contours reports also the velocity vector field, while only the zero axial velocity isoline is present on the mixture fraction and temperature contours. Finally, each map reports on the left side the results coming from the standard FGM approach and the ones from the extended approach on the right.

Considering the flame leading edge (labeled with A in Figure 3.13), it can be seen that its time-averaged position occurs on the outer side of the swirling jet shear layer, in a fairly premixed region, where hot combustion products recirculate upstream and allow the flame stabilization. The outer recirculation zone is therefore responsible for the leading edge

anchoring in a lean region of the mixture fraction field, in agreement with the experimental observations. Meanwhile, the inner zone of the jet (label B) presents high-velocity magnitudes, which push the flame front downstream notwithstanding the local richer mixture fraction.
Starting from the flame leading edge and moving downstream, the flame follows the expansion of the jet stream in the radial direction (label C): here, the first non-negligible progress variable source term isoline is located along the zero axial velocity isoline. In this region, the hot combustion products operate a continuous re-ignition process of the fresh mixture, as pointed out in the experimental OH-PLIF images (Figure 3.12-Right), as well as of the previously quenched gas pockets. It should be noticed that a similar mechanism has been observed also for lifted jet flames in co-flowing air [45]. The combustion process is then completed and the two isolines separate before reaching the confinement wall.
In conclusion, these results confirm that the fundamental stabilization mechanism pointed out from the experimental campaign is caught with both the combustion models, while a probable cause of the wrong LOH prediction is due to a low magnitude of the stretch and heat loss effects. Nevertheless, the FGM models have demonstrated to be not adequate for a correct reproduction of the flame. In order to understand better the reasons for such misprediction, in the next chapter a sensitivity to the combustion modelling within some of the most popular approaches within LES framework is carried out.

Chapter 4

Reactive conditions simulations with gaseous fuel

The outcomes of the numerical simulations reported in Chapter 3 justify a further investigation of the turbulent combustion modelling adopted to describe this type of lifted flames. In this sense, this chapter is devoted to explore and understand further numerical models with respect to the already employed FGM, according to the overview given in Chapter 2. Indeed, as already mentioned, different operating conditions could lead to the need for a totally different strategy for the numerical modelling. Furthermore, it is known in the literature that the FGM approach overestimates the reactivity [39, 112], leading to a flame stabilizing close to the nozzle outlet. Keeping in mind this, here a different test case is considered where the flame is operated with gaseous fuel with shame injector concept, where the aim of the present chapter is therefore to understand the limitations of two of the most popular turbulent combustion LES models applied in the GT field: the already introduced FGM and TF models. Also, this analysis is reported and discussed in detail in [113]. Since the standard FGM model has already proven to be not adequate to model these flames, a modified version of this approach including stretch and heat loss effects is also described. Such model has been introduced

as well in Chapter 3, but now different thermal boundary conditions are employed. In this fashion, some further considerations can be drawn, excluding a possible misprediction due to improper wall thermal boundary conditions. Moreover, the use of a gaseous flame will allow in a first attempt to exclude the influence of the liquid fuel in the numerical modelling, which clearly adds further complexities and challenges to the investigation.
Keeping in mind these aspects, in the following the employed combustion models are described, except for the standard FGM, already introduced in Chapter 3.

4.1 Flamelet Generated Manifold Extended model

Aiming to improve the FGM model predictions, many efforts have been put by the scientific community into the inclusion of the quenching effects due to local aerodynamic stretch and heat losses on the flame front. Several strategies have therefore been carried out, but basically, they could be divided into two different subgroups, as resumed also by Tang and Raman in [114]: the direct inclusion of stretch and heat loss in the manifold by increasing its dimension; the correction of the FGM reaction source term with a scaling factor, while the original manifold is kept.
The first approach is theoretically the most correct, but it leads to complex strategies to carry out the look-up table and usually a very large manifold. These aspects could impact the computational effort required at runtime and also its implementation in the CFD solver is not trivial. To limit the number of variables required for the tabulation, sometimes only the heat loss is considered without the stretch [115, 116, 117] or the assumption of a fully premixed regime (i.e., avoiding the need for $\widetilde{z}$ and $\widetilde{z}''^2$) is made [114].
The second approach is instead more simplistic since only the reaction rate takes into account the effects of stretch and heat loss: the scaling is obtained through the ratio of the laminar flame speed from un-strained and

adiabatic flamelets to the one from non-adiabatic strained flames. Also, the use of such scaling factor requires some assumptions depending on how it is defined, which rarely can be generalized for all the possible operating conditions. All in all, this strategy is quite straightforward to implement but at the expense of a less robust theoretical background. A further discussion of the advantages and drawbacks of these two approaches is out of scope in the present work, while a very detailed description of these strategies with the related references is present in [114].

Since here the second approach is used, the focus is on the previous works which followed such strategy. In particular, the idea of applying a scaling factor to the reaction rate model was originally proposed by Tay-Wo-Chong et al. [118, 119] with the Turbulent Flame Closure model by Zimont [120] as well as a model developed at KIT-EBI [121]. Most recently, the same approach has been applied in the work of Kutkan et al. [122] for flames employing blended methane-hydrogen mixtures. Also, a further development has been carried out by Klarmann et al. concerning the Finite Rate closure for the progress variable equation [112, 123, 124]. Both these approaches were developed originally for RANS turbulence framework.

Considering the formulation by Klarmann et al., the mean progress variable source term $\overline{\dot{\omega}}_c$ is multiplied for a reduction factor $\Gamma_{\kappa,\Psi}$ ranging between 0 and 1. In this fashion, all the scenarios are represented, respectively from the local quenching to the unmodified reaction. The reduction factor is evaluated at run-time with the following expression:

$$\Gamma_{\kappa,\Psi} = \left(\frac{S_c(\kappa, \Psi, z)}{S_c^0(z)} \right)^m \tag{4.1}$$

where S_c is the consumption speed related to the stretched and non-adiabatic flamelet for a given value of stretch κ, heat loss Ψ, and mixture fraction z, while S_c^0 is the consumption speed referred to the same flamelet in un-stretched and adiabatic conditions. A power-law is present with a coefficient m, defined starting from the maximum of the reaction rate and the consumption speed in strained and non-adiabatic conditions as:

$$m \approx \frac{log(\dot{\omega}_c(\kappa, \Psi, z))}{log(S_c(\kappa, \Psi, z)} \tag{4.2}$$

This term is evaluated from laminar simulations and it has shown that it assumes a constant value considering the type of fuel and the operating conditions [124]. The effects of stretch and heat loss on the consumption speed can be observed in Figure 4.1, where isosurfaces of S_c are reported at fixed value of strain, heat loss and mixture composition. While $S_c^0(z)$ is derived from the FGM look-up table, $S_c(\kappa, \Psi, z)$ is computed a priori and stored in an additional table. This latter tabulation is obtained from one-dimensional laminar flames considering a from premixed counterflow flamelets (i.e., fresh to equilibrium products) with the Cantera v2.4.0 libraries [125] and stored in an additional table. Stretch and heat loss are imposed respectively by varying the velocity of the opposed jets and the temperature of the burnt gas side. At run-time, this table is accessed using the stretch and the heat loss values computed in the CFD simulation, other than the local composition. In this work, the consumption speed table consists of $249x38x200$ points, respectively of z, Ψ and κ.

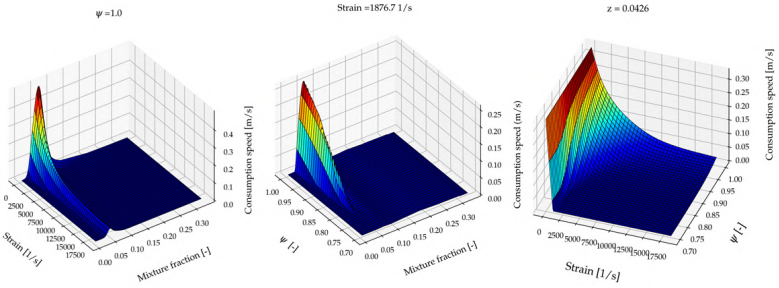

Figure 4.1: Isosurfaces of consumption speed for fixed levels of heat loss, strain and mixture fraction.

The differences between the heat loss modelling adopted in the present work (other than in the ones in [90, 126]) and the works by Tay-Wo-Chong and Klarmann with respective co-workers are due to two aspects.
First, since the use of LES turbulence modeling context here adopted, a

different formulation for the computation of the aerodynamic stretch is required. Assuming a thin front the flame stretch κ (i.e. the rate of the flame surface variation per unit area), is defined as [103]:

$$\kappa = \frac{1}{A}\frac{dA}{dt} = (\delta_{ij} - n_i n_j)\frac{\partial u_i}{\partial x_j} + S_l \frac{\partial n_i}{\partial x_i} = a + \sigma_c \tag{4.3}$$

where A is the flame surface, δ_{ij} is the Kronecker's delta, n is the unit vector normal to the front and S_l the laminar flame speed. The stretch is thus due to the separate contribution of flame strain a, i.e. the fluid strain rate tangential to the flame front, and the curvature of the flame front σ_c. In LES framework, the above definition can be filtered and the two terms of a and curvature σ_c distinguished. Applying the filter to the strain definition leads to [119]:

$$\tilde{a} = (\delta_{ij} - \widetilde{n_i n_j})\frac{\partial \tilde{u}_i}{\partial x_j} + \left[\widetilde{\delta_{ij} - n_i n_j}\frac{\partial u_i'}{\partial x_j}\right] = \tilde{a}_{res} + \tilde{a}_{sgs} \tag{4.4}$$

The filtered strain is thus evaluated as sum of the strain induced by the resolved and sub-grid flow structures. The resolved part can be extrapolated from the fluid strain rate, removing the component normal to the flame. This operation can be carried out by computing the flame front normal unit vector from the progress variable $\tilde{c}$ field as:

$$n = -\frac{\nabla \tilde{c}}{||\nabla \tilde{c}||} \tag{4.5}$$

The other contribution to total strain (Equations 4.4) is the part associated to the sub-grid turbulent motions, which requires specific modellings. In this work, it is expressed in terms of the sub-grid time scale and corrected with an efficiency function Π_k:

$$\tilde{a}_{sgs} = \frac{\Pi_k}{\tau_\Delta} \tag{4.6}$$

The correction Π_k accounts for the reduced influence of the smallest turbulent eddies to strain the flame front because their lifetime is not long

enough to affect significantly the combustion process. By fitting DNS data, Meneveau et al. [127] proposed the following formulation for the efficiency function:

$$\log_{10}\Pi_k = -\frac{1}{s+0.4}e^{-(s+0.4)} + \left(1 - e^{-(s+0.4)}\right) \tag{4.7}$$

$$s = \log_{10}\left(\frac{\Delta}{\delta_l^0}\right) \tag{4.8}$$

$$\sigma = -\frac{2}{3}\left(-\frac{1}{2}exp\left[-\left(\frac{u'_\delta}{S_c^0}^{\frac{1}{3}}\right)\right]\right) \tag{4.9}$$

where δ_0 and S_c^0 stand for the un-stretched laminar flame front thickness and consumption speed respectively and u'_Δ the sub-grid velocity fluctuation, modeled as:

$$u'_\Delta = \frac{\nu_t}{C_s\Delta} \tag{4.10}$$

Combining the set of Equations 4.4–4.9 the local strain of the flame front can be evaluated at any time. Nevertheless, the flame stretch definition requires the calculation of the front curvature σ_c. Despite in previous LES studies it was not modelled [33–35, 37], in this work this contribution was included by filtering its definition:

$$\tilde{\sigma}_c = S_c^0\frac{\partial\tilde{n}_i}{\partial x_i} = S_c^0\nabla\cdot\tilde{n} \tag{4.11}$$

Note that the un-stretched laminar consumption speed is considered among the different laminar flame speed definitions. The curvature contribution is algebraically added to the strain to evaluate the flame stretch, which is then clipped to zero consistently to the non-negative values recorded in the laminar database.

The other key quantity, the heat loss parameter, requires instead some further clarifications concerning its computation. First of all, it should be noticed that the heat loss imposed in the 1D flames simulation for computing the S_c table is modeled through the temperature of the burnt

gas (i.e., $c = 1$ side) in the counterflow flamelets, as reported previously. This approach is the same employed by Tay-Wo-Chong et al., as well as Klarmann et al., Tang and Raman, and other works in the literature [112, 114, 115, 118, 119, 123, 124]. What differs from these works is how the heat loss is computed within the CFD calculations for the querying of the table for the consumption speed in strained and non-adiabatic conditions. Here, the heat loss parameter Ψ has to be adapted to the tabulated chemistry approach with respect to the definition used in the 1D simulations. Indeed, here the heat loss is referred to the products of the laminar counterflow flamelets that means $\widetilde{c} = 1$ and $\widetilde{c}^{''2} = 0$. In the CFD instead, it should be formulated accordingly to the overall progress variable field, so it is expressed as the ratio of the local temperature to the local adiabatic temperature:

$$\Psi = \frac{T}{T_{eq}} \cong \frac{T\left(\widetilde{z}, \widetilde{z}^{''2}, \widetilde{c}, \widetilde{c}^{''2}, h\right)}{T_{ad}\left(\widetilde{z}, \widetilde{z}^{''2}, \widetilde{c}, \widetilde{c}^{''2}, h_{ad}\right)} \tag{4.12}$$

It can be seen that with this definition $\Psi = 1$ in the fresh mixture, since here $\widetilde{c} = 0$ and $\widetilde{c}^{''2} = 0$. This fact will be explained later in the results section where the Ψ field always is assuming a value close to 1 in the swirling jet near the nozzle outlet, which is dominated by the fresh mixture. As well, in the corners, low values of Ψ are reached, since here the local temperature is considerably far from the associated adiabatic flame temperature.

Concerning the works in the literature by Tay and Klarmann, the heat loss parameter was instead defined with the enthalpy defect $\Delta h = h - h_{ad}$, where h is the local enthalpy and h_{ad} is the one from the look-up table. This fact was already commented in [90] and it is assumed that the two approaches are equivalent in the framework of non-adiabatic FGM since the thermochemical quantities are included in the manifold in the function of the enthalpy defect with respect to adiabatic conditions. Also, the fact that the present definition is adimensionalized does not represent an issue since it is used only as a parameter to access the consumption speed additional table.

This approach has already shown its potential in the mentioned works [90, 126] available in the literature, but it should be recalled that the flame structure tabulated in the manifold is not affected, while it has shown that the levels of heat loss and stretch could largely impact the flamelet response [114]. This approach leads to a robust implementation of the heat loss correction with the standard FGM model in the ANSYS Fluent solver while retrieving the same physical effects concerning the quantification of the heat loss with respect to the look-up table, since the estimation is obtained by directly accessing the database (for the adiabatic temperature) and the local one, instead of solving an additional expression.

4.2 Thickened Flame model

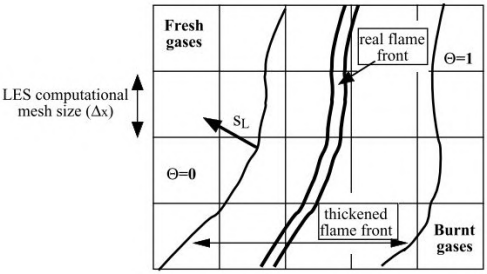

Figure 4.2: Sketch of Thickened Flame approach concept (adapted from [103].

In the Artificially Thickened Flame model [95], or most commonly, just Thickened Flame (TF) model, no assumptions on the combustion regime are made a priori and the flame front is directly resolved. For this reason, one transport equation for each chemical species involved is present. The problem when trying to resolve the flame structures is that the flame front is considerably smaller than the usual mesh grid size: the thickening procedure alters the flame front in order to be solved on the actual mesh grid.

During this operation, the correct laminar flame speed is preserved by increasing the thermal diffusivity and decreasing proportionally the reaction rate through the introduction of a thickening factor F, which is a function of the mesh grid size Δ and the laminar flame thickness δ:

$$F = \frac{N\Delta}{\delta} \tag{4.13}$$

N is instead the number of points into which the flame front is discretized, which is set to 8 in this work.
This operation however affects the interaction between chemistry and turbulence, since the eddies smaller than the thickened front are not interacting properly with the flame [103]. In order to mitigate this issue, the reaction rates and the thermal diffusivity are multiplied by the efficiency function E, defined as the ratio of the flame wrinkling factors for the original flame and the thickened one: here, E is computed following the formulation given by Colin et al. [95].
Furthermore, since the thickening procedure could lead to erroneous mixing and heat-transfer, the flame is dynamically thickened only in the proximity of the flame front, through the use of a flame sensor Ω, assuming its value equal to 1 in the regions of interest and 0 away from them [128]. All the reaction rates in the species transport equations and the source term in the energy equation are therefore multiplied by E/F, as follows:

$$\overline{\dot{\omega}}_{k,TF} = \frac{E}{F}\dot{\omega}_{k,lam} \tag{4.14}$$

where $\dot{\omega}_{k,lam}$ is the source term of the generic $k-th$ species evaluated with the Arrhenius law as $\dot{\omega}_{k,lam} = AT^{\beta}exp(-E_a/RT)$.
The species diffusivities are dynamically computes instead as

$$D_{eff} = D_{lam}(1 + (EF - 1)\Omega) + D_{turb}(1 - \Omega) \tag{4.15}$$

where D_{lam} is the laminar diffusivity and D_{turb} is the turbulent one. In this fashion, near the flame Ω is equal to 1, hence the turbulent diffusivities are neglected while the laminar diffusivities are enhanced by EF. Instead, away from the reaction front, the expression $D_{lam} + D_{turb}$

is retrieved and thickening is switched off. This approach has been widely applied in literature for both premixed and non-premixed flames [128] and nowadays is one of the most popular approaches for combustion modeling concerning scale resolving simulations.
The TF model is often used together with global or semi-global [129] chemical mechanisms to reduce the number of transported species, therefore mitigating the required computational effort. In this first attempt to apply the TF model to the low-swirl gaseous lifted test case, the BFER 2-step mechanism for air-methane mixtures developed by Franzelli et al. [130] is used. This reaction mechanism considers six species with a first reaction concerning the oxidation of the fuel into carbon monoxide, while the second reaction takes into account the final $CO - CO_2$ equilibrium. Each reaction follows the Arrhenius law with the introduction of two dedicated parameters, f_1 and f_2 respectively for calibrating the laminar flame speed for rich flames and the thickness of the post-flame zone.

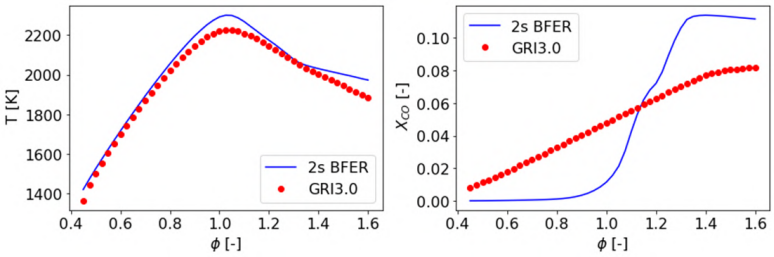

Figure 4.3: Adiabatic flame temperature (left) and CO mole fraction (right) in function of the equivalence ratio for the conditions of Table 4.1 from freely propagating flamelets simulations with detailed (GRI3.0) and Semi-Global (2S-BFER) chemical mechanisms.

This mechanism has been largely employed in literature considering the LES modelling context, showing how it could successfully predict the fuel oxidation and the temperature field in the combustion chamber. However, as many reduced mechanisms, the underlying idea is to carry out a correct estimation of the laminar flame speed and adiabatic flame temperature, rather than the concentration of the intermediate chemical species [129]

or potential autoignition phenomena [131]. Especially considering the CO prediction, a poor agreement is expected in comparison with a more detailed mechanism from a quantitative point of view: this fact can be seen in Figure 4.3, where the adiabatic temperature and the CO mole fraction are reported for the BFER and the GRI3.0 mechanisms simulated with a freely propagating 1D flame in Cantera for the operating conditions in Table 4.1. More details concerning these aspects are available in [132].

4.3 Experimental test rig

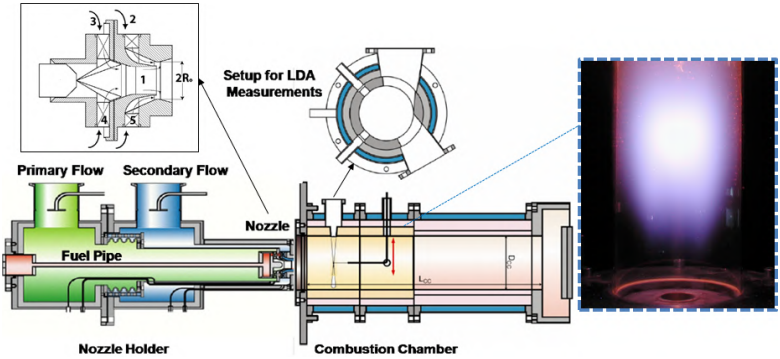

Figure 4.4: Experimental test rig and low-swirl nozzle concept investigated by Fokaides adapted from [65].

The test rig here considered employs a confined low-swirl lifted flame investigated by Fokaides et al. at KIT-EBI [64, 65]. In fact, this configuration is almost identical to the one already reported in Chapter 2 for the investigation of Sedlmaier J., where the main difference consists in the available measurements set and the effective area of the nozzle. Therefore the same radial double-swirl nozzle with $S_{th,o} \leq 0.4$ is employed with the methane injection, as shown in Figure 4.4.

During the experimental campaign, two different facilities were employed, respectively for atmospheric pressure conditions and elevated pressure combustion: here only the former is considered. The test rig

provided of a cylindrical combustion chamber where both gaseous and liquid fuel can be employed. The diameter D_{CC} is four times the throat diameter of the nozzle diffuser $2R_0$ and the outlet section is placed at a distance L_{CC} equal to four and half times D_{CC} from the chamber bottom. Moreover, the outlet section geometry is designed to avoid back-flow recirculation.
The main section consists of a water cooled ceramic segment, while different additional segments can be employed allowing the specific measurement techniques. Flow-field measurements are carried out by applying LDA technique, thanks to two aligned silica-glass for the optical access, for both isothermal and reactive conditions.
Again concerning the reactive conditions, local species concentration in the combustion chamber is evaluated through gas sampling with a suction probe, then analysed with conventional gas analyses based on molecular excitation process. In this fashion, spatial maps of chemical species such as carbon monoxide (CO), carbon dioxide (CO_2) and methane (CH_4) are available for the lift-off region and the main reaction zone. Finally, temperature measurements are obtained thanks to S type compensated micro thermocouple probes corrected for radiative heat losses.

Table 4.1: Lifted flame experiment operating conditions by Fokaides et al.

Operating pressure p_0	101325 Pa
Air inlet temperature T_0	373 K
Air mass flow $\dot{m}_{air}$	0.0185 kg/s
Nozzle pressure drop $\Delta p_{nozzle}/p_0$	2 %
Equivalence ratio ϕ	0.65
Fuel Type	Gaseous (Methane)

The operating point studied here is summarized in Table 4.1. A lean global equivalence ratio ϕ equal to 0.65 is employed to investigate the flame stabilization and capability.

Numerical setup

The numerical investigation has been conducted within the LES context in order to provide a proper description of the turbulent structures present in the flow-field. As in Chapter 2 Spatially-filtered compressible Navier-Stokes equations are employed within the CFD suite ANSYS Fluent 2019-R1 [91]. As well, spatial and temporal discretization adopted second-order schemes while the Dynamic Smagorinsky-Lilly model [92] is used for the subgrid stress tensor.

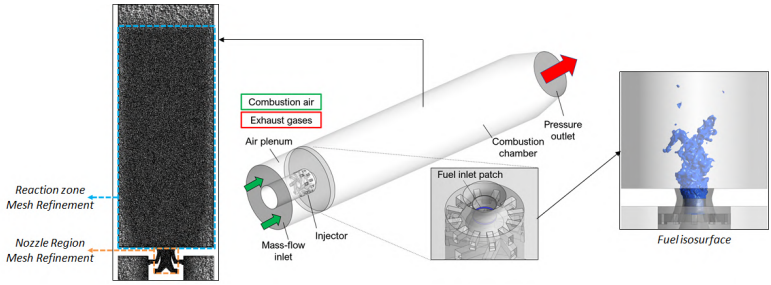

Figure 4.5: Sketch of the CFD numerical domain with mesh grid. Blue box: flame tube local mesh refinement. Orange box: swirler local mesh refinement.

The numerical domain, reported in Figure 4.5 has been derived from the simulations in [90] and described in Chapter 2 where an injector with the same configuration, but lower effective area was employed.
The previous study investigated both isothermal and reactive conditions and a good agreement was obtained between numerical results and experimental data for the flow-field in cold conditions. Therefore here the efforts have been focused on the only reactive point to assess the differences among the combustion models, assuming that the numerical setup can properly reproduce the flow structures when no reaction is occurring.
One of the main challenges of the present test case is the large extension of the reaction zone and its interaction with the confinement walls, which imposes a wide region with local refinement and thus limits the

magnitude of the refinement itself. It is worth recalling at this point that this numerical study aims to investigate how different combustion models are reproducing the flame characteristics. Therefore a robust and affordable computational grid is required at this stage, while a complete study comprehensive of mesh sensitivity is left to future works when focusing on a single combustion model.
Keeping in mind this, an unstructured polyhedral mesh with 16 million elements is employed since it is considered a good compromise in terms of both computational efforts and accuracy. Two distinct refinement regions are present: one within the swirler and the other in the flame tube (see Figure 4.5). The latter region has a maximum diameter of 85 mm for both the FGM simulations, while it reaches the chamber walls for the TF model. As result, a different mesh sizing for these simulations is used, in order to meet the target overall number of elements. Therefore, the FGM models employed 250μm in the swirler and 500μm in the flame tube, while the TF model considers respectively 500μm and 600μm. This fact helps to avoid a too large value of F in the reaction zone, leading to better reproduction of the turbulence effects on the flame front. Finally, both the setups are including 5 prismatic layers for near-wall treatment. Furthermore, the study in Chapter 2 adopted a coarser mesh than the actual employed here, but still quite reasonable results for both mean and fluctuating components of the velocity were obtained in isothermal conditions: therefore it is assumed that at least the same accuracy could be retrieved within this work. Some further details are reported in Appendix B.
A preliminary estimation of the calculation grid adequacy is carried out with the LES Quality Index by Celik [133], where the capability of both the mesh grids to properly describe the flow-structures is assessed when a value greater or equal to 0.8 is obtained. Clearly, this is not a substitute for a mesh sensitivity study, but still, it represents a preliminary indicator of mesh adequacy within the scientific community [134], especially when dealing with a test case which has not been investigated widely before, therefore little experience is available concerning its numerical modeling

(e.g., maximum element size within the nozzle for an acceptable turbulent field description). Keeping in mind this, in Figure 4.6, it can be observed that the criterion is met in the whole domain for both the configurations, where clearly the lowest values are present at the nozzle exit.
Instead, focusing on the Thickened Flame approach, another important indicator of the mesh adequacy concerning the operating condition is the magnitude of the thickening Factor F. When this quantity is too large, it could lead to an improper description of the turbulence chemistry interaction, as introduced earlier discussing this combustion model.

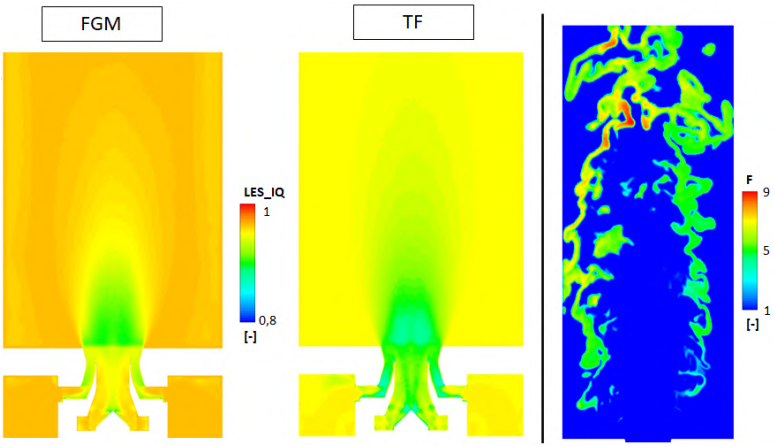

Figure 4.6: Contour maps of mean LES quality index by Celik [133] for the FGM and the TF simulations (left) and instantaneous value of thickening factor F (right).

Since the present work, as far as the authors are aware, represents the first attempt to apply the Thickened Flame model to this burner, particular attention has been paid to reproduce the acceptable magnitude of F. In this fashion, the actual mesh grid seems aligned with the value for F suggested in the literature [103]. This can be observed in the contour map of F is reported again in Figure 4.6, where the largest part of the structures are assuming a value of 5, while some peak values are present

for such pockets of gas with richer composition (i.e., smaller laminar flame thickness).

Concerning the boundary conditions, a mass-flow inlet is used for the air plenum, while a pressure-outlet is present at the exit section: here the ambient pressure is imposed according to the conditions reported in Table 4.1. Fuel injection took place before the prefilmer lip with a dedicated inlet patch where its mass flow is derived accordingly to the global equivalence ratio. Concerning the walls of the combustion chamber, no-slip condition is used for the relative boundaries in all the simulations. Instead, the modeling of the thermal boundary condition on the lateral and bottom walls is a challenging aspect to be taken care of.

Firstly, no accurate information is available concerning the wall temperature from the experimental campaign. In this fashion, two different wall temperatures are used for respectively the FGM and the FGM-EXT models and the TF one, namely 700K and 1000K. This choice might appear counter intuitive since this study should assess the impact of the combustion modeling on the flame representation. However, by doing this, the magnitude of the heat losses through the walls is maximized in the FGM simulations but still with a reasonable value of temperature. Indeed, as it will be shown in the results section, this temperature well matches the experiments near the dome of the combustion chamber: assuming an even lower temperature might be unrealistic considering the test rig setup and operating conditions.

Keeping in mind this, the FGM-EXT approach should provide a good agreement with the flame or even the flame quench in the extreme case. In other words, this strategy should highlight the fact that the potential misprediction of the flame lift-off is due to an actual limit of the combustion model, rather than a low magnitude of the heat losses through the walls. This wall temperature was initially imposed also in the TF simulation (not reported here for the sake of brevity), resulting in the presence of unburnt fuel pockets at the outlet section, which is not possible considering this test rig. For this reason, the wall temperature was increased to the current value of 1000K, which is again a reasonable value considering the GT

application field [115, 117].
Although a well-defined sensitivity study to the wall temperature for the TF model has not been carried out, as it will be explained in the results section, this higher wall temperature already leads to a good agreement with the experiments in terms of fuel concentrations maps. In this sense, the use of a 700K as wall temperature would result in a worse prediction of the flame position. As well, another interesting point might be the scenario if a wall temperature equal to 1000K is applied also to the FGM and FGM-EXT approaches. At a first look, it is expected that the FGM-EXT will not revert to the FGM, since even if the heat loss magnitude is reduced, the correction effects might negligible only in absence of stretch actions, as visible in Figure 4.1. Further comments will be given in the dedicated results section.
The time step has been set to $1 \cdot 10^{-6}$ s, with a CFL value below 5 in the whole domain and below 0.5 in the flame region. The simulated physical time for each simulation is therefore reported in Table 4.2, where the Flow Through Time (FTT) is preliminarily estimated from the experimental measurements window and the average flow-velocity from the same measurements.

Table 4.2: Simulation average time with estimated FTT for each combustion model.

Combustion model	Average time	FTT
FGM	117 ms	8.75
FGM-EXT	150 ms	11.50
TF	180 ms	13.85

4.4 Results for the low-swirl gaseous lifted flame

Flow-field and local mixture composition

As explained in Chapter 2, this type of nozzle is characterized by a low swirl number which is responsible for a peculiar flow-field with

respect to the high-swirl injectors, commonly employed in current the GT's application. In Figure 4.7 the velocity field on the midplane up to 150 mm is reported for all the combustion models and experiments in terms of mean axial velocity maps.

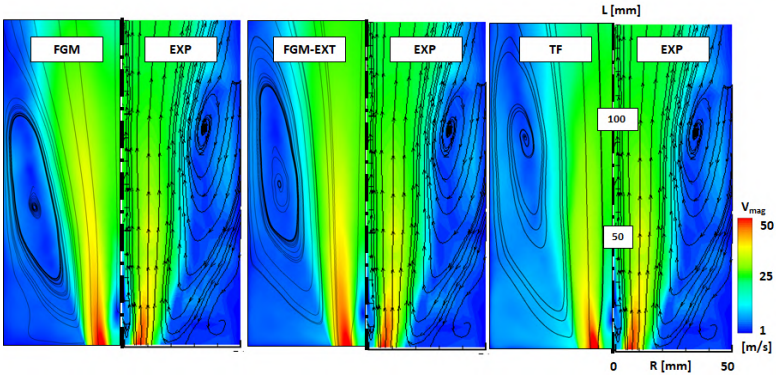

Figure 4.7: Contour maps of mean magnitude velocity with streamlines superimposed from FGM, FGM-EXT, and TF (from left to right) compared with experimental data from [65].

From a qualitative point of view, the results are in good agreement with the experimental data since all the key features can be observed, regardless of the specific combustion model. These involve the high-velocity streams close to the burner axis and rapidly decaying away from it in the radial direction, as well as the almost absent IRZ. Also, thanks to the streamlines the wide ORZ is visible besides the main jet, which extends from the burner dome into the combustion chamber.
Considering this last point, here the differences among the three combustion models are instead visible and they could be addressed to the different position of the predicted flame, hence the related thermal expansion of the flow.

A quantitative comparison is depicted in Figure 4.8 thanks to the radial profiles of axial velocity for given axial positions. Considering the nozzle near-field up to 10 mm, all the combustion models are collapsing

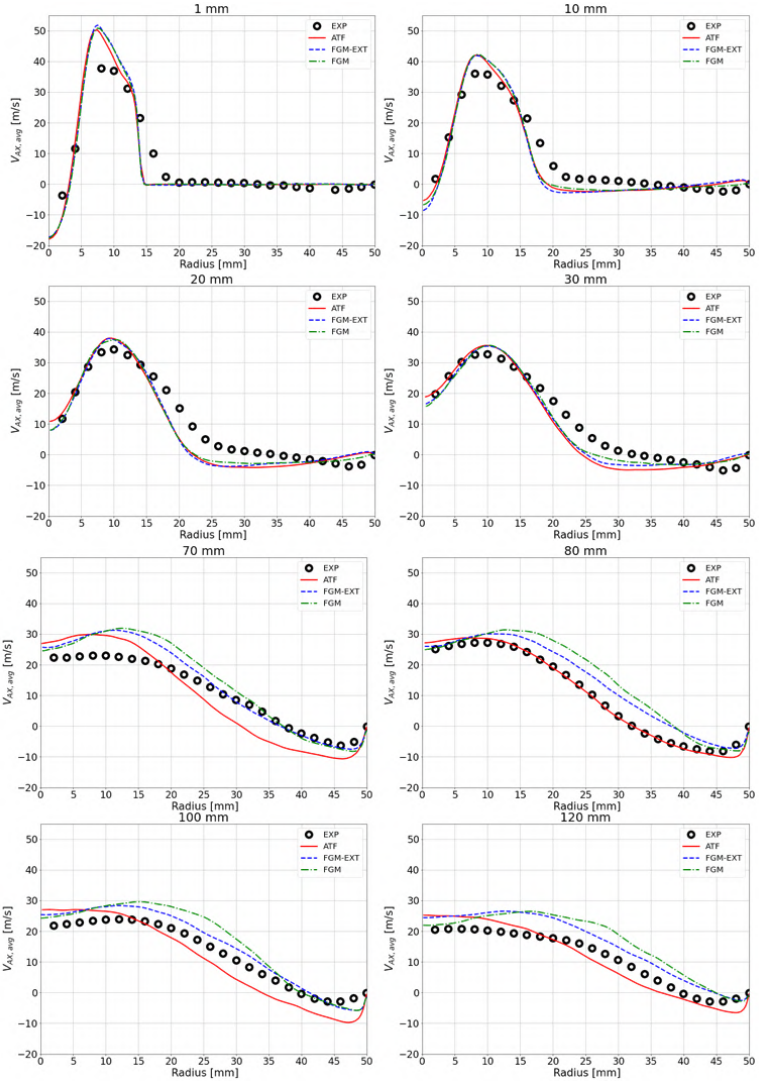

Figure 4.8: Radial profiles of axial velocity at given planes for the numerical simulations and experimental data.

on a single curve, since no influence on the flow due to the reaction zone is present yet. Here, the small IRZ is visible close to the nozzle axis, followed by a peak of velocity within 20 mm in the radial direction. Then, the axial velocity rapidly decreases, due to the presence of the ORZ. All the employed combustion models are in good agreement with the experimental data, except for the value of the peak velocity, which is overpredicted for the profile at 1 mm.
Also, the experiments show a larger spreading in the radial direction, while the numerical simulations are somehow reproducing a sort of narrower high-velocity stream, where the velocity decay more rapidly around 15 mm. A similar conclusion could be drawn also for the profile at 20 mm and 30 mm. Instead, from 70 mm the effects of the ongoing reaction is clearly visible and the combustion models begin to reproduce different trends along the radial direction. As expected, when the flame is predicted in a lower position, the heat release influence accelerates earlier the flow: the result is a higher value of velocity. This is the case of the FGM and the FGM-EXT approaches, which are always above the correspondent curve for the TF approach. Nevertheless, it is worth recalling that for the desired goal of this work the flow-field can be considered sufficiently described. Further improvements of the numerical model are instead left to future works.

The local composition of the mixture is reported in Figure 4.9 in terms of equivalence ratio ϕ contour maps. This quantity well describes another very important characteristic of the investigated nozzle: the mixing process between air and fuel along the LOH.
Since methane is injected only in the primary swirler, a fuel-rich composition is present close to the axis at the nozzle outlet section. As well, the pure air jets related to the secondary swirler are clearly visible at the bottom of the combustion chamber. These flow structures prevent the flame reattachment since they avoid the interaction of the vitiated products with the fresh mixture, thus delaying the ignition.
As for the velocity field, all the tested approaches are in good agreement with the experimental data from a qualitative point of view. Also, these

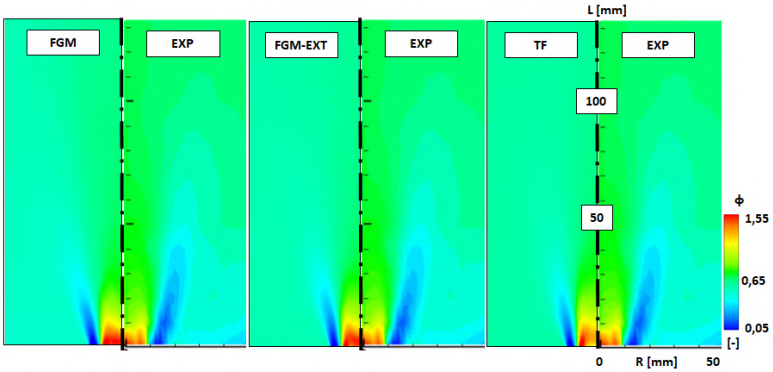

Figure 4.9: Contour maps of equivalence ratio up to 130mm from FGM, FGM-EXT, and TF (from left to right) simulations compared with experimental data from [64].

contour maps well explain the driving principle of this type of flame, where air and fuel enter as separate streams at the bottom of the flame tube, while mixing is completed within 50mm, obtaining the nominal value of $\phi = 0.65$. Meanwhile, it is clear here that the ORZ is dominated by vitiated air, that as explained is of paramount importance for the flame stabilization.

Chemical species

The comparison between numerical simulations and experimental measurements in terms of chemical species is one of the most interesting and critical aspects considering the goal of the present work.

Figures 4.10 and 4.11 reports the comparison in terms of methane mole fraction X_{CH_4} and carbon dioxide mole fraction X_{CO_2}. In contrast to the previous equivalence ratio maps, here the differences among the combustion models are clearly visible.

Considering the X_{CH_4} maps, the FGM model reached the complete oxidation of the fuel before 100mm in the axial direction, pointing out the over prediction of reactivity already seen in the previous works. This issue

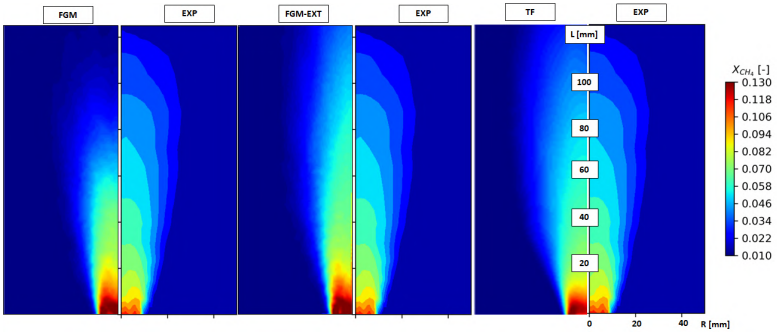

Figure 4.10: Contour maps of CH_4 mole fraction (X_{CH_4}) from FGM, FGM-EXT, and TF compared with experimental maps adapted from [65].

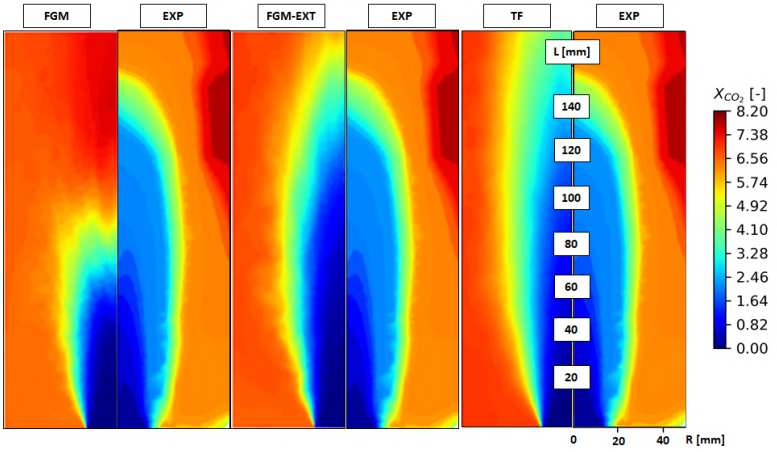

Figure 4.11: Contour maps of CO_2 mole fraction (X_{CO_2}) (left) from FGM, FGM-EXT, and TF compared with experimental maps adapted from [65].

is largely improved with the FGM-EXT approach, where the fuel oxidation is not completed in the reported 125 mm, as depicted in the experimental map. However, the levels of X_{CH_4} are lower than expected at the end of the maps, leading to a not perfect agreement with the measurements. The opposite situation is instead verified for the TF approach, where the levels of X_{CH_4} at 125 mm are slightly higher than the experimental counterpart.
Regarding the contour maps of carbon dioxide mole fraction $X_{CO_2}$the inner region of the swirling jet is dominated by low values, since here no reaction is occurring yet and the high velocity streams avoid the presence of recirculating combustion products. Again, the FGM model is reproducing a small penetration of the nozzle jet, rapidly approaching the values of X_{CO_2} corresponding to the equilibrium composition. The FGM-EXT and the TF models are instead comparable under this point of view. The concentration of CO_2 instead reaches high levels in the ORZ, due to the presence of the combustion products. Also, the experimental contours are reporting lower levels of X_{CO_2} at the bottom of the flame tube, that are not predicted in the numerical simulations: this aspect will be further investigated in future works.

Figure 4.12 reports the mean carbon monoxide mole fraction, X_{CO} which can be considered a good indicator of the ongoing reaction from a qualitative point of view. Each map refers to the maximum value observed on this plane for a specific combustion model: these are reported in the related table again in Figure 4.12. It can be seen that the TF simulation is underestimating the peak by two orders of magnitude with respect to the experimental finding, while both FGM models are instead overestimating this value but within almost the same order of magnitude. This fact could be explained by the previously mentioned misprediction related to the 2-step chemistry, which is reported also in [132]. Nevertheless, from a qualitative point of view, this comparison permits the visualization of the flame region in terms of extension and shape.
The lift-off occurrence is predicted by all the combustion models since each map is reporting the reaction zones detached from the nozzle outlet.

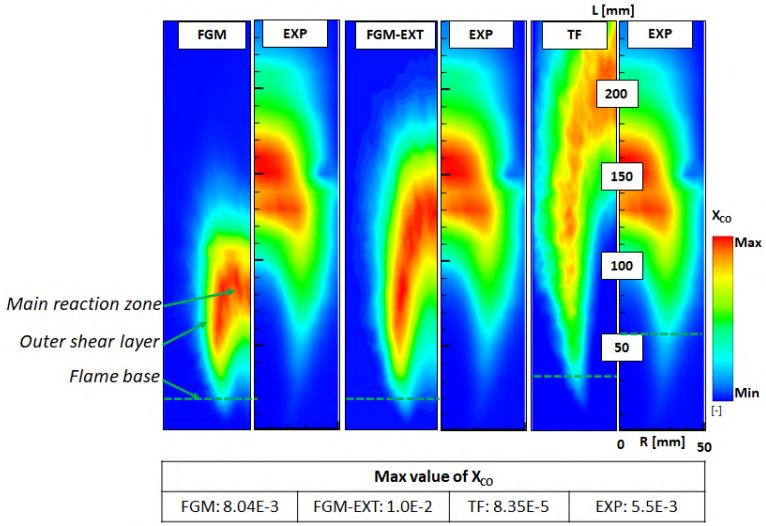

Max value of X_{CO}			
FGM: 8.04E-3	FGM-EXT: 1.0E-2	TF: 8.35E-5	EXP: 5.5E-3

Figure 4.12: Contour maps of averaged CO mole fraction (X_{CO}) respectively for (from left to right) FGM, FGM-EXT, TF combustion models, and experimental data from [65].

As found in [90], the FGM model reproduces a short and more compact flame than the experiments. The main reaction zone is found between 50 and 100 mm, while the flame base occurrence can be found around 25 mm. However, the flame assumes an arrow shape, where the anchoring edges are visible in the outer shear layer.

The FGM-EXT improves the flame prediction by taking into account the stretch and heat loss effects, even with the simplistic approach introduced in the combustion modeling section. Here the main reaction zone is placed between 100 and 150mm, getting closer to the experimental map. This is because the inner zone around the axis is now experiencing a lowered reactivity thanks to the intense stretch field related to the nozzle jet. Still, the LOH is underpredicted since the first occurrence of the reaction zone is almost identical to the standard FGM outcome.

Also, high values of X_{CO}, similar to the ones present in the main reaction

zone near the burner axis are found in the outer shear layer. A possible explanation for this is related to the stretch field presence, which assumes very low values in the ORZ and decays moving downstream in the flame tube, as it will be shown in the next section.
Differently with the TF model the main reaction zone stabilizes around 200 mm, which is even more downstream the experimental finding (i.e., 150 mm). The flame again assumes all the features already seen with the other models in terms of anchoring edges, arrow shape, and inner regions devoid of reactions, but all these zones have now a larger extension. Another important point to highlight is that now the reaction zone is reaching the lateral confinement walls, which is reported also by the experimental map, and potentially could enhance the heat losses contribution. This aspect was already introduced in Chapter 4 with the experimental findings by Sedlmaier in [70], where the impact of different cooling flow rates was tested.
Unexpectedly, the base of the flame is still placed in the lower zone of the combustion chamber and it is closer to the FGM models rather than the experiments. The latter indeed is anchored beyond 50mm while the TF model reactions occur before this position.

Temperature field

The comparison between numerical simulations and experiments is reported in terms of temperature field in Figure4.13. As mentioned in the numerical setup section, the FGM models and the TF are employing different values of wall temperature, since imposing 700K for the TF simulation results in the presence of unburnt fuel at the outlet, which is not the case considering the experimental findings. All the contour maps are showing a relatively cold region close to the nozzle axis in correspondence of the swirling jet, while a higher temperature is present in the ORZ dominated by the combustion products recirculation. The extension of this cold region depends on the combustion models, since it is strictly related to the position of the main reaction zone, as shown by the X_{CO} maps.

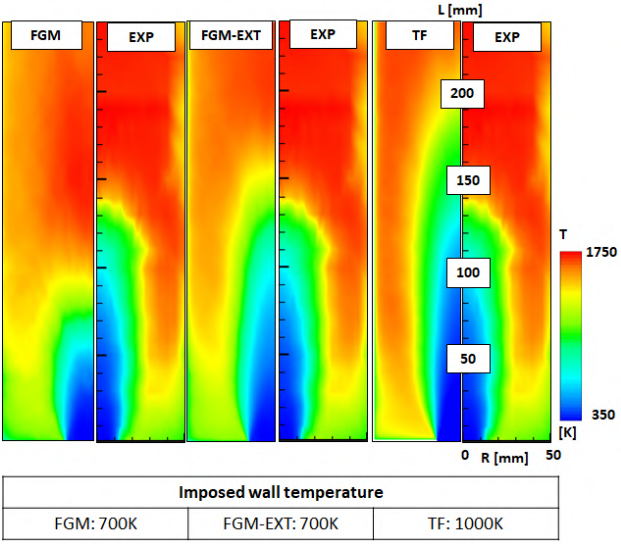

Figure 4.13: Contour maps of averaged temperature respectively for (from left to right) FGM, FGM-EXT, TF combustion models, and experimental data from [65].

Although the best prediction in terms of X_{CO} is related to the higher value of wall temperature, the temperature field in the FGM models reaches a better agreement with the experiments near the bottom of the flame tube. As well, the region with the highest temperature (close to the adiabatic flame one) according to the experimental map, seems better described in terms of position with the FGM-EXT model rather than the TF one.

Besides the value imposed on the walls, it is expected that a uniform wall temperature could lead to a wrong prediction of the flame temperature field. This means that likely the wall temperature set to 700K is reasonable for the first part of the combustion chamber, as shown in Figure 4.13, but then this value should be increased taking into account the heat transfer with the recirculating products, similar to the strategy reported by Massey et al. in [117]. This aspect is clearly of primary importance

and it will be investigated in detail in future works.
Another important consideration that can be drawn is that the misprediction associated with the FGM and the FGM-EXT approaches is not related to improper wall thermal boundary conditions, but an actual limit of this type of modeling. Indeed, the lower wall temperature should have enhanced the effect of $\Gamma_{\kappa,\Psi}$, thus predicting a reaction zone with the FGM-EXT closer to the experimental measurements with respect to the TF model.

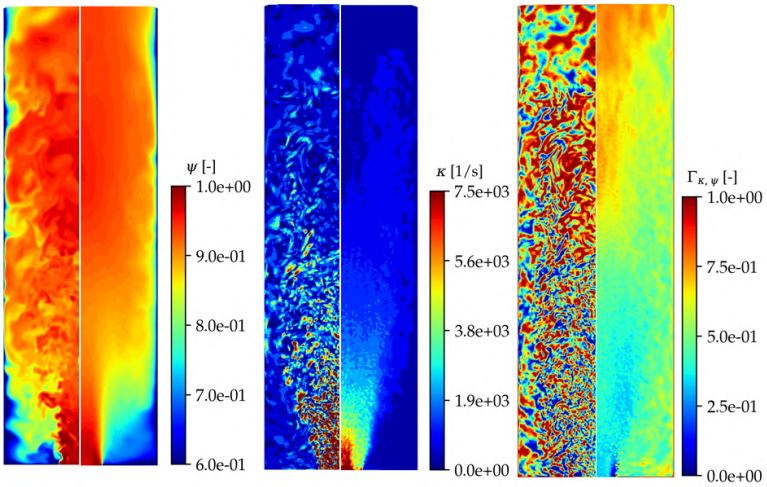

Figure 4.14: Contour maps of instantaneous and mean field for heat loss Ψ, stretch κ and correction factor $\Gamma_{\kappa,\Psi}$.

A better understanding of how the heat loss correction works in the FGM-EXT is possible thanks to Figure 4.14, where the instantaneous and mean fields of heat loss Ψ, stretch κ and correction factor $\Gamma_{\kappa,\Psi}$ are reported. As explained previously, $\Gamma_{\kappa,\Psi}$ affects directly the global reaction rate $\overline{\dot{\omega}}_c$ in the FGM-EXT: the regions distinguished by low values are the ones where the flame experiences a reactivity decrease and potentially the local quench. The value of $\Gamma_{\kappa,\Psi}$ depends on the local level of aerodynamic stretch and heat loss. The first reaches high values in the nozzle near field

and close to the burner axis. The heat losses instead are concentrated in the bottom corner of the combustion chamber and near the confinement walls. This means that the low temperature imposed at the walls for the FGM-EXT, enhances this quantity, as visible in Figure 4.14. For this reason, even if a relatively strong heat loss field is present in the corners, the low values assumed by the stretch field maintain the reduction factor at an intermediate level, which can be deduced also from Figure 4.1. Furthermore, the chaotic behaviour of the instantaneous field of $\Gamma_{\kappa,\Psi}$ is again related to the same field of κ, which is governed by the turbulent structures in the flow.

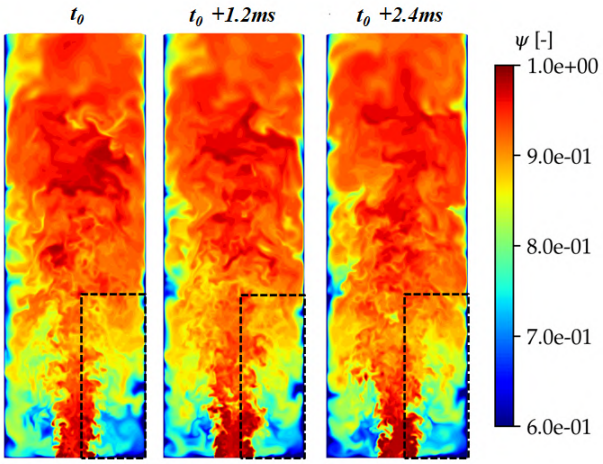

Figure 4.15: Instantaneous maps of heat loss field Ψ for various instants of time (from left to right). The blacks dashed lines highlight the recirculating gas cooling during the upstream transport.

Moreover, the importance of the wall heat losses could be deduced considering the sequence in Figure 4.15 reporting the instantaneous field of Ψ for various instants of time. It is worth recalling that for this simulation the wall temperature is imposed to 700K, which is less than half of the adiabatic flame temperature, therefore the heat loss will be strongly

enhanced at the walls. The hot combustion products are taken from the reaction zone upstream and transported by the ORZ upstream toward the bottom of the flame tube. During this transport, as highlighted with the black dashed lines in Figure 4.15 these gases are cooled down by the walls, thus delaying the ignition of the incoming fresh mixture.

4.5 Considerations on the stabilization mechanism

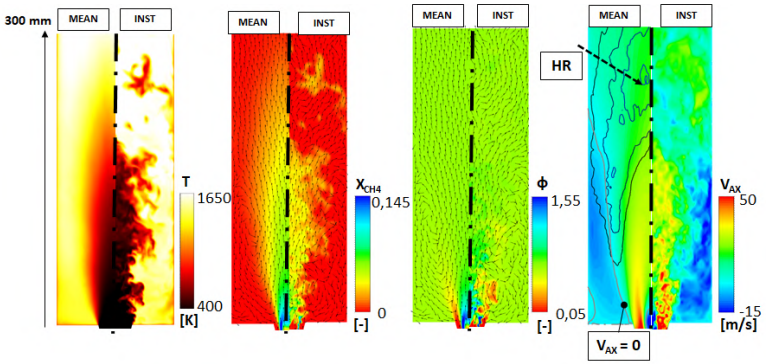

Figure 4.16: Contours of mean and instantaneous quantities from the TF simulation of (from left to right) temperature, methane mole fraction X_{CH_4}, equivalence ratio ϕ, and axial velocity with heat-release (HR) isolines superimposed. Normalized vectors of velocity are superimposed on the methane mole fraction and the equivalence ratio maps.

In Figure 4.16, the mean and instantaneous contours for the TF simulation are reported in terms of the temperature, methane mole fraction, equivalence ratio, and axial velocity field: in the latter contours isolines of heat-release and zero axial velocity are superimposed.
The flame stabilizes at a position where a sufficiently low value of the velocity is reached: this can be seen by both the decrease of methane concentration as well as the increase of mean temperature in the flame tube along the axial direction. The flame base is anchoring on the outer shear layer of the swirling jet, as visible from the zero axial velocity isoline

tangent to the heat-release ones.
Also, the temperature and equivalence ratio instantaneous fields show the presence of turbulent instabilities at the jet basis: this phenomenon leads to the entrainment of hot vitiated products in the fresh mixture jet, operating the continuous re-ignition of the reactants reported in previous works in literature [45]. The ORZ acts as a reservoir of hot combustion products, promoting the ignition mentioned before since here all the fuel is already consumed, but the composition shows values of ϕ close to the nominal value for this test point. All in all, the TF model can correctly predict the stabilization mechanism, as depicted also for the FGM and the FGM-EXT model in Chapter 3, but it is superior from the reaction zones prediction point of view.

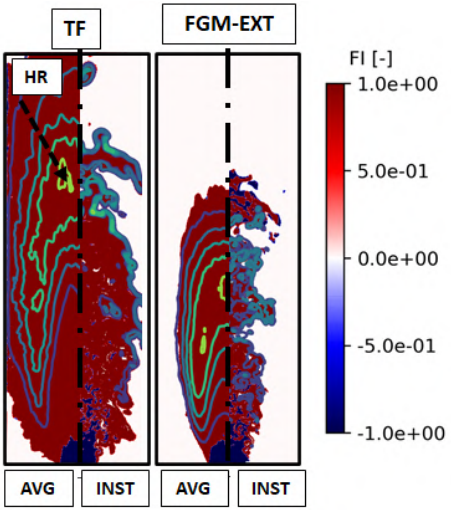

Figure 4.17: Contour maps of instantaneous and mean field of Flame Index FI for the TF (left) and the FGM-EXT (right) models.

Additionally, in Figure 4.17, the instantaneous and mean maps of Flame Index FI are reported for both the TF and the FGM-EXT models, with superimposed the isolevels of heat release. The Flame Index could

be interpreted as an indicator of where the flame can be assumed in a premixed state or a non-premixed one. This quantity is defined as [135]:

$$FI = \frac{\nabla Y_{Fuel} \cdot \nabla Y_{Ox}}{|\nabla Y_{Fuel} \cdot \nabla Y_{Ox}|} \tag{4.16}$$

where a value of equal to 1 indicates a premixed state of the reactive mixture and -1 a non-premixed one. In Figure 4.17 it can be seen that both approaches are dominated by the premixed-like conditions since such state is reached very early in the combustion chamber. This highlights also the capability of this low-swirl lifted flame to operate as a premixed flame without the use of premixing chambers.

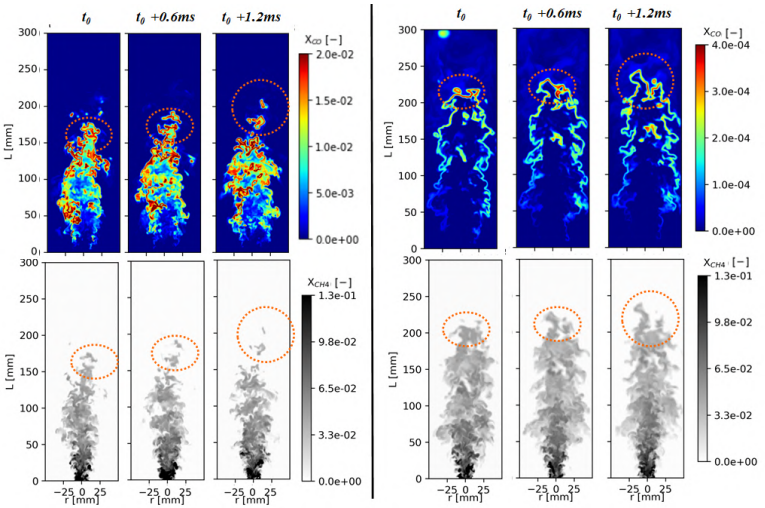

Figure 4.18: Sequence of instantaneous maps of X_{CH_4} and carbon monoxide mole fraction X_{CO} for the FGM-EXT (left) and the TF (right) models. Circles indicate the reactive regions being transported downstream.

Finally, instantaneous maps for X_{CH_4} and X_{CO} are reported in Figure 4.18. Three consecutive instants are reported, aiming to show the dynamic behaviour related to the reactive regions. The swirling jet enters the

flame tube with a rich local composition and it experiences the already mentioned flow instabilities interacting with the vitiated hot products and promoting the mixing downstream. The presence of carbon monoxide acts as an indication of the flame front position, showing how the fuel is being consumed. The TF simulation is showing a thin reaction front strongly deformed by the turbulence. Moreover, it can be seen how the flame front is interacting with the lateral walls, which indeed enhances the heat losses and therefore the decrease of the reactivity. The reaction front surrounds the reactive mixture regions (circled in Figure 4.18) with a sharp and well-defined front: from a modelling point of view, this behaviour is due to the dynamic thickening and here the flame sensor Ω drops to 0 within this region. Instead, the FGM-EXT field is reporting a compact reaction zone highly corrugated and this time the direct interaction with the walls is not occurring. The reactive mixture regions are showing a diffused reaction zone, where the higher values are present at the outer layer of this region. The flame front position is now related to the transport of the mean progress variable and its variance, where the assumption made on the turbulence-chemistry interaction plays a decisive role.

Concluding remarks on the FGM and TF simulations

The previous sections have shown the numerical LES modelling of the low-swirl partially premixed lifted flame operated with gaseous fuel with three different combustion models, namely the TF model, the FGM model, and finally a version of the FGM with stretch and heat loss correction. This analysis has pointed out that a crucial point is the influence of the heat losses on the final prediction, which has been demonstrated with both experimental and numerical results in previous studies. Since no information on the wall temperature is present, a uniform value has been imposed on the wall thermal boundary conditions: this value has been chosen considering the experimental results near the bottom of the combustion chamber, similar to previous studies in the literature. This represents a major limitation for the final evaluation of the effects of

heat loss on the flame. Even more limiting is the use of a different wall temperature between the FGM models and the TF one. Nevertheless, this action was necessary to prevent the presence of unburned fuel at the outlet in the TF simulations, which is unrealistic for this test case. In spite of this, some remarks are possible considering the numerical results. Firstly, all the models predict the flame lift-off, and all are very close to the experiments in terms of velocity field and local composition of the exhaust gas. The main differences are related to the position of the reaction zones in terms of CO mole fraction and obviously of the temperature field. The FGM models are under predicting the flame height and extension both in the axial and radial direction, despite the higher magnitude of the heat losses. The TF model instead is slightly over predicting the main reaction zone position even with the higher wall temperature. Noticeably, all the models are retrieving the early occurrence of reaction in the flame tube in the ORZ, which is not observed in the experiments. Also, the TF model is largely under predicting the CO concentration due to the use of 2-step mechanisms with respect to the FGM models employing a detailed one. The temperature field is affected by the choice of the different boundary conditions: a general conclusion is therefore not possible from the comparison among combustion models, except that the use of uniform wall temperature is not correct, also considering the flame extension in the combustion chamber. Moreover, the experimental findings concerning the stabilization mechanism seem correctly reproduced by all the models.
Another point to address is the fact that, although the best prediction is related to the TF model, limited information are available on the chemical species, due to the simplified chemistry approach.
Considering all these aspects, in the next section a hybrid TF-FGM approach is proposed and tested, with the aim of exploiting the advantages of both for the flame prediction.

4.6 Combustion modelling developments

The studies carried out so far have confirmed the findings pointed out in the literature, which attributed an over prediction of the reactivity level to the FGM approach. Additionally, a first attempt to introduce the stretch and heat loss modelling through the so called FGM-EXT approach shows that this is not enough to improve the flame representation.
The introduction of the TF modelling instead shows a very interesting result and opposite to the FGM one, but nevertheless not achieve a good representation of the flame. In this sense, a potential improvement of the combustion modelling to describe the flame in the correct way seems to include within the same model the inherent capability of the TF model to include the stretch and heat loss effects with the detailed chemistry description provided by the FGM approach.
To this aim, in this section an hybrid TF-FGM approach is proposed and compared with the experimental measurements. Nevertheless, the previous study has pointed out that the inclusion of the heat loss is of paramount importance for a correct description of the flame. Hence, a non-adiabatic manifold for the FGM approach is described and implemented in this novel strategy. Also, this attempt, together with the related results, has been carried out in [136].

Non Adiabatic Flamelet Generated Manifold

As pointed out many times, heat loss effects on the flame front are crucial for the flame prediction. In this regards, the FGM approach natively is not able to take into account of such effects.
Recalling the strategies pointed out in Section 4.1 for heat loss modelling within the tabulated chemistry framework, a possible way consists of introducing an additional dimension to the manifold for this purpose.
For this reason, here heat loss effects are taken intro account during the look-up table generation thanks to the use of non-adiabatic flamelets. Indeed, the usual adiabatic flamelets does not consider the effect of enthalpy on the reaction, and these effects are handled only in the calculation

by varying the temperature or gas properties. Instead the use of non-adiabatic flamelets takes into account of enthalpy loss or gain also during the generation of the table, therefore on the chemical species and related reaction rates. An example of the effect of enthalpy loss on the reaction rate is depicted in Figure 4.19 for given conditions. Also, similar strategy have proposed in the literature [137] in the years.
In this work, the strategy adopted in the CFD code ANSYS Fluent 2021R2 [138] is used. Both freely propagating premixed flamelets for low values of heat loss and burner stabilized flamelets at higher levels are employed. These latter type introduced enthalpy loss or gain by varying the burner temperature.
The switch from one type of flamelets to another is done automatically based on inlet composition and enthalpy inlet at boundaries. The final table is a five-dimension manifold, where only an additional input for the enthalpy loss, since it is convoluted in the table assuming a delta function. In this fashion, the overall cost-effective approach in terms of computational efforts is maintained. This new strategy has been validated for some well-known test cases in the literature [116], obtaining very interesting results. For the sake of clarity, the same nomenclature of [116] is used here, therefore the FGM model with non-adiabatic manifold is referred as NFGM in the next sections.
Aiming to compare the effects of this new tabulation with the previous results, the same settings of the table have been employed. Therefore, the GRI3.0 detailed mechanism is used for the table computation. The table is still discretized with $64x32$ points in terms of respectively z and c. Instead, 21 levels are employed for the enthalpy loss-gain discretization. Also, the Finite Rate closure is employed for the progress variable source term modeling.

Coupled TF-FGM model

The focus of this section is the application of the same artificial thickening used in the standard TF model [95] to the equation of the scalars from the FGM approach.

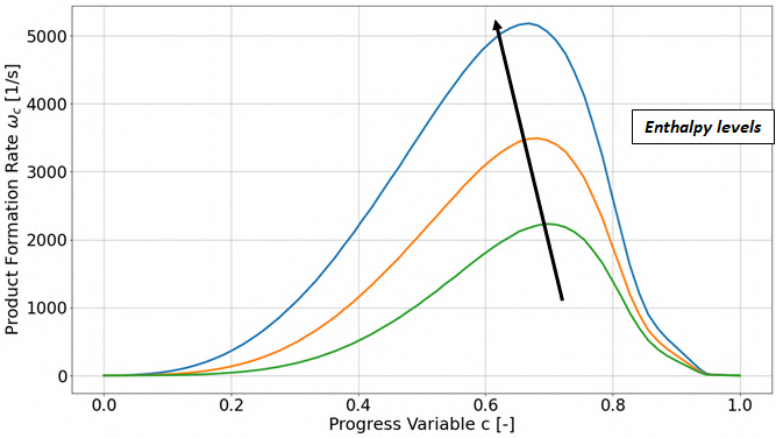

Figure 4.19: Product Formation Rate $\overline{\dot{\omega}}_c$ versus progress variable for various levels of enthalpy (operating conditions: $\phi = 1.0$, ambient pressure and inlet temperature).

The thickening procedure pointed out in Section 4.2 is therefore maintained in all these aspects, but now it is applied to the FGM scalars, c and z instead of the generic chemical species. In this fashion, the equations are recasted now as:

$$\frac{\partial \overline{\rho}\tilde{Y}_c}{\partial t} + \frac{\partial \overline{\rho}\tilde{u}_j\tilde{Y}_c}{\partial x_j} = \frac{\partial}{\partial x_j}\left(\overline{\rho}D_{eff}\frac{\partial \tilde{Y}_c}{\partial x_j}\right) + \frac{E}{F}\overline{\dot{\omega}}_c \tag{4.17}$$

being $\overline{\dot{\omega}}_{c,l}$ is the mean source term of progress variable provided by the PDF table, while the diffusivity is identical to the definition given in Section 4.2, that is $D_{eff} = D_l E(1 + (F-1)\Omega) + D_t(1-\Omega)$ (being D_l is the laminar diffusivity and D_t is the turbulent one).
Also, for the sake of brevity, the mixture fraction z and the enthalpy h equations are not reported, considering that the whole procedure is applied in the exact same way to terms in the respective equations.
An important point of the TF-FGM approach is that the variances for the involved scalars c and z are no more employed for the querying of the look-up table, since it is assumed that the TF formulation is able to take

into account properly the turbulence-chemistry interaction.
This approach has already been applied successfully in the literature to both gaseous [139, 140] and spray flames [137, 141]. The advantage of this approach is to include a better turbulence-chemistry interaction, avoiding the a priori β-PDF assumptions for c and z.
However, as explained in Section 4.2, the turbulent effects on the flame front are stictly related to the efficiency functions E, which clearly has to be properly computed. Within the present work, the defintion given by Colin et al. [95] is used, as already mentioned. In the followings some alternative strategies for the computation of E according to the Colin's definition are given, aiming to improve the physics representation.

Efficiency Function computation

As mentioned the efficiency function is introduced in the equations to recover the effects of the turbulence wrinkling altered during the front thickening procedure. This quantity is defined as the ratio of the flame wrinkling factors for the original flame and the thickened one. Here, E is computed following the formulation given in [95] by Colin et al.:

$$E = \frac{\Xi(\delta_l)}{\Xi(\delta_{TF})} = \frac{1 + \alpha\Gamma\left(\frac{\Delta_e}{\delta_l}, \frac{u'_{\Delta_e}}{s_l}\right)\frac{u'_{\Delta_e}}{s_l}}{1 + \alpha\Gamma\left(\frac{\Delta_e}{\delta_{TF}}, \frac{u'_{\Delta_e}}{s_l}\right)\frac{u'_{\Delta_e}}{s_l}} \tag{4.18}$$

where in turn:

$$\Gamma\left(\frac{\Delta_e}{\delta_l}, \frac{u'_{\Delta_e}}{s_l}\right) = 0.75 exp\left[-1.2/\left(\frac{u'_{\Delta_e}}{s_l}\right)^{0.3}\right]\left(\frac{\Delta_e}{\delta_l}\right)^{2/3} \tag{4.19}$$

and it stands for the dimensionless stretch of a flame with flame velocity s_l and thickness δ_l submitted to the action of a range of vortices [95]. For the sake of brevity, the other expression is not reported here, since it assumes the exact same form once the laminar flame thickness δ_l is replaced with artificially thickened one δ_{TF}.
Furthermore, another important aspect is how the velocity fluctuations

at the test filter u'_{Δ_e} are computed. A first attempt can be done considering the subgrid scale turbulent viscosity within the LES model. If the Smagorinsky model is employed for instance, u'_{Δ_e} can be derived as follows:

$$u'_{\Delta_e} = \frac{\nu_{sgs}}{C_L \Delta} \tag{4.20}$$

however, as reported in[95], this approach has two main drawbacks concerning the accuracy of the model constant C_L for the scales of interest, and the difficulties when dealing with the influence of thermal expansion. For this reason, in the same work, a similarity assumption has been retained as:

$$u'_{\Delta_e} = OP(\tilde{\mathbf{u}}) \approx \left| \left(\tilde{\mathbf{u}} - \hat{\tilde{\mathbf{u}}} \right) \right| \tag{4.21}$$

where $\tilde{\mathbf{u}}$ is the velocity field from the LES solution and $\hat{\tilde{\mathbf{u}}}$ is the filtered field at the scale Δ_e. This expression is futherly manipulated to avoid the use of a test filter, obtaining a final expression requiring a third-order derivative (the interested reader is addressed to the reference work [95]). This last fact could be not trivial when the implementation in a CFD solver is considered. An interesting approach to overcome this issue has been carried out is reported in the work by Durand et al.[142]. Here, the velocity fluctuations are derived from the formulation given originally by Colin [95]: here only the formulation valid for unstructured mesh is reported. Firstly, the scale similarity is written for finite volume approximation. An analog expression with the rotational operator is written as:

$$u'_{\Delta_e} = c\Delta_x \left| \nabla \times \left(\tilde{\mathbf{u}} - \hat{\tilde{\mathbf{u}}} \right) \right| = c\Delta_x \left| \nabla \times \tilde{\mathbf{u}} - \nabla \times \hat{\tilde{\mathbf{u}}} \right| \tag{4.22}$$

Then, the evaluation of the curl of the test filter is achieved by using its linear definition:

$$\hat{\tilde{\mathbf{u}}} = \frac{\sum_k \tilde{\mathbf{u}}_k V_k}{\sum_k V_k} \tag{4.23}$$

where $\tilde{\mathbf{u}}_k$ and V_k are respectively the velocity vector and volume of each cell surrounding the considered cell and evaluated within the main solver cell loop for each time-step.

In this work, both the definitions from eq. 4.20 and eq. 4.22 are employed to evaluate how the velocity fluctuations description impacts the final results: for the sake of clarity, the two different implementations will be referred as TF-FGM-A and TF-FGM-B respectively in the next sections.

4.7 Results with hybrid combustion models

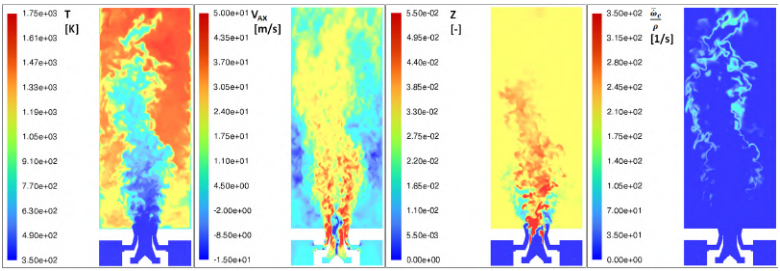

Figure 4.20: Instantaneous field of (from left to right): temperature, axial velocity, mixture fraction and progress variable source term over density for the TF-FGM-A model.

In this section, the numerical results are compared with the experimental data in terms of velocity field, local gas composition, chemical species and temperature field. Indeed, for the sake of brevity, the results in terms of CH_4 and CO_2 are not reported here, since these quantities are strictly related to the reaction zone position.
However, before this, a brief overview on the stabilization mechanism is reported in Fig.4.20, aiming to better explain how this flame works. Here, the instantaneous contour for the TF-FGM-A simulation are reported in terms of the temperature, axial velocity, mixture fraction, and progress variable source term over density. From the velocity field are

clearly visible the swirling jet and the related outer recirculation zone at larger radii. If compared with the temperature field, it is possible to notice the flow instabilities on the outer shear layer which entrains hot combustion products into the main jet, helping the stabilization at lean reactive mixture composition. This fact can be seen also if the mixture fraction field is considered, where z=0.055 corresponds to the stoichiometric mixture fraction. The outer recirculation zone is dominated by vitiated products, at nominal composition of the operating point. Instead, near the burner axis a fuel-rich composition is present initially, while it approaches the nominal value when moving downstream. Finally, the reaction occurs only away from the nozzle outlet and in that regions where a suitable low velocity is reached. This fact could point out a stabilization mechanism similar to the one originally described by Vanquickenborne and Van Tiggelen in [41] for a fully premixed lifted flame. However, a detailed description of the stabilization mechanism is out of scope and the interested reader is addressed to previous works[90, 113].

Flow-field and equivalence ratio

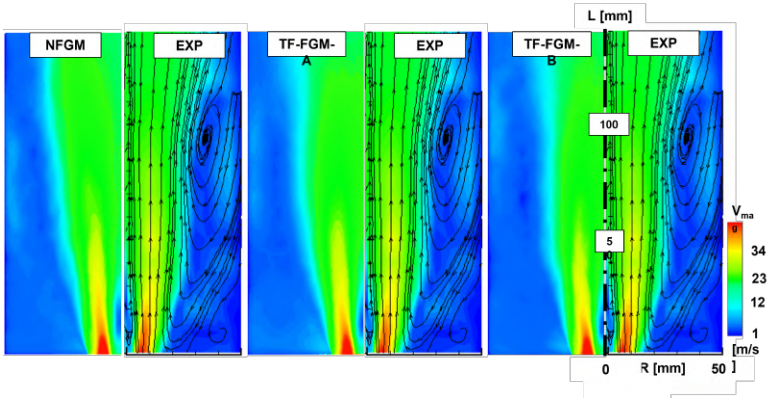

Figure 4.21: Mean velocity magnitude maps comparison. from left to right: NFGM, TF-FGM-A, TF-FGM-B, and EXP adapted from [64].

A preliminary comparison between numerics and experiments concerns the velocity and equivalence ratio fields. In Fig.4.21 the velocity field on the midplane up to 175 mm is reported for both CFD and experiments in terms of mean velocity magnitude maps. It can be observed that numerical simulations are in a good agreement with the experimental data since all the key features are present, regardless of the specific combustion model. That means the high-velocity streams close to the burner axis and rapidly decaying away from it in the radial direction, as well as the short and weak IRZ near the burner axis. Furthermore, also the stream height is around 50mm, as reported in the experimental map. A more quantitative comparison however should be performed to understand the discrepancies among the combustion models due to the different position of the predicted flame, hence the related thermal expansion of the flow.

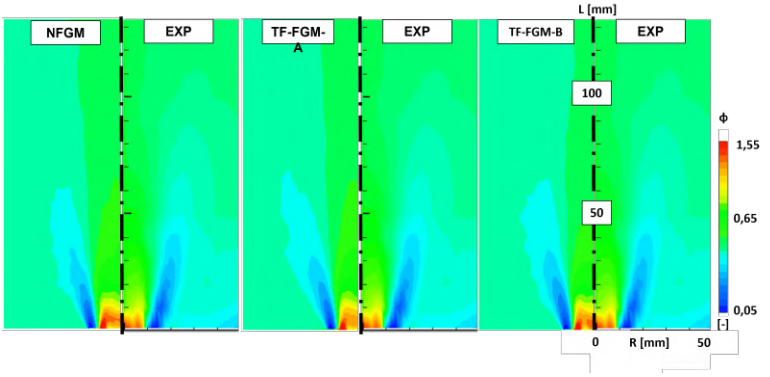

Figure 4.22: Mean equivalence ratio maps comparison. from left to right: NFGM, TF-FGM-A, TF-FGM-B, and exp adapted from [64].

The local composition of the mixture is reported in Fig.4.22 in terms of equivalence ratio ϕ contour maps.
Since methane is injected only in the primary swirler, a fuel-rich composition is present close to the nozzle axis at the nozzle outlet section, as already mentioned. Also the pure air jets related to secondary swirler are clearly visible at the bottom of the combustion chamber. The radial

channels are indeed responsible for a flow characterized by a very lean mixture and high axial velocity. Therefore, the flame reattachment is avoided, since these flow structures act as a barrier between the recirculating hot gas and the fresh mixture in the inner region. Also in this case, the investigated models are in a good agreement with the experimental data from a qualitative point of view. Some discrepancies are present instead considering the field near the bottom of the chamber, which seems with a leaner compositions in the experimental contour. This aspect will be further investigated in future works.

CO mole fraction

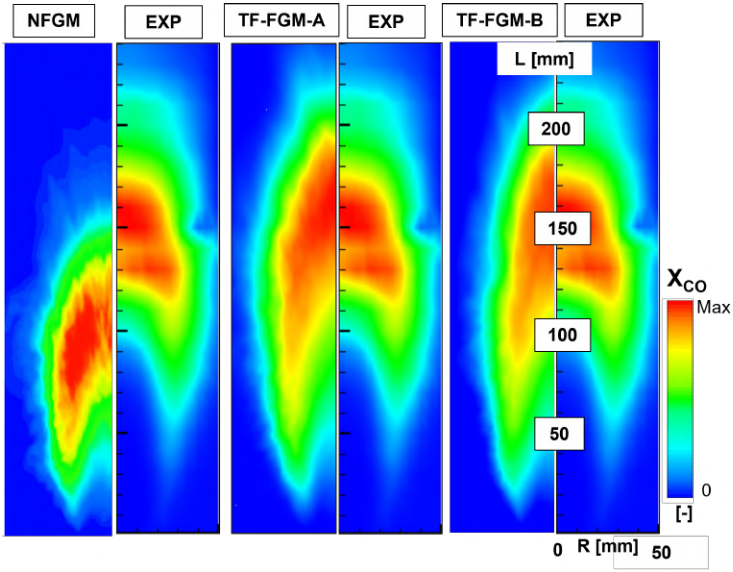

Figure 4.23: Mean CO mole fraction maps comparison. From left to right: NFGM, TF-FGM-A, TF-FGM-B, and exp adapted from [64].

Once again, the most important quantity among the chemical species is surely the carbon monoxide mole fraction X_{CO}, as best indicator

of the ongoing reaction from a qualitative point of view. It should be highlighted that the maximum value for X_{CO} is 0.055 for the experimental contours, while it is around 0.012 for the numerical results. However these are presented here in terms of normalized value, coherently with the numerical results in Section 4.4. Such difference could be related to the experimental measurement technique and will be object of future investigation.
In Figure 4.23 the contour maps of carbon monoxide mole fraction, X_{CO} are reported for the employed combustion models. As already noticed in the previous numerical results, each combustion model is predicting the flame lift-off, since all the maps are showing the reaction zones detached from the nozzle exit. This fact was already observed also with the standard FGM model with Adiabatic PDF, where the effects of heat losses were not taken into account. As well, each model is predicting the arrow-shaped flame according to the experimental findings with the base anchored on the outer shear layer of the main swirling jet.
When the NFGM model is used, the flame appears quite compact and short with respect to the experiments: the higher values of X_{CO} are found between 100 and 150 mm. Compared with the FGM with Adiabatic flamelets manifold studied in the previous Sect 4.4, it still could be seen an improvement, since the flame elevates more in the combustion chamber and with a wider reaction zone. The flame base instead is still anchored at the same height observed with the standard FGM model and generally high values of X_{CO} can be found in the shear layer between ORZ and the nozzle swirling jet.

It should be noticed also that although the manifold takes into account the effects of heat losses thanks to this novel manifold, this situation is verified mainly in the bottom corners of the combustion chamber, as can be seen in Fig.4.24. The heat loss is defined as $\Delta h = (h - h_{ad})/h_{ad}$ being h the mixture enthalpy and h_{ad} the adiabatic enthalpy for the given equivalence ratio[116]. The inner core and the mean reaction zone instead are not affected directly but, as observed in the experiments, it has an indirect effect due to the decrease of the recirculating gas temperature,

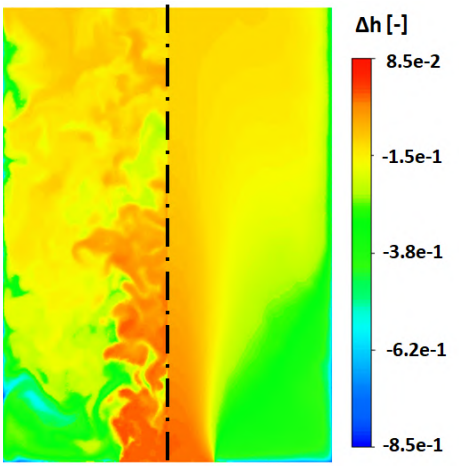

Figure 4.24: Heat loss contour maps up to 135 mm coming from the TF-FGM-A simulation. Left: instantaneous. Right: mean.

postponing the ignition of the mixture and thus decreasing the reactivity at the flame base.

Another useful consideration is that the NFGM approach seems to predict a worse flame shape with respect to the FGM-EXT of Section 4.4. This fact is somehow unexpected, since the FGM-EXT is quite simplistic as numerical modelling concerning a tabulated chemistry with an additional dimension. Nevertheless, it could point out that the inclusion of the stretch effects is not of secondary importance, which is a conclusion reported also in [90]. This aspect will be further investigated in future works. A good agreement in terms of flame shape and reproduction of the lift-off is instead reached considering the TF-FGM combustion model. The main reaction zone, where the highest value of the X_{CO} is reached is between 100 and 200 mm, which is shown also by the EXP map. Moreover, on the burner axis, CFD and EXP data are almost coincident where the most reactive region begins, which is around 110mm. Instead, the largest differences are still related to an early occurrence of the reaction zone in the lower part of the chamber. This concerns the outer shear layer of the

swirling jet, where the flame is anchored, which is showing a non-negligible presence of CO with respect to the EXP data.
Furthermore, the use of the most accurate computation of the velocity fluctuation with the TF-FGM-B model predicts better the post-flame region, which appear very close to the experimental data, while the TF-FGM-A model instead presents a larger extension of this region. Nevertheless, such results are showing a strong improvement with respect of the results obtained with other approaches such as pure TF model with 2step mechanism, where the flame largely exceed the flame position reported in the experimental map.

Temperature field

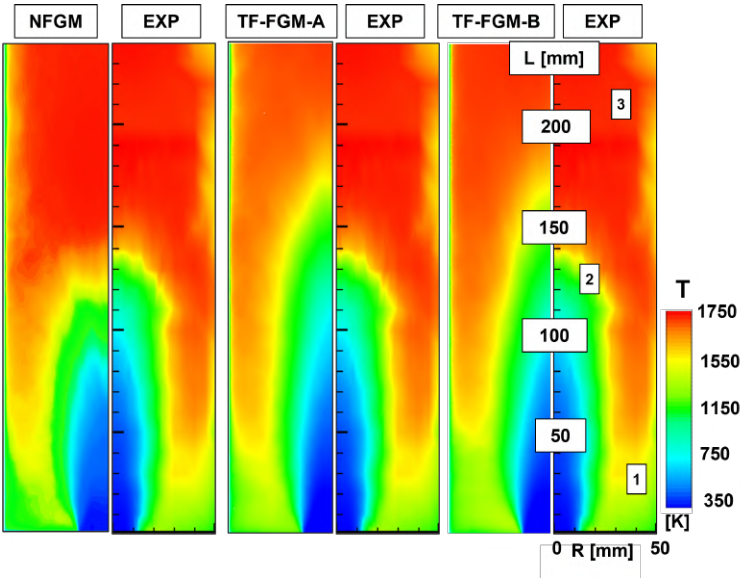

Figure 4.25: Mean temperature field maps comparison. From left to right: NFGM, TF-FGM-A, TF-FGM-B, and exp adapted from [64].

In Figure 4.25 the temperature field maps are reported again for all the

combustion models and compared with the experimental results. Here, the lift-off distance is visible thanks to the cold region which is present near the burner's axis, in correspondence of the swirling jet. Instead, the ORZ is dominated by the combustion products, being transported here from the flame region. The effects of the different combustion models indeed affect the extension of this cold jet, accordingly with the position of the main reaction zone in the flame tube, as shown in the CO mole fraction maps. However, the temperature field is affected by the assumption made for the thermal boundary condition on the wall, that is a uniform temperature equal to 700K.

Such assumption has been made after the results carried out from the previous works [113**?**], since the temperature seems fairly well predicted if the bottom corners of the chamber are considered. Also, the flame root (label "1" in Figure 4.25) is established near 50 mm in the axial direction, which is very close to the experimental measurement. This means that this assumption could reasonably be representative of the actual wall temperature near the bottom wall. However, assuming this thermal boundary condition also on the lateral confinement wall is leading to a wrong prediction of the temperature field downstream the main reaction zone (label "3" in Figure 4.25). This is clear if the NFGM map is considered: although this model has the worst agreement with the CO experimental finding, it also has the best agreement concerning the temperature field. Due to the early occurrence of the reaction zone, the post flame region temperature field is better described with respect to both the TF-FGM models. At the same time, this fact could also explain why the TF-FGM model is predicting a higher level of CO with respect to the experimental measurements, since the finite rate chemistry is slowed down due to the imposed lower temperature.

Considering label "2" in Figure 4.25, the spread of the flame front is highlighted in outer shear layer of the swirling jet. This region assumes an intermediate temperature between the fresh mixture and the fully oxidized reaction products. Both TF-FGM-A and TF-FGM-B are quite in agreement with the experimental finding. Here, the TF-FGM-B is

expected to have a better agreement, since the more accurate computation of the velocity fluctuations, thus the flame brush in this zone. Nevertheless, this results should be evaluated with a longer averaging for the TF-FGM-B. As well, the prediction of the cold jet penetration is very well predicted reaching the 100 mm of height similarly to the EXP map for both the models with the flame thickening.

4.8 Concluding remarks on the Single Sector Gaseous Flame

In this chapter an extensive numerical campaign was performed on the low-swirl gaseous lifted flame studied by Fokaides et al., where sequential improvements to the combustion modelling strategy are introduced continuously.
This sectin has confirmed again that the standard FGM approach is not able to correctly predict the flame LOH magnitude, although the use of a look-up table generated from Non-Adiabatic flamelets brings some slight improvements with respect of the previous works. Instead, the introduction of the coupled TF-FGM model results in a better prediction of the flame shape and lift-off, especially considering the main reaction zone position. Further improvements can be obtained depending how the velocity fluctuations at the test filter in the calculation of the the Efficiency Function are computed. Here, the use of an more accurate formulation leads to a better shape with respect of the computation from the subgrid model employed in the LES simulations.
In agreement with previous studies, further improvement are expected if a more representative boundary condition for the wall temperature is employed. As well, another interesting point could be the influence of a more accurate formulation of the Efficiency Function for the turbulence effects, such as the one carried out by Charlette et al. [143].
Finally, the manifold here employed takes into account only for the heat loss, but indeed also the action of the stretch on the flame front could be relevant and its inclusion in the manifold should be investigated.

Chapter 5

Reactive conditions simulations with liquid fuel

Although in the previous chapters the focus was on reactive cases employing gaseous fuel, the final step remains the application to spray flames. Here, as already introduced in Chapter 3 for the Multiburner simulations, further complexities are introduced due to the presence of the liquid fuel.

In Chapter 3, aiming to carry out a detailed but affordable numerical setup for the tilt angle sensitivity, some approximations were introduced in terms of spray boundary conditions modelling, other than turbulence and combustion description. Here, apart from the use of the hybrid TF-FGM model with Non-Adiabatic manifold carried out in Chapter 4, ad hoc boundary conditions will be employed for the spray. This has been possible thanks to a novel approach for the prediction of the atomization process at an early stage [36, 144], recently proposed and studied at the COmplexe de Recherche Interprofessionnel en Aérothermochimie (CORIA) from the University of Rouen.

It is worth notice also that this represents the first attempt to model this low-swirl lifted flame through CFD simulations, as far as the author is aware.

5.1 Modelling challenges for multi-phase flows

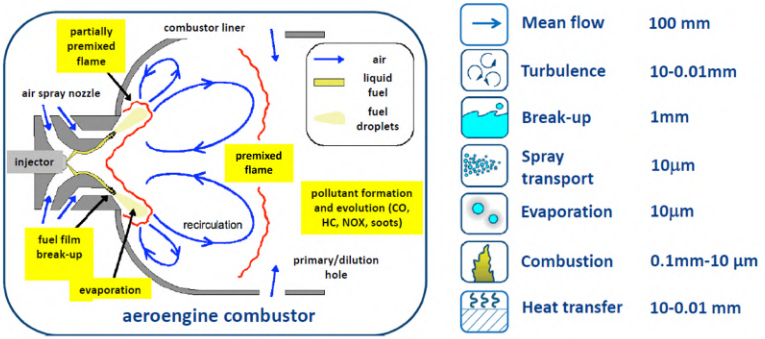

Figure 5.1: Conceptual sketch of the physics scales involved in a spray flame (adapted from [27]).

While LES turbulence framework has been already introduced with the isothermal calculations reported in Chapter 2 and the turbulent combustion has been widely discussed in Chapter 3 and 4, the spray modelling requires some further comments.

As depicted in Figure 5.1, generally speaking, the numerical reproduction of the physics occurring in a combustion chamber involves several different scales, which clearly are impacting the modelling choices themselves. Indeed, concerning the liquid fuel, the physical scales of the problem are strongly related to the injector type [28]. For instance, in Figure 5.1, the nozzle employs both a pressure atomizer (*injector* in Figure 5.1) and a prefilmer air-blast atomizer (*air spray nozzle* in Figure 5.1): these systems per se produce sprays characterized by very different liquid structures [30]. Furthermore, their performances could be impacted by the operating conditions, depending on the specific injector.

Apart from this, focusing on the only prefilmer air-blast atomizer, the liquid film formed on the surface undergoes the aerodynamic actions of the co-flowing air, being deformed and fragmented in ligaments and irregular droplets [28], according to the so-called *Primary Breakup* in the literature.

When moving further downstream, the larger ligaments are atomized into smaller spherical droplets (*Secondary Breakup*) and finally evaporate.
Although the simplified description, this sketch allows to understand that the complete simulation from the formation of the liquid film on the prefilmer surface to the ultimate droplet evaporation will be really challenging due to the fine spatial discretization required.
Keeping in mind this, it should be clear now that the need for an advanced multi-phase modelling is of primary importance, intended as an approach capable to describe with enough accuracy the atomization processes without impacting too much on the computational cost.
In this regard, the development of a numerical approach combining the liquid interface and sub-grid description of two phase flows and Williams-Boltzmann Equation resolution based on Lagrangian droplet tracking was mandatory to model the lifted spray flames resolving all steps including injection, atomization and spray propagation up to the combustion zone.
Generally speaking, the numerical simulation of liquid-gas flow with Interface Capturing Method (ICM) has been the topic of intense research during the last decade, leading to mature methods as Volume-of-Fluid (VOF) [145], Level-Set (LS) [146] and Front tracking methods [147]. As well, a number of combinations of the previous methods have been also proposed. Despite their accuracy, these methods require a complete spatial resolution of the flow thus implying a very high computational effort, thus the complete simulation of liquid fuel injection in the engine is not affordable. Others state-of-the-art numerical methods including Adaptive Mesh Refinement (AMR) [148] and Smoothed Particle Hydrodynamics (SPH) [149] on the most powerful computer still present some challenges when dealing with the multiscale nature of the problem, that range from sub-micron droplets up to combustor scale thus covering more than four orders of magnitude.
Indeed, this problem is addressed in only very few studies [148, 150] where an ICM approach is combined with a representation of liquid droplets below a certain size by Lagrangian particles interacting with the gaseous career phase through point source forces using the DPM Method, as in

Chapter 3.
These recent approaches suffer of many drawbacks related to the coupling between ICM and DPM that has not been achieved up to now in a fully consistent manner. But the most important issue is the necessity to capture the liquid droplet with the ICM approach until the spherical liquid droplets are produced to recover the relevant condition to apply DPM, thus not consistently solving the multiscale nature of the flow.
An alternative general approach is the so-called ELSA (Eulerian Lagrangian Spray Atomisation) [151]. This approach handles the unresolved interface by pinning down the liquid volume fraction and surface density (amount of surface per unit of volume) and has been successfully validated against DNS and experiments [152]. Recently extended to LES [152], this approach looks at the multiscale issue from another perspective: the unresolved interface. The last developments have seen the compatibility with ICM approach achieved thanks to Interface Resolution Quality (IRQ) sensors that allow to switch from ICM to under resolved interface [144, 153].
In this work, the latter procedure is applied in order to provide the advanced boundary conditions required by this type of injector: the developments of such boundaries have been carried out by the research team of the CORIA laboratories and a detailed description is available in [154, 155].

Test case and spray boundary conditions

The test case investigated here is the same already described in Chapter 2 and 3 concerning the operating conditions (i.e., $p = 4$ bar, $T_{in} = 573$ K, $\lambda = 1.91$, $dp/p_0 = 3$ %) with the relevant difference that the fuel is now JET-A1. The same numerical setup in terms of turbulence modelling, time step and numerical domain are therefore kept. Instead the local refinement within the mesh grid has been revised, extending up to 180 mm in order to include the whole reaction zone, according to the study in Appendix B: the final grid consists of 10 M of polyhedral elements.
Furthermore, making use of the experience from Chapter 4, the thermal

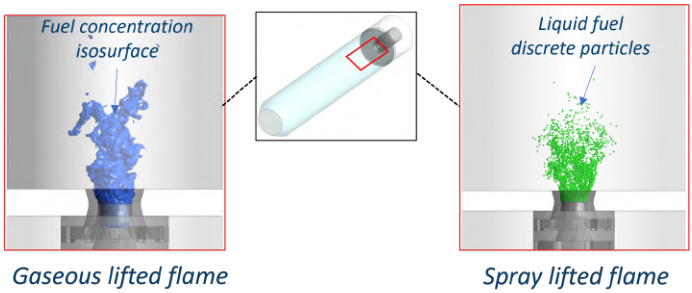

Figure 5.2: Comparison between gaseous and liquid injection in the considered test case.

boundary conditions to the walls is now adopting a linear increase in the first 50 mm, then assuming a uniform value, as shown in Figure 5.3.

The rationale behind this choice is to avoid the use of an adiabatic wall, while imposing a reasonable value of temperature considering the operating conditions here employed. Indeed, this strategy concerning the linear increase of temperature is already present in the literature [117]. Also, the axial position for the end of the linear increase, that is 50 mm, has been chosen since here is the estimated position of the flame base [68] (see Figure 5.4). Finally, it should be recalled here that the heat losses could not only affect the combustion process directly, but also the evaporation rate of the spray.

As in Chapter 4, these assumptions should be verified with a dedicated study, and future works will surely investigate in this direction.

Regardless of these modifications to the original setup, the main difference from the previous reactive simulation is without any doubt the presence of liquid fuel, which has to be properly modeled: as done for the multiburner in Chapter 3, the DPM method is employed for its description. This means to model the liquid phase with an Eulerian-Lagrangian approach, where the liquid is considered as a discrete phase carried by the gas one. This assumption could be considered adequate since the reaction zone is sufficiently far from the prefilmer, therefore the liquid phase has reached

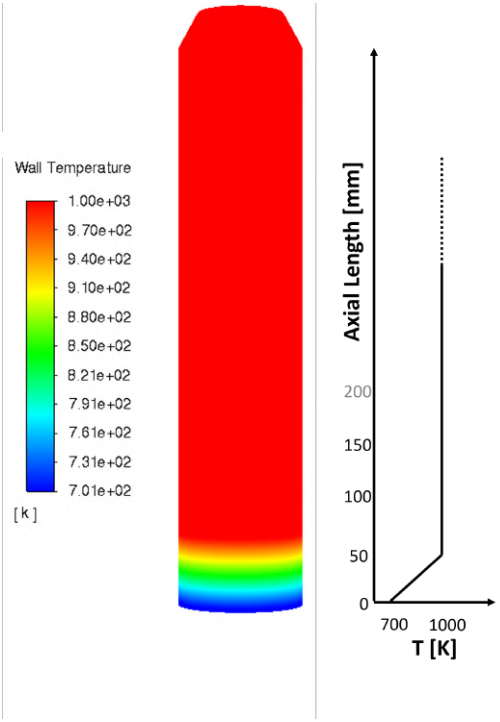

Figure 5.3: Thermal wall boundary conditions imposed in the numerical simulation along the axial coordinate.

the diluted regime (liquid volume fraction $\alpha_l \leq 1\%$).

Recalling the previously introduced challenges concerning the atomization process modelling for an air blast atomizer, the goal is to properly reproduce the initial distribution of droplets population in terms of diameters and droplet velocity. All the very interesting considerations concerning how the droplets population is recasted in terms of a well-defined representative distribution is out of scope in the present work and it is left to the dedicated literature [28, 30, 156].

It is clear that a poor description of the whole process would largely affect the flame itself since the reactive mixture field might be very far from

the real one. At the same time, a very detailed description of the liquid phase would require a complex numerical model, hence increasing the computational efforts needed for the simulation. One of the most common approach in the literature is to impose the spray injection with a Rosin-Rammler distribution where the distribution parameters are derived from an empirical correlation developed for this type of injector and available in the literature following the same approach of Chapter 5.
However, this strategy has two main drawbacks: the distribution is somehow fixed a priori, given the input parameters in terms of SMD and q; this distribution concerns the droplets population in terms of diameter classes, but clearly no information are retrieved on other characteristics, such as the spray cone angle and the initial velocity of the droplets. Normally, such quantities are assumed constant and uniform for all the droplets, by imposing a fixed value from correlations.

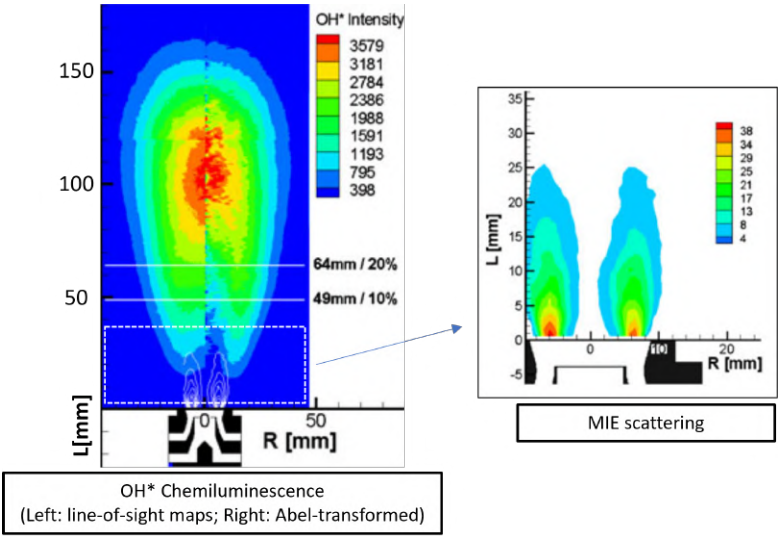

Figure 5.4: Flame OH chemiluminescence map (left) and MIE scattering light emission maps (right) for the investigated operating conditions (adapted from [68].)*

Another challenging point is the scarce information concerning the spray initial conditions from the previous experimental campaigns. Few data are available from the experimental campaign about the liquid fuel presence in the combustion chamber: qualitative information is obtained thanks to MIE scattering contour maps [40, 68], which allows visualizing from where the fuel is completely evaporated, as reported in Figure 5.4. Within the context of the numerical simulation, this quantity is compared with the normalized liquid volume fraction field: although the qualitative nature of this comparison, useful information can be drawn for the evaporation process.
Taking into account all these aspects and aiming to improve the spray boundary conditions, an hoc simulation of the prefilmer lip have been carried out by Ferrando et al. in [154], other than a procedure to couple the spray information in the present reactive simulation in [155].
In these studies, a LES-VOF approach is used to reproduce the liquid fraction field close to the prefilmer lip, where the Primary Breakup is expected to be accomplished. These simulations employ a novel strategy for retrieving information on the spray distribution based on the distribution of the curvature from the liquid structures [156, 157]. As shown in Figure 5.5, such structures are extremely irregular and need a dedicated procedure to be post-processed for the final spray estimation. The information on the corresponding droplets distribution is obtained through the fluxes of the liquid volume fraction α_l and the gas-liquid interface Σ_l at a given sampling position: for the sake of brevity the complete strategy is not reported here and the interested reader is referred to [144, 154].

The final diameter distribution is depicted in Figure 5.6: it should be noticed that the SMD computed with this procedure is around 40 μm (*D32* in Figure 5.6), which is close to the value obtained with the reference correlation by Gepperth et al. [158], employed also in Chapter 3 for the multiburner simulations. However, the maximum diameter here is 90 μm, while it is estimated around 240 μm for the equivalent Rosin-Rammler distribution. Moreover, in the same work, information about the velocity distribution for the droplets is obtained. Together with the diameter

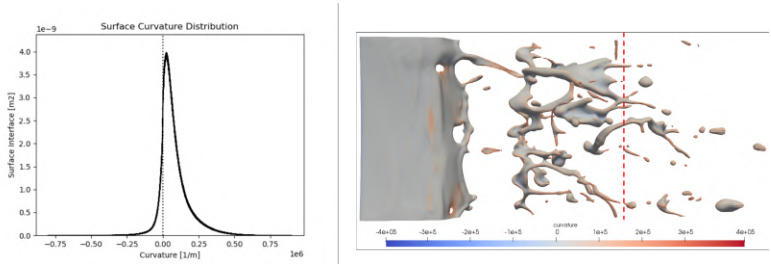

Figure 5.5: Surface Curvature Distribution (Left) and α_l contours (right) (adapted from [154].

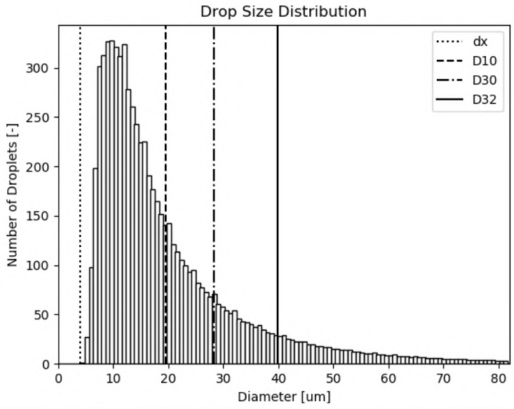

Figure 5.6: Drop Size Distribution for the investigated test point (adapted from [154]).

distribution, these information are used to set the boundary conditions, as reported in [155].

In the reactive simulations in the present work, the droplets are finally injected as lagrangian particles 1.2 mm downstream of the atomizer edge, being transported by the flow structures developed on the prefilmer surface. Since any information about the liquid fuel temperature is available, the temperature of the particle is set to 350 K. These values are considered

appropriate since this test point employed preheated air: it is reasonable to expect an increase of the fuel temperature especially at the location designed for the injection point after the liquid film primary breakup. Meanwhile, higher temperature are not expected to be realistic since they will lead to fuel cooking at the injector lip. Nevertheless, the fuel initial temperature remains an open point to be improved for future works.
As concluding remark for the spray boundary conditions, it should be said that in this first attempt, the TAB model for the Secondary Breakup is kept, as for the simulations on the multiburner. However, the impact of this model in the LES context should be further assessed before drawing some final conclusions.
Concerning the combustion modeling, this simulation exploits the outcomes of the previous tests with gaseous fuel. In this fashion a hybrid TF-FGM approach is employed together with a PDF table from non-adiabatic flamelets. The chemistry mechanism is again the Luche, as in Chapter 3. In particular, in this first attempt, the TF-FGM model exploits the definition of the velocity fluctuations at the test filter derived from the turbulent viscosity (i.e., the TF-FGM-A model of Section 4.6).

5.2 Numerical results

The main outcome concerning the numerical results for this test case is the comparison between experimental data and the TF-FGM-A approach previously mentioned. This comparison is reported in Figure 5.7: on left side the EXP map is reported in terms of OH* chemiluminescence map, while the CFD results are reported in the right side in terms of Product Formation Rate PFR (introduced in Chapter 3, source term of the progress variable $\dot{\omega}_c$ divided by the density) and mass fraction of OH* and CH*. These latter chemical species have been introduced in the Luche's mechanism thanks to the sub-mechanism reported in [159, 160]. The idea is to overcome the possible discrepancy between excited radical light emission and heat release signal, as discussed in detail by Lauer et al. in the literature [161]. It should be noticed also that each maps reports

on the left side the line-of-sight integrated map and the mean values on the midplane on the right side.
From this it is clear that, despite the interesting results obtained with the gaseous flame, the agreement between CFD and experiments is not satisfactory for the spray flame.

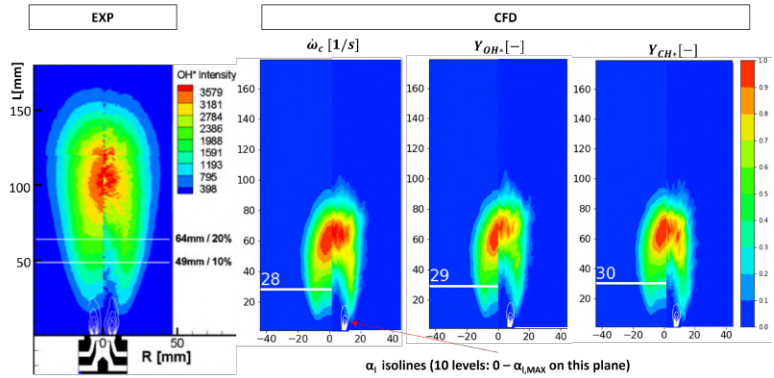

Figure 5.7: Mean contours of PFR, Y_{OH*} and Y_{CH*} in the nozzle near field with liquid volume fraction α_l isolines superimposed for the TF-FGM simulation. Exp maps is reported on the left side of the Figure.

This fact is clearly visible concerning the underestimation of the LOH in the CFD results, where a value of around 30mm is obtained against the experimental results of 49mm. The flame arrow-like shape is actually reproduced, but the extension of the reaction zone is not correctly reproduced leading to a shorter flame in the numerical results.
Additionally, it can be seen how the use of OH* and CH* mass fraction in place of the PFR leads indeed to a very slight shift downstream of the main reaction zone position. This effect clearly is not enough to justify the underestimation of the LOH, but nevertheless shows how it should be taken into account for the next calculations.
As final comment, it could be said that the TF-FGM approach is still not able to properly catch the flame shape, but still it introduces some advantages with respect to the standard FGM approach. However, for this case

unlike the gaseous flame tests presented in Chapter 4,a comparison among different modelling approaches is available only in terms of instantaneous contours maps due to the high computational cost related to the presence of the liquid phase within reactive LES calculation. Also, it should be recalled that, as explained in Chapter 2, the low-swirl lifted flame object of this investigation is characterized by a low frequency precession, which impacts the overall physical time to be considered in the simulation for well-converged statistics.
Keeping in mind this, some comments are still possible with these results from a qualitative point of view.

In Figure 5.8, the comparison between the standard FGM and the TF-FGM approach is reported. It is worth highlight that both are employing the same Non-Adiabatic manifold: however, in order to maintain a coherent description with the investigations carried out in Chapter 4, the FGM approach is referred as NFGM also in this case. The NFGM simulation is employed to initialize the calculation with the artificial thickening of the flame front.
This figure reports instantaneous maps of progress variable c, Product Formation Rate PFR, and mixture fraction z, from the nozzle outlet up to 180 mm. As first, it can be seen the improvement of the flame representation due to the use of the TF-FGM model is clear. Indeed, the NFGM model is barely predicting the lift-off occurrence, as visible from both the c and $\dot{\omega}_c$ maps.
The PFR maps have been clipped to a reference value of 350 1/s to highlight the main reaction structures: this is extending up to 100 mm for this specific instant of time for the TF-FGM approach. However, the flame position is almost defined, since no reactive zones have been observed beyond the 110 mm during the simulations by the author for various instants of time (not reported here). This fact points out that, if the experimental map in Figure 5.4 is considered as reference, the reaction zone, once retrieved a proper mean field, is stabilizing too low in the simulations.
Also, it should be said that the simulation time is long enough to affirm

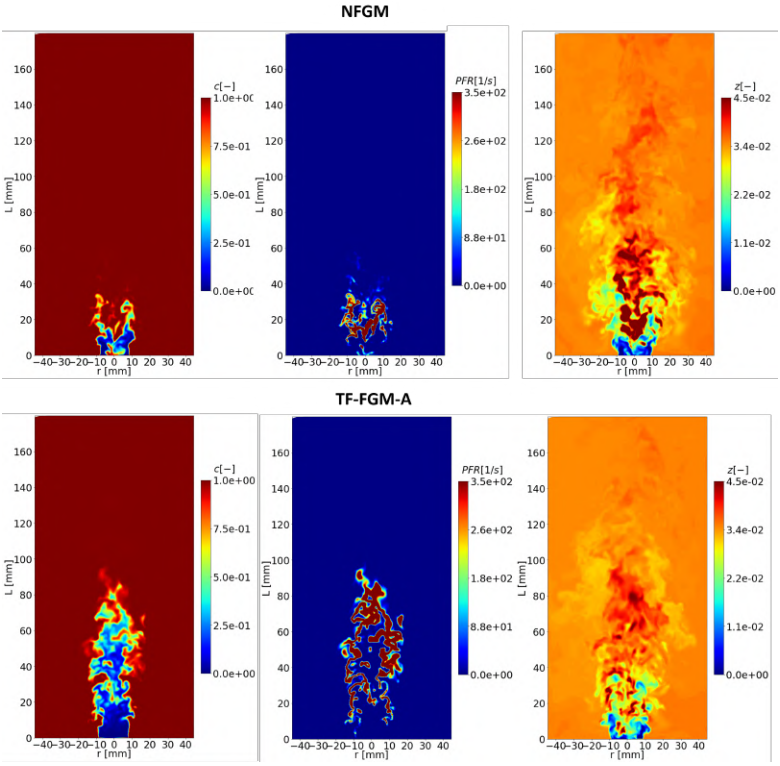

Figure 5.8: Instantaneous contour maps of (from left to right) progress variable c, Product Formation Rate PFR, and mixture fraction z, for the NFGM (top) and the TF-FGM with Non-adiabatic manifold.

that the turbulent flow-field is established excluding any further influence of the initialization from the NFGM field.

Another peculiar aspect is how the mixture composition is distributed with regards to the swirling jet considering the last picture on the right of Figure 5.8. While the relatively high values of z around 0.0338 (corresponding to $\lambda = 1.91$, the nominal value for this operating condition) in the corners of the flame tube are associated with the recirculation of the exhaust, the local richer regions close to the burner axis is due to the

evaporation of the spray, as it will be discussed later. It can be observed that in the NFGM simulation a large richer zone is present a few millimeters downstream the nozzle exit: since here the same clip value of 0.045 is used for both the simulations, aiming to allow a comparison between these two models, it is not excluded that points with local stoichiometric composition (i.e., $z = 0.0626$) could be present. This fact might be related to the very low flame stabilization position, which affects the evaporation of the fuel in a small region, increasing the local value of z.
On the contrary, the TF-FGM model presents a more uniform and distributed field of z, where the local richer zones can be observed from 20 mm. It should be said that this comparison will be better described considering mean fields for such quantity, and possibly considering the fuel concentration maps. as it will be included in the future.

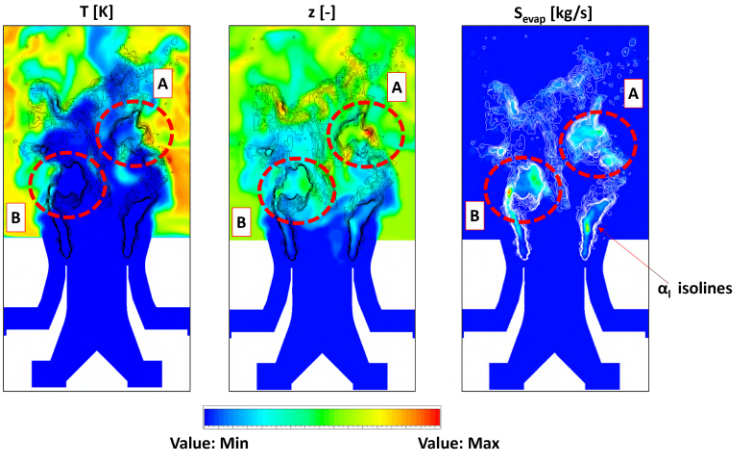

Figure 5.9: Instantaneous contour of temperature (left), z (mid) and soruce term of DPM evaporation (right) in the nozzle near field with liquid volume fraction α_l isolines superimposed for the TF-FGM simulation. The red dashed circles highlight two different operating modes for the liquid-gas interaction.

All in all, concerning the results available at this moment, it can

be affirmed that the TF-FGM model is effectively introducing some improvements with respect to the standard FGM approach (even if taking into account the heat loss effects in the tabulation).
In this last part some comments about the spray injection are carried out thanks to Figures 5.9. The α_l isolines are clipped to an arbitrary value evaluated accordingly to the maximum value present if the only flame tube (i.e., without the region inside the nozzle) is considered.
Here, thanks to these, the action of the turbulent flow-field on the spray injection can be observed. Moreover, differently from the mixture fields reported in Chapter 4, it can be seen that the internal channels of the nozzle are almost completely dominated by pure air, while air-fuel mixture begins to appear only where the evaporation occurs.
If the turbulent structures highlighted with the red dashed circle in Figure 5.9 is considered, it can be seen how a local richer composition is occurring where the hot recirculation products are entrained in the swirling jet, enhancing the local evaporation rate. Considering therefore Figure 5.10, where the same maps in terms of PFR are reported, it is clear that the reaction occurs where the flow structures in the outer shear layer and the spray interacts (label A).
However, considering label B in the same figures, it can be observed that a local high evaporation rate is reached with the subsequent presence of fuel, without the occurrence of the reaction. In this fashion, the premixing process within the LOH, as explained in Chapter 2 seems to be correctly predicted. Future investigations are therefore required before drawing some conclusions on this novel TF-FGM approach could with advanced spray boundary conditions.

Concluding remarks

In this last chapter, all the modelling efforts carried out in this research activity concerning the low-swirl lifted flame object of this study are gathered together. Moreover, ad hoc boundary conditions from the dedicated study are employed aiming to have a better characterization of

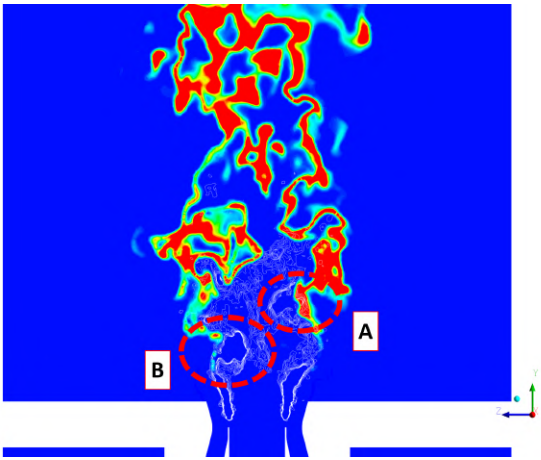

Figure 5.10: Instantaneous contour of PFR in the nozzle near field with liquid volume fraction α_l isolines superimposed for the TF-FGM simulation.

the spray at the early stage of the atomization.
A first comparison in terms of instantaneous and averaged maps points out that the flame is stabilized too low with respect to the available experimental data. Nevertheless, the TF-FGM model with Non-Adiabatic manifold, carried out in the previous chapter on the gaseous flame test case has shown a superior prediction with respect to the NFGM model. In the followings some considerations are reported for future investigations and improvements of such numerical modelling:

- The first obvious comment concerns the multiphase modelling within the reactive simulations. The spray introduces not only an additional phase to be modeled, but also a more complex fuel to take into account in the reaction process. In these regards, the spray modelling should investigate if some assumptions are really adequate, such as the TAB model for the Secondary Breakup: this model is known in the literature [28, 91] to over predict the droplets breakup. Although this has been successfully employed in some previous works [156],

the use of different modelling concerning this phenomenon could lead to a delay in the evaporation and ultimately in increase of the flame LOH;

- The more complex fuel (i.e., $NC_{10}H_{22}$) could have a different impact on some parameters within the TF-FGM approach (e.g., the laminar flame thickness δ which controls the thickening factor F), and generally speaking could not be understood with the considerations carried out for the TF-FGM simulations with gaseous fuel. Some further investigations are required in this sense;

- Another strong assumption is, as usual, the imposed wall thermal boundary condition. Apart from the need for more detailed information concerning this region, it should be clear that a different profile of wall temperature (see Figure 5.3) could affect the flame position. In future works a sensitivity to this boundary conditions definition should be conducted to this aim;

- Although its wide popularity in the scientific literature, the comparison between OH* chemiluminescence maps and Product Formation Rate might be misleading, since it has also shown that the correspondence between the peak of OH* emissivity could be delayed with respect to one of reaction rate [161]. In this regard, a dedicated sub-mechanism for the inclusion of the excited radical OH* has be employed within the chemical mechanism within the reactive calculations. Nevertheless, more tests are required to assess the impact of these modification with respect to the original Luche's mechanism;

- Finally, the TF-FGM has proved its capability in the description of the turbulence-chemistry effects, but still such type of combustion modelling relies on the look-up table computed a priori. In this regards, further investigation are required to understand how this aspect can be improved and how it will affect the final flame shape, such as the preliminary study reported in Chapter A. As well, the

impact of the aerodynamic stretch, such as described in Chapter 4 for the gaseous flame could play a role and it should be investigated in deep;

Conclusions

The research activity discussed in this dissertation has been carried out with the aim of enabling a quick and safe diffusion of the lean burn combustor concept for air civil transportation. The interest in such investigation is justified by the current trends in pollutant emissions reduction in the design of modern combustor concepts, which could lead to potential technological issues about the combustion process and overall reliability of the aero-engine. Also, the importance of disruptive low-emissions technologies, especially with respect to the NO_x emissions is discussed widely in the Introduction. Indeed, large research efforts have been devoted to the development of such combustion systems which are considered as the most effective technology to meet the future increasingly emission standards imposed by ICAO-CAEP.

This purpose is pursued by focusing on an innovative combustion chamber concept studied in the EU project CHAiRLIFT, where low-swirl spray lifted flames are gathered with an inclined arrangement of the burners, the so-called SHC. The aim is to promote a macro-recirculation of hot combustion products which will improve the combustion stability at ultra-lean equivalence ratios, therefore averting Lean Blow-Off occurrences. Moreover, these two concepts will allow some further benefits, such as avoiding flashback risks and reducing the overall mass of the engine, other than cooling air requirement. In this fashion, in Chapter 1, a detailed discussion the current low-emission technologies and the improvement introduced with the CHAiRLIFT burner with respect to these, is reported.

This interesting concept, however, introduces also some complexities in terms of interaction between adjacent flames. Understanding these phenomena other than exploring some operating conditions and burners arrangement for the inclination could not be possible without proper numerical tools within the CFD framework. For this reason, in Chapter 2, a first overview on the fundamental physics behind this low-swirl lifted flame stabilization is reported, together with the numerical analysis of the flow-field in non reactive conditions with the commercial CFD suite ANSYS Fluent. Here, it can be observed that Scale Resolving approaches such as LES simulation can effectively predict with success the specific flow-field associated with this burner.

Although this first outcome concerning turbulence modelling, a multiphysics approach is needed when investigating the CHAiRLIFT multi-burner configuration currently under-testing at KIT. This configuration consists of five burners disposed in a linear array arrangement and shifted in the axial direction accordingly to the investigated tilt angle. In turns, these burners employ liquid fuel and various operating conditions can be imposed. In Chapter 3, a robust and affordable numerical setup is carried out to investigated such test rig: the modelling choices are validated with the experimental data available so far and further tilt angles are investigated with respect to the current test rig configuration. To this aim, RANS turbulence modelling is applied together with FGM approach for the turbulent combustion modelling and DPM methods for the spray description.

This study has also pointed out that, when low-swirl flames are employed, the best setup in terms of burner's inclination to maximize the recirculation of the exhaust stands between 20° and 30°. This fact is very interesting, since the original investigators of the SHC concept found that this corresponds to 45° if high-swirl nozzles are used.

Furthermore, a large amount of the efforts devoted to the multirig studies was aimed to understand how the outlet section should be designed to avoid back-flow recirculation, which could affect the interaction among flames. In this regard, further investigation concerning how the finite

geometry of the test rig differs from a real annular combustor should be investigated in the future.
Another crucial point is that the strategy concerning the numerical modelling carried out for this specific operating condition might be not adequate when different test points (e.g., inlet air preheating) are considered. The last part of Chapter 3 introduces and discusses these issues through the low-swirl flame operated with gaseous fuel in single sector configuration.

Aiming to understand which combustion models among the state-of-the-art approaches for LES context is the best candidate in terms of accuracy, cost-effectiveness and information concerning pollutant emissions, a sensitivity study is carried out on the low-swirl lifted flame in single sector configuration with gaseous fuel in Chapter 4. From this study, the importance of the aerodynamic stretch and heat loss actions on the local flame front is highlighted for the investigated burner. Moreover, it is demonstrated that the FGM model and a modified version of this approach, including stretch and heat loss effects, and called FGM-EXT, are not adequate to model this flame. On the contrary, if the direct resolution of the flame front is performed with the TF model, the flame lift-off and general representation are largely improved.
The main drawback of the TF model is due to its high demanding approach in terms of computational efforts when several chemical species are included in the simulation. This fact is important to understand the benefits of the CHAiRLIFT burners in terms of pollutant emissions. With the purpose of maintaining the description of the turbulence effects on the flame front given by the TF approach, but also the detailed information related to a tabulated chemistry one as the FGM, a hybrid TF-FGM approach is considered in the second part of Chapter 4. Moreover, due to the great relevance of the heat loss modelling for this type of flame, a revised manifold including the heat loss is used. Another improvement is represented by the test of two different formulations for the efficiency function employed in the thickening procedure.
The final outcome is that the TF-FGM approach is providing the best

prediction in terms of lift-off and flame shape, also with respect to the previous results with the pure TF model. In this regard, both the formulations of the efficiency function report very interesting results, even if the one with a more detailed computation of the velocity fluctuation seems to further improve the results. Nevertheless, before drawing further conclusions, more investigations are required in terms of the final effects of the Efficiency Function on the flame front. Moreover, detailed thermal boundary conditions are mandatory to avoid affecting the final results with an ill-conceived numerical setup.

Finally, in Chapter 5, the newly introduced numerical modelling is applied again to the single sector configuration operated with liquid fuel. This situation introduced new challenges both in terms of multi-phase modelling and turbulent combustion one.
The former is handled with the DPM method, as in Chapter 3, but with ad hoc boundary conditions coming from a novel approach in the literature proposed by the CORIA research team. The main differences with respect to commonly adopted approaches in the multi-phase modelling framework are the use of the liquid structures' curvature for estimating the droplets diameters distribution and initial velocity. Turbulent combustion modelling instead should potentially carry out a proper flame description, as in Chapter 4, but the preliminary results are showing a not negligible discrepancy with the available experimental data.
To summarize, the TF-FGM model has shown potential when applied to gaseous flame, but further investigation are required before extending this approach to more complex type of fuels. Moreover, also the strategy behind the Non-Adiabatic PDF should more investigated, since this approach is not taking into account currently of the aerodynamic stretch impact on the manifold. Other than this, the next step of this research activity will involve the use of the final multiphysics model to the tilted configuration of the burner, aiming to assess the potential of the CHAiRLIFT concept.

Appendix A

RANS chemistry tabulation tests

The purpose of this appendix is to provide an overview of possible alternative strategies for the chemistry tabulation within the FGM approach. Different laminar structures are employed to obtain the look-up tables, hence to evaluate the global reactivity of the process. The impact of this description has been suggested by previous work by Galeazzo [109] on a similar test case, where the look-up table is obtained from a zero-dimensional reactor governed by auto-ignition phenomena. This step emphasis that the representation of a lifted flame through a conventional premixed flamelet is not obvious, due to the complex physics involved.

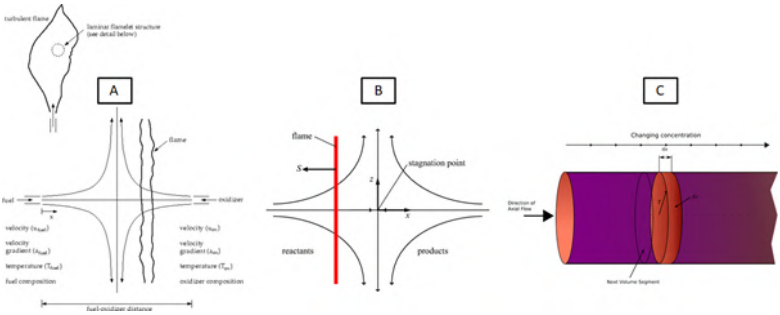

Figure A.1: 1D fundamental flame structures overview.

In order to allow a representative but cost-effective analysis, a 10 deg periodic sector of the domain reported in Chapter 2 is here considered. In this case, the swirler is not included entirely, while the reactive mixture inlet is placed 2.5 mm upstream of the prefilmer lip: the final mesh grid consists of 400 K hexahedral elements.
The boundary conditions are therefore from the previous LES simulation in terms of circumferentially averaged profiles for the quantities of interest (i.e., velocity components, temperature, and mixture fraction), similar to the approach employed in Chapter 3 for the investigation of the multiburner. Turbulence modeling is particularly crucial since the numerical domain starts in a region distinguished by a high degree of velocity fluctuations. Therefore, the profiles of Turbulence Kinetic Energy (k) and Turbulent Dissipation Rate (ϵ) have been evaluated from the previous LES calculations, then applied to the mixture inlet. Moreover, the k-ϵ realizable approach has been used to model the turbulence within the RANS calculation. These steps help to mitigate the use of a rotational periodic numerical domain, but clearly, the physics of the problem would be affected, especially in terms of the flow-field. Nonetheless, it is worthy to point out that the final goal of this study is a comparison among combustion modeling strategies rather than a detailed description of the flame.
At this point, it is worth recalling that the FGM approach is based on a priori chemistry tabulation: the underlying thermochemical states are assumed represented in 1D laminar structures called flamelets. Considering the following tests, the combustion model adopted is fundamentally the same, but with a chemistry tabulation obtained from different one-dimensional (or zero-dimensional) structures (see Figure A.1), described as follows:

- Diffusive flamelets: pure oxidizer is injected against pure fuel (Figure A.1 – label A). The velocity imposed at the inlet of the two opposed streams determines the strain level, thus the reaction rate.

- Premixed counter-flow flamelets: premixed reactants are injected

against combustion products (Figure A.1 – label B). A consideration similar to the previous one can be drawn for the reaction rate.

- Premixed freely propagating flamelets: premixed reactants and combustion products are injected as coflowing streams (not reported in the figure),

- Plug Flow Reactor (PFR): reactants are perfectly premixed in a "reactor", advanced along the axial coordinate (Figure A.1 – label C) considering a given axial transport and specific time step. The main feature of the PFR is that backward transport is neglected, so the mixing process. Hence, the reaction that takes place is due to an initial autoignition event.

For each of those, a look-up table has been carried out as a function of the mixture fraction z and the progress variable c with a python script integrated with CANTERA v2.4.0. Therefore, these tables have been employed in the ANSYS Fluent 2019R1 CFD suite. An instance of the different outcomes obtained from the considered laminar structures can be seen in Figure A.2, where the Rate of progress variable (i.e., the progress variable source term in the related per unit mass of the results in Section 3.2) is reported as a function of c, for the stoichiometric mixture fraction. This plot points out as different laminar structures affect both the peak value of the mentioned source term as well as the distribution in function of the progress variable.

The chemistry tabulation comparison is reported in Figure A.3 in terms of the source term of the progress variable, $\dot{\omega}_c$ as an indicator of the ongoing reaction. The contours are normalized over the maximum value reached for the specific tabulation and line-of-sight integrated, where the intent is to visualize the main reaction zone and its extension for the various tabulations. The labels in the figure refer to different laminar structures and they will be used as a reference for further description.
The diffusive flamelet (Figure A.3 - A-Top) shows an elonged shape of the flame and a relatively high value of lift-off height (circa 63 mm). This behavior can be explained considering that this type of flamelet is

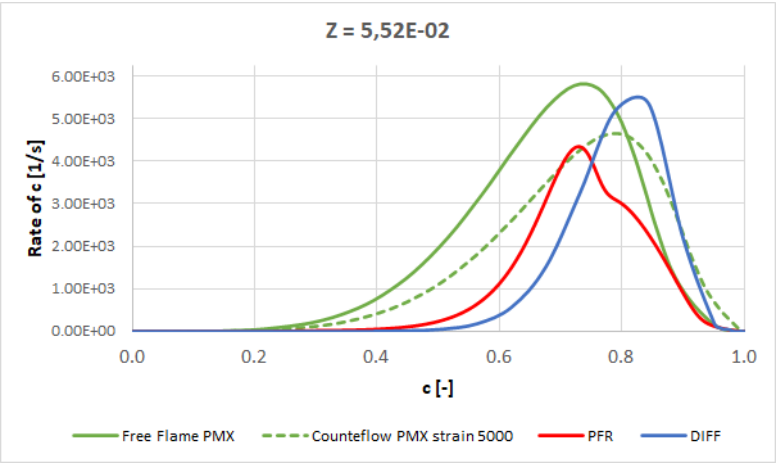

Figure A.2: Rate of progress variable in function of the reaction progress for the considered laminar structures at the stoichiometric mixture fraction.

mainly driven by the mixing process between fuel and oxidizer rather than autoignition phenomena. This idea is suggested by the trend observed for the diffusive flamelet in Figure A.2, where for a given mixture fraction, the rate of the reaction takes place in a relatively narrow range of progress variable, with a peak value close to the one of the free flame. Also, for low values of the progress variable, lower values of the reaction rate are occurring with respect to the other types of tabulation: also this aspect allows the flame to stabilize downstream, where higher values of the progress variable are reached.

As expected, the free-flame configuration (Figure A.3 – B-Top) overestimates the reactivity of the combustion process, and it provides the lowest flame among the ones here considered. This result is in line with the one already seen for the LES calculation for the FGM baseline results and it can be understood looking at Figure A.2, where the free flame curve exhibit the highest value of the rate of progress variable for the laminar structures set, other than the wider distribution. If the level of strain

is increased (i.e., increasing the velocity at which the stream are being injected against each other in the premixed flamelet) as in Figure A.3 – C-Top and D-Top, the flame stabilized downstream and has a larger axial extension. The aerodynamic actions of the flow-field on the flame front weakens the reaction, hence results in a less intense combustion process. The related flame speed assumes a lower value, therefore the flame stabilized downstream, where the swirling jet from the nozzle has a lower velocity.
The last case here considered, Figure A.3 – E-Top, represents the chemistry tabulation obtained from the Plug-Flow Reactor, that as already mentioned, assumed perfect premix among fuel, oxidizer, other than the combustion products once the reaction has started due to autoignition. The underlying concept for this type of tabulation is that the combustion process is controlled by the chemistry kinetics rather than mixing or possible aerodynamic actions related to the flow-field. Considering this, the flame shows an elonged shape similar to the case with higher imposed strain.

Additionally, Figure A.3 Bottom reports the same comparison among chemistry tabulation strategies with an increased level of turbulence imposed to the inlet. It is possible to observe that the same trend already explained for the previous level of turbulence is still valid for the related 1D laminar structures. However, the turbulence enhances the reaction, resulting in a reduction of the lift-off height for all the cases: moreover, the free flame tabulation case (Figure A.3 B-Bottom) brings to an almost attached flame with a shape of the main reaction zone specular respect to the other flames.
In conclusion, this comparison points out that in the context of the FGM approach, the complex physics behind a lifted flame, at least in the case of gaseous fuel for this operating point, are better represented in the case of premixed flamelets with an imposed level of strain, or considering that combustion is mainly driven by the chemistry kinetics, such as in the PFR-like structures. Although these concepts require a further investigation with a more realistic configuration of the burner, they will be used as a

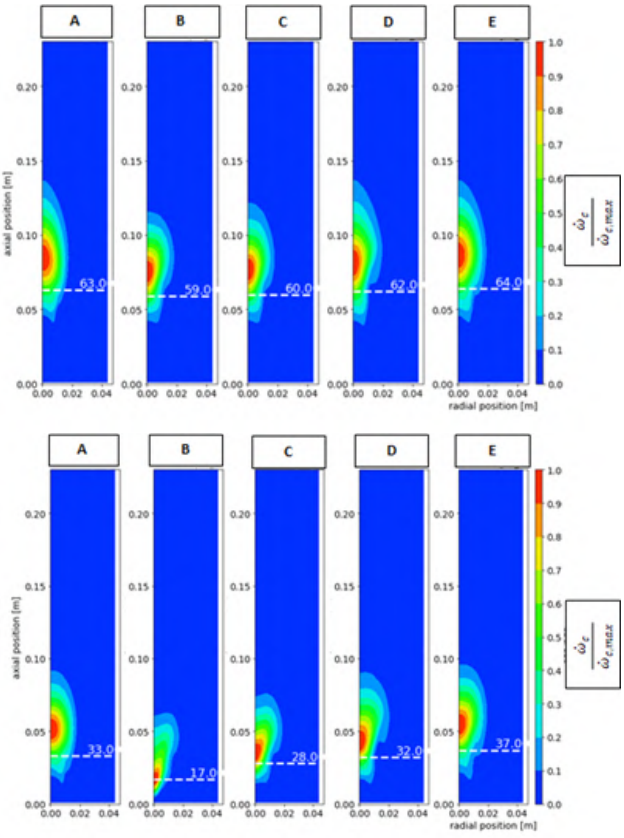

Figure A.3: Progress variable source term maps on the midplane for various chemistry tabulation strategies (A: diffusive flamelets; B: premixed free flame; C: premixed counter-flow flame – strain: 1000 1/s; D: premixed counter-flow flame – strain: 5000 1/s; E: plug flow reactor). Top: baseline turbulence imposed to the inlet section. Bottom: increased level of turbulence imposed to the inlet section.

starting point for the next calculations.

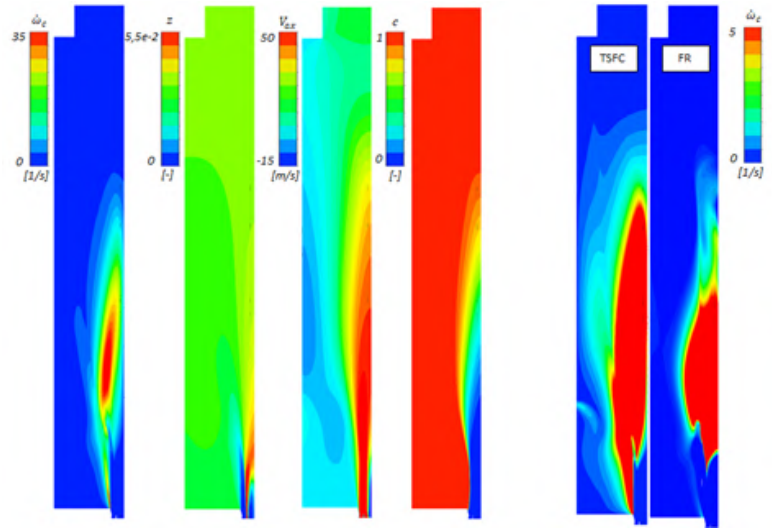

Figure A.4: Left: contour maps of (from left to right) progress variable source term, mixture fraction, axial velocity and progress variable for the periodic sector test case with the TSFC model. Right: Contour map of progress variable source term $\dot{\omega}_c$ of the TSFC model (left) and the FR one (right).

The second part of this study focused on the progress variable transport equation source term closure. This step aims to investigate how the two most diffused approach, the Turbulent Flame Speed Closure (TSFC) and the Finite Rate (FR) approach, affects the flame representation. It should be noted that the FR modeling has been employed for all the calculations described so far. The chemistry tabulation is the same shown previously obtained with premixed counterflow flamelets (imposed strain level: 1000 1/s).

In Figure A.4, the results from the FGM approach with TSFC modeling of the source term are reported in term of the contour map at the midplane of progress variable source term $\dot{\omega}_c$, axial velocity V_{ax}, mixture fraction

z, and progress variable c. Respect to the previous results with the FR model, the peak value of $\dot{\omega}_c$ assumes a value one order of magnitude below the ones seen in the previous comparison (Figure A.3). Moreover, the flame appears distributed on a wider zone rather than concentrated on a thin front where the flow velocity and the local composition allow the stabilization.

Although this favorable aspect, the main issue is represented by the attachment of the flame to the nozzle outlet, which results in a rim-stabilized flame rather than a lifted one. This aspect could be explained considering that the reaction zones mainly reflect the trend of the gradient of progress variable, other than the values of the velocity turbulence fluctuations u' and the laminar flame speed, therefore the local composition of the mixture. A detailed discussion of the TSFC model is out of scope here and the interested reader is addressed to [120].

In the injector near field, the shear-layer between the jet issuing from the nozzle and the ORZ raises the values of u'. Moreover, here also a large value of the progress variable gradient can be found since the combustion products transported upstream from the ORZ meet the fresh mixture coming from the nozzle. This allows the flame to stabilize in a region where values of the mixture fraction close to zero are found, which clearly is not physical. This behavior is emphasized in Figure A.4, where the progress variable source term map for both the TFSC and the FR closure are reported and clip to a very low value in order to highlight the zones interested by even a low reactivity. It can be seen that for the FR closure negligible value of $\dot{\omega}_c$ near the nozzle outlet rim, confirming its eligibility to represent the lift-off occurrence.

Appendix B

Mesh elements sensitivity

With respect to the reactive test point simulations reported in Section 3.4, further tests regarding the sensitivity to the mesh grid arrangement on the same operating point has been performed. This test aimed to evaluate the effects of three different aspects:

- The extension and disposition of the local refinement area in the combustion chamber, such as in the new grids it extends deeper in the flame tube;
- The mesh grid sizing;
- The mesh grid element type, that are tetrahedral elements and polyhedral ones;

This test has been performed in LES context with the only standard FGM model in order to evaluate uniquely the effects of the flow-field discretization itself, adopting the same settings presented in subsection 2.2. The new local refinement now included the whole area interested by the reaction in the flame tube (i.e., up to 200 mm for this operating condition), which largely increases the number of elements in the grid, since the large extension of this type of flame. The results are reported in Figure 11, while in Table B.1 are resumed the associated computational costs.

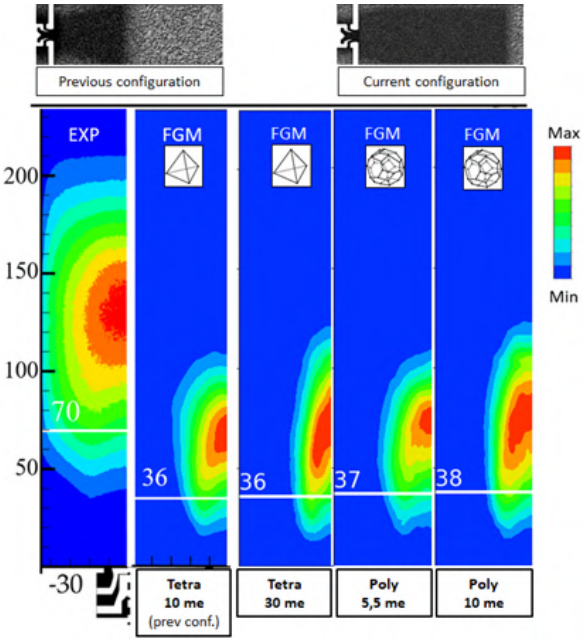

Figure B.1: Line-of-sight contours maps of EXP experimental OH emission intensity map [70] and progress variable source term maps (LES-FGM model) for various mesh grids.*

Case	Clock time per time step $[s]$	Estimation Single PVC $[cpuh]$
Tetra 10 M	18	369E+3
Tetra 30 M	27	583E+3
Poly 5.5 M	6	115E+3
Poly 10 M	8-7	155E+3

Table B.1: Computational cost for the various mesh grids employed in the mesh sensitivity tests.
Number of employed CPUs: 280. Precessing Vortex Core (PVC) period: 0.25 s.

It can be observed that by changing the local refinement disposition, the flame extends in the combustion chamber, therefore avoiding the dissipative effects of a coarse mesh in the flame tube. Instead, the LOH, as well as the position of the flame base, remain unaffected at least with the FGM model. Moreover, these tests have pointed out that the polyhedral elements available in ANSYS Fluent allow an accuracy comparable with the usual tetrahedral mesh grids, but with a much lower computational cost, reduced by a factor of roughly 3 as reported in Table B.1.
Although the outcomes of this study have provided useful insight into the combustion modeling, further investigation is required, possibly based on more quantitative comparisons

List of Figures

List of Tables

Bibliography

[1] Liu, Yize, Sun, Xiaoxiao, Sethi, Vishal, Nalianda, Devaiah, Li, Yi-Guang, and Wang, Lu. "Review of modern low emissions combustion technologies for aero gas turbine engines." *Progress in Aerospace Sciences*, 94:12–45, 2017.

[2] Paccati, Simone. *Development of advanced numerical tools for the prediction of wall temperature and heat fluxes for aeroengine combustors*. PhD thesis, University of Florence, 2021.

[3] Lefebvre, Arthur H and Ballal, Dilip R. *Gas turbine combustion: alternative fuels and emissions*. CRC press, 2010.

[4] Madden, Paul. "Caep combustion technology review process and caep nox goals." *CAEP Publication July*, 2014.

[5] Flightpath, ACARE. "2050-europe's vision for aviation." *Advisory Council for Aeronautics Research in Europe*, 2011.

[6] Grewe, Volker, Rao, Arvind Gangoli, Grönstedt, Tomas, Xisto, Carlos, Linke, Florian, Melkert, Joris, Middel, Jan, Ohlenforst, Barbara, Blakey, Simon, Christie, Simon, et al. "Evaluating the climate impact of aviation emission scenarios towards the paris agreement including covid-19 effects." *Nature Communications*, 12(1):1–10, 2021.

[7] Nojoumi, H, Dincer, I, and Naterer, GF. "Greenhouse gas emissions

assessment of hydrogen and kerosene-fueled aircraft propulsion." *International journal of hydrogen energy*, 34(3):1363–1369, 2009.

[8] Yılmaz, İlker, İlbaş, Mustafa, Taştan, Murat, and Tarhan, Cevahir. "Investigation of hydrogen usage in aviation industry." *Energy conversion and management*, 63:63–69, 2012.

[9] Yilmaz, Nadir and Atmanli, Alpaslan. "Sustainable alternative fuels in aviation." *Energy*, 140:1378–1386, 2017.

[10] Amerini, Alberto, Langone, Leonardo, Vadi, Riccardo, and Andreini, Antonio. Assessment of a hybrid propulsion system for short-mid range application with a low-order code. In *E3S Web of Conferences*, volume 312, page 11005. EDP Sciences, 2021.

[11] Vouros, Stavros, Kavvalos, Mavroudis, Sahoo, Smruti, and Kyprianidis, Konstantinos. "Enabling the potential of hybrid electric propulsion through lean-burn-combustion turbofans." *Journal of the Global Power and Propulsion Society*, 5:164–176, 2021.

[12] PENANHOAT, Olivier. "Low emissions combustor technology developments in the european programmes lopocotep and tlc." *Proceedings of the 25th ICAS, Hamburg, Germany*, 2006.

[13] Liu, Kexin, Burluka, AA, and Sheppard, CGW. "Turbulent flame and mass burning rate in a spark ignition engine." *Fuel*, 107:202–208, 2013.

[14] Ranasinghe, Kavindu, Guan, Kai, Gardi, Alessandro, and Sabatini, Roberto. "Review of advanced low-emission technologies for sustainable aviation." *Energy*, 188:115945, 2019.

[15] de Oliveira, Pedro M, Fredrich, Daniel, De Falco, Gianluigi, El Helou, Ingrid, D'Anna, Andrea, Giusti, Andrea, and Mastorakos, Epaminondas. "Soot-free low-no x aeronautical combustor concept: The lean azimuthal flame for kerosene sprays." *Energy & Fuels*, 35(9):7092–7106, 2021.

[16] Zhao, Dan, Gutmark, Ephraim, and de Goey, Philip. "A review of cavity-based trapped vortex, ultra-compact, high-g, inter-turbine combustors." *Progress in Energy and Combustion Science*, 66:42–82, 2018.

[17] Yin, Feijia and Rao, Arvind Gangoli. "A review of gas turbine engine with inter-stage turbine burner." *Progress in Aerospace Sciences*, 121:100695, 2020.

[18] Gicquel, Laurent YM, Staffelbach, Gabriel, and Poinsot, Thierry. "Large eddy simulations of gaseous flames in gas turbine combustion chambers." *Progress in energy and combustion science*, 38(6):782–817, 2012.

[19] Arroyo, Carlos Pérez, Dombard, Jérôme, Duchaine, Florent, Gicquel, Laurent, Martin, Benjamin, Odier, Nicolas, and Staffelbach, Gabriel. "Towards the large-eddy simulation of a full engine: Integration of a 360 azimuthal degrees fan, compressor and combustion chamber. part i: Methodology and initialisation." *Journal of the Global Power and Propulsion Society*, 2021(May):1–16, 2021.

[20] Zeldovich, YA, Frank-Kamenetskii, D, and Sadovnikov, P. *Oxidation of nitrogen in combustion.* Publishing House of the Acad of Sciences of USSR, 1947.

[21] Innocenti, Alessandro. *Numerical analysis of the dynamic response of practical gaseous and liquid fuelled flames for heavy-duty and aero-engine gas turbines.* PhD thesis, University of Florence, 2015.

[22] Li, Jianzhong, Chen, Jian, Yuan, Li, Hu, Ge, and Feng, Jianhan. "Flow characteristics of a rich-quench-lean combustor-combined low-emission and high-temperature rise combustion." *International Journal of Aerospace Engineering*, 2019, 2019.

[23] Hatch, M, Sowa, W, SAMUELSON, G, and Holdeman, J. Jet mixing into a heated cross flow in a cylindrical duct-influence of

geometry and flow variations. In *30th Aerospace Sciences Meeting and Exhibit*, page 773, 1992.

[24] Holdeman, James D and Chang, Clarence T. "The effects of air preheat and number of orifices on flow and emissions in an rql mixing section." 2007.

[25] Darwish, M, Abdulrahim, H, Mabrouk, A, and Hassan, A. "Cogeneration power-desalting plants using gas turbine combined cycle." *Desalination updates*, page 127, 2015.

[26] Koff, BL. "Aircraft gas turbine emissions challenge." 1994.

[27] Vervisch, L., Veynante, D., and Van Beeck, JPAJ. *Turbulent Combustion: May 20-24, 2019*. Von Karman Institute for Fluid Dynamics, 2019.

[28] Giusti, Andrea. *Development of numerical tools for the analysis of advanced airblast injection systems for lean burn aero-engine combustors*. PhD thesis, University of Florence, 2013.

[29] Mongia, Hukam. Taps: A fourth generation propulsion combustor technology for low emissions. In *AIAA International Air and Space Symposium and Exposition: The Next 100 Years*, page 2657, 2003.

[30] Lefebvre, Arthur H and McDonell, Vincent G. *Atomization and sprays*. CRC press, 2017.

[31] Mazzei, L, Puggelli, S, Bertini, D, Andreini, A, Facchini, B, Vitale, I, and Santoriello, A. "Numerical and experimental investigation on an effusion-cooled lean burn aeronautical combustor: Aerothermal field and emissions." *Journal of Engineering for Gas Turbines and Power*, 141(4), 2019.

[32] Giusti, Andrea, Andreini, Antonio, Facchini, Bruno, Vitale, Ignazio, and Turrini, Fabio. Thermoacoustic analysis of a full annular aero-engine lean combustor with multi-perforated liners. In *19th AIAA/CEAS Aeroacoustics Conference*, page 2099, 2013.

[33] Puggelli, S, Bertini, D, Mazzei, L, and Andreini, A. "Modeling strategies for large eddy simulation of lean burn spray flames." *Journal of Engineering for Gas Turbines and Power*, 140(5), 2018.

[34] Mazzei, Lorenzo. *A 3d coupled approach for the thermal design of aeroengine combustor liners*. PhD thesis, University of Florence, 2014.

[35] Poggiali, Matteo. *Development of a new combustor liners thermal design procedure through low order codes and uncertainty quantification tools*. PhD thesis, University of Florence, 2021.

[36] Palanti, Lorenzo. *On the modelling of liquid fuel ignition and atomization in aero engine combustors*. PhD thesis, University of Florence, 2021.

[37] `https://cordis.europa.eu/project/id/831881/en`.

[38] Wohl, Kurt, Kapp, Numer M, and Gazley, Carl. The stability of open flames. In *Symposium on Combustion and Flame, and Explosion Phenomena*, volume 3, pages 3–21. Elsevier, 1948.

[39] Jella, SE, Kwong, WY, Steinberg, AM, Park, JW, Lu, T, Bergthorson, JM, and Bourque, G. "Attached and lifted flame stabilization in a linear array of swirl injectors." *Proceedings of the Combustion Institute*, 38(4):6279–6287, 2021.

[40] Kasabov, Plamen. *Experimentelle Untersuchungen an abgehobenen Flammen unter Druck*. PhD thesis, 2014.

[41] Vanquickenborne, L and Van Tiggelen, A. "The stabilization mechanism of lifted diffusion flames." *Combustion and Flame*, 10(1): 59–69, 1966.

[42] Cabra, R, Chen, J-Y, Dibble, RW, Karpetis, AN, and Barlow, RS. "Lifted methane–air jet flames in a vitiated coflow." *Combustion and Flame*, 143(4):491–506, 2005.

[43] O'Loughlin, W and Masri, AR. "A new burner for studying auto-ignition in turbulent dilute sprays." *Combustion and Flame*, 158 (8):1577–1590, 2011.

[44] Tagliante, Fabien, Poinsot, Thierry, Pickett, Lyle M, Pepiot, Perrine, Malbec, Louis-Marie, Bruneaux, Gilles, and Angelberger, Christian. "A conceptual model of the flame stabilization mechanisms for a lifted diesel-type flame based on direct numerical simulation and experiments." *Combustion and Flame*, 201:65–77, 2019.

[45] Lawn, C.J. "Lifted flames on fuel jets in co-flowing air." *Progress in Energy and Combustion Science*, 35(1):1–30, 2009.

[46] Lyons, Kevin M. "Toward an understanding of the stabilization mechanisms of lifted turbulent jet flames: experiments." *Progress in Energy and Combustion Science*, 33(2):211–231, 2007.

[47] Merlo, Nazim, Boushaki, Toufik, Chauveau, Christian, de Persis, Stephanie, Pillier, Laure, Sarh, Brahim, and Gokalp, Iskender. "Experimental study of oxygen enrichment effects on turbulent non-premixed swirling flames." *Energy & fuels*, 27(10):6191–6197, 2013.

[48] Sayad, Parisa, Schonborn, Alessandro, and Klingmann, Jens. "Experimental investigations of the lean blowout limit of different syngas mixtures in an atmospheric, premixed, variable-swirl burner." *Energy & fuels*, 27(5):2783–2793, 2013.

[49] Jerzak, Wojciech and Kuźnia, Monika. "Experimental study of impact of swirl number as well as oxygen and carbon dioxide content in natural gas combustion air on flame flashback and blow-off." *Journal of Natural Gas Science and Engineering*, 29:46–54, 2016.

[50] Syred, Nicholas. "A review of oscillation mechanisms and the role of the precessing vortex core (pvc) in swirl combustion systems." *Progress in Energy and Combustion Science*, 32(2):93–161, 2006.

[51] Jourdaine, Paul, Mirat, Clément, Caudal, Jean, and Schuller, Thierry. "Stabilization mechanisms of swirling premixed flames with an axial-plus-tangential swirler." *Journal of Engineering for Gas Turbines and Power*, 140(8), 2018.

[52] Johnson, MR, Littlejohn, D, Nazeer, WA, Smith, KO, and Cheng, RK. "A comparison of the flowfields and emissions of high-swirl injectors and low-swirl injectors for lean premixed gas turbines." *Proceedings of the Combustion Institute*, 30(2):2867–2874, 2005.

[53] Mansouri, Zakaria, Aouissi, Mokhtar, and Boushaki, Toufik. "A numerical study of swirl effects on the flow and flame dynamics in a lean premixed combustor." *International journal of heat and technology*, 34(2):227–235, 2016.

[54] Eichler, Christian Thomas. *Flame flashback in wall boundary layers of premixed combustion systems*. Verlag Dr. Hut, 2011.

[55] Chan, CK, Lau, KS, Chin, WK, and Cheng, RK. Freely propagating open premixed turbulent flames stabilized by swirl. In *Symposium (International) on Combustion*, volume 24, pages 511–518. Elsevier, 1992.

[56] Bedat, B and Cheng, RK. "Experimental study of premixed flames in intense isotropic turbulence." *Combustion and Flame*, 100(3): 485–494, 1995.

[57] Cheng, Robert K. Ultralean low swirl burner, April 7 1998. US Patent 5,735,681.

[58] Day, Marc, Tachibana, Shigeru, Bell, John, Lijewski, Michael, Beckner, Vince, and Cheng, Robert K. "A combined computational and experimental characterization of lean premixed turbulent low swirl laboratory flames: I. methane flames." *Combustion and Flame*, 159 (1):275–290, 2012.

[59] Shahsavari, Mohammad, Farshchi, Mohammad, and Arabnejad, Mohammad Hossien. "Large eddy simulations of unconfined non-reacting and reacting turbulent low swirl jets." *Flow, Turbulence and Combustion*, 98(3):817–840, 2017.

[60] Petersson, Per, Olofsson, Jimmy, Brackman, Christian, Seyfried, Hans, Zetterberg, Johan, Richter, Mattias, Aldén, Marcus, Linne, Mark A, Cheng, Robert K, Nauert, Andreas, et al. "Simultaneous piv/oh-plif, rayleigh thermometry/oh-plif and stereo piv measurements in a low-swirl flame." *Applied optics*, 46(19): 3928–3936, 2007.

[61] Cheng, RK, Littlejohn, D, Strakey, PA, and Sidwell, T. "Laboratory investigations of a low-swirl injector with h2 and ch4 at gas turbine conditions." *Proceedings of the Combustion Institute*, 32(2):3001–3009, 2009.

[62] Cheng, Robert K et al. "Low swirl combustion." *The Gas Turbine Handbook*, pages 241–255, 2006.

[63] Zarzalis, N., Fokaides, P.A., and Merkle, K. Fuel injection apparatus, 2005. DE Patent 10 2005 022 772.4, EP 06 009 563.5.

[64] Fokaides, P and Zarzalis, Nikolaos. Lean blowout dynamics of a lifted stabilized, non-premixed swirl flame. In *Proceedings of European Combustion Meeting*, volume 7, page 2, 2007.

[65] Fokaides, Paris A, Kasabov, Plamen, and Zarzalis, Nikolaos. "Experimental investigation of the stability mechanism and emissions of a lifted swirl nonpremixed flame." *Journal of engineering for gas turbines and power*, 130(1), 2008.

[66] Fokaides, P, Weiß, M, Kern, M, and Zarzalis, N. "Experimental and numerical investigation of swirl induced self-excited instabilities at the vicinity of an airblast nozzle." *Flow, turbulence and combustion*, 83(4):511–533, 2009.

[67] Kasabov, Plamen and Zarzalis, Nikolaos. Pressure dependence of the stability limits and the nox exhaust gas concentrations in case of swirl-stabilized, diffusion flames burning in a lift-off regime. In *Turbo Expo: Power for Land, Sea, and Air*, volume 48838, pages 613–622, 2009.

[68] Kasabov, P, Zarzalis, N, and Habisreuther, P. "Experimental study on lifted flames operated with liquid kerosene at elevated pressure and stabilized by outer recirculation." *Flow, turbulence and combustion*, 90(3):605–619, 2013.

[69] Sedlmaier, Julia, Habisreuther, Peter, Zarzalis, Nikolaos, and Jansohn, Peter. Influence of liquid and gaseous fuel on lifted flames at elevated pressure stabilized by outer recirculation. In *Turbo Expo: Power for Land, Sea, and Air*, volume 45684, page V04AT04A054. American Society of Mechanical Engineers, 2014.

[70] Sedlmaier, Julia. *Numerische und experimentelle Untersuchung einer abgehobenen Flamme unter Druck*. PhD thesis, 2019.

[71] Zhang, Feichi, Heidarifatasmi, Hosein, Harth, Stefan, Zirwes, Thorsten, Wang, Robert, Fedoryk, Michal, Sebbar, Nadia, Habisreuther, Peter, Trimis, Dimosthenis, and Bockhorn, Henning. "Numerical evaluation of a novel double-concentric swirl burner for sulfur combustion." *Renewable and Sustainable Energy Reviews*, 133:110257, 2020.

[72] Hall, Russell S. Spiral annular combustion chamber, September 19 1961. US Patent 3,000,183.

[73] Schutz, Herbert, Kraupa, Werner, and Termuhlen, Heinz. Gas turbine engine with tilted burners, September 7 1999. US Patent 5,946,902.

[74] Buret, Micher Roger, Cazalens, Michel Pierre, and Hernandez, Didied Hippolyte. Turbomachine with angular air delivery, July 12 2006. US Patent US20070012048A1.

[75] Burd, Steven and Cheung, Albert. Angled flow annular combustor for turbine engine, September 13 2007. US Patent 5,946,902.

[76] Ariatabar, Behdad, Koch, Rainer, Bauer, H-J, and Negulescu, D-A. "Short helical combustor: Concept study of an innovative gas turbine combustor with angular air supply." *Journal of Engineering for Gas Turbines and Power*, 138(3), 2016.

[77] Ariatabar, Behdad, Koch, Rainer, and Bauer, Hans-Jörg. "Short helical combustor: Flow control in a combustion system with angular air supply." *Journal of Engineering for Gas Turbines and Power*, 140(3), 2018.

[78] Hu, Bin, Zhang, JunHua, Deng, AiMing, Zhao, Wei, and Zhao, QingJun. Numerical investigation on single-restricted swirling flows in an innovative combustor. In *Turbo Expo: Power for Land, Sea, and Air*, volume 51067, page V04BT04A002. American Society of Mechanical Engineers, 2018.

[79] Zhang, Junhua, Hu, Bin, Fang, Aibing, Wang, Zhonghao, and Zhao, Qingjun. "Analysis of coherent structures in partly confined swirling flows." *Aerospace Science and Technology*, 107:106280, 2020.

[80] Savary, Nicolas and Taliercio, Guillaume. "The safran helicopter engine spinning flame combustor concept to meet customer needs." 2016.

[81] Agostinelli, Pasquale Walter, Kwah, Yi Hao, Richard, Stephane, Exilard, Gorka, Dawson, James R, Gicquel, Laurent, and Poinsot, Thierry. Numerical and experimental flame stabilization analysis in the new spinning combustion technology framework. In *ASME Turbo Expo*, 2020.

[82] Shamma, Mohamed, Harth, Stefan Raphael, Zarzalis, Nikolaos, Trimis, Dimosthenis, Hoffmann, Sven, Koch, Rainer, Bauer, Hans-Jörg, Langone, Leonardo, Galeotti, Sofia, and Andreini, Antonio.

Investigation of adjacent lifted flames interaction in an inline and inclined multi-burner arrangement. In *Turbo Expo: Power for Land, Sea, and Air*, volume 84959, page V03BT04A020. American Society of Mechanical Engineers, 2021.

[83] Hoffmann, Sven, Koch, Rainer, and Bauer, Hans-Jörg. Numerical investigation of the low-swirl flow in an aeronautical combustor with angular air supply. In *Turbo Expo: Power for Land, Sea, and Air*, volume 84928, page V02CT34A019. American Society of Mechanical Engineers, 2021.

[84] Giorgi, Maria Grazia De, Ficarella, Antonio, Fontanarosa, Donato, Pescini, Elisa, and Suma, Antonio. "Investigation of the effects of plasma discharges on methane decomposition for combustion enhancement of a lean flame." *Energies*, 13(6):1452, 2020.

[85] Fontanarosa, Donato, Mehdi, Ghazanfar, De Giorgi, Maria Grazia, and Ficarella, Antonio. Assessment of the impact of nanosecond plasma discharge on the combustion of methane air flames. In *E3S Web of Conferences*, volume 197, page 10001. EDP Sciences, 2020.

[86] Giorgi, Maria Grazia De, Bonuso, Sara, Mehdi, Ghazanfar, Shamma, Mohamed, Harth, Stefan Raphael, Zarzalis, Nikolaos, and Trimis, Dimosthenis. Enhancement of blowout limits in lifted swirled flames in methane-air combustor by the use of sinusoidally driven plasma discharges. In *Active Flow and Combustion Control Conference*, pages 66–82. Springer, 2021.

[87] Mehdi, Ghazanfar, Bonuso, Sara, and De Giorgi, Maria Grazia. "Effects of nanosecond repetitively pulsed discharges timing for aeroengines ignition at low temperature conditions by needle-ring plasma actuator." *Energies*, 14(18):5814, 2021.

[88] Ju, Yiguang and Sun, Wenting. "Plasma assisted combustion: Dynamics and chemistry." *Progress in Energy and Combustion Science*, 48:21–83, 2015.

[89] Kern, Matthias, Fokaides, Paris, Habisreuther, Peter, and Zarzalis, Nikolaos. Applicability of a flamelet and a presumed jpdf 2-domain-1-step-kinetic turbulent reaction model for the simulation of a lifted swirl flame. In *Turbo Expo: Power for Land, Sea, and Air*, volume 48838, pages 359–368, 2009.

[90] Langone, Leonardo, Sedlmaier, Julia, Nassini, Pier Carlo, Mazzei, Lorenzo, Harth, Stefan, and Andreini, Antonio. Numerical modeling of gaseous partially premixed low-swirl lifted flame at elevated pressure. In *Turbo Expo: Power for Land, Sea, and Air*, volume 84133, page V04BT04A068. American Society of Mechanical Engineers, 2020.

[91] ANSYS. *Fluent 19.3 Theory Guide*, 2019.

[92] Lilly, Douglas K. "A proposed modification of the germano subgrid-scale closure method." *Physics of Fluids A: Fluid Dynamics*, 4(3): 633–635, 1992.

[93] Langone, Leonardo, Amerighi, Matteo, and Andreini, Antonio. Numerical modeling of lean spray lifted flames in inclined multi-burner arrangements. In *Turbo Expo: Power for Land, Sea, and Air*. American Society of Mechanical Engineers, 2022. UNDER REVIEW.

[94] Van Oijen, JA, Lammers, FA, and De Goey, LPH. "Modeling of complex premixed burner systems by using flamelet-generated manifolds." *Combustion and Flame*, 127(3):2124–2134, 2001.

[95] Colin, O, Ducros, Frédéric, Veynante, D, and Poinsot, Thierry. "A thickened flame model for large eddy simulations of turbulent premixed combustion." *Physics of fluids*, 12(7):1843–1863, 2000.

[96] Chrigui, Mouldi, Gounder, James, Sadiki, Amsini, Masri, Assaad R, and Janicka, Johannes. "Partially premixed reacting acetone spray using les and fgm tabulated chemistry." *Combustion and flame*, 159 (8):2718–2741, 2012.

[97] Pierce, Charles D and Moin, Parviz. "Progress-variable approach for large-eddy simulation of non-premixed turbulent combustion." *Journal of fluid Mechanics*, 504:73–97, 2004.

[98] Wehrfritz, Armin, Kaario, Ossi, Vuorinen, Ville, and Somers, Bart. "Large eddy simulation of n-dodecane spray flames using flamelet generated manifolds." *Combustion and Flame*, 167:113–131, 2016.

[99] Shih, TH, Liou, WW, Shabbir, A, Yang, Z, and Zhu, J. "A new eddy-viscosity model for high reynolds number turbulent flows-model development and validation.-computers fluids. 24 (3). 227-238." 1995.

[100] Gepperth, S, Koch, R, and Bauer, H-J. Analysis and comparison of primary droplet characteristics in the near field of a prefilming airblast atomizer. In *Turbo Expo: Power for Land, Sea, and Air*, volume 55102, page V01AT04A002. American Society of Mechanical Engineers, 2013.

[101] Taylor, Geoffrey Ingram. "The shape and acceleration of a drop in a high speed air stream." *The scientific papers of GI Taylor*, 3: 457–464, 1963.

[102] O'Rourke, Peter J and Amsden, Anthony A. The tab method for numerical calculation of spray droplet breakup. Technical report, SAE technical paper, 1987.

[103] Poinsot, Thierry and Veynante, Denis. *Theoretical and numerical combustion*. RT Edwards, Inc., 2005.

[104] Bradley, Derek, Kwa, LK, Lau, AKC, Missaghi, M, and Chin, SB. "Laminar flamelet modeling of recirculating premixed methane and propane-air combustion." *Combustion and flame*, 71(2):109–122, 1988.

[105] Bradley, Derek and Lau, AKC. "The mathematical modelling of premixed turbulent combustion." *Pure and applied chemistry*, 62 (5):803–814, 1990.

[106] Bilger, RW. The structure of turbulent nonpremixed flames. In *Symposium (International) on Combustion*, volume 22, pages 475–488. Elsevier, 1989.

[107] Luche, J, Reuillon, M, Boettner, J-C, and Cathonnet, M. "Reduction of large detailed kinetic mechanisms: application to kerosene/air combustion." *Combustion science and technology*, 176(11):1935–1963, 2004.

[108] Van Oijen, JA, Donini, A, Bastiaans, RJM, ten Thije Boonkkamp, JHM, and De Goey, LPH. "State-of-the-art in premixed combustion modeling using flamelet generated manifolds." *Progress in Energy and Combustion Science*, 57:30–74, 2016.

[109] Galeazzo, Flavio Cesar Cunha, Prathap, Chockalingam, Kern, Matthias, Habisreuther, Peter, Zarzalis, Nikolaos, Beck, Christian, Krebs, Werner, and Wegner, Bernhard. Investigation of a flame anchored in crossflow stream of vitiated air at elevated pressures. In *Turbo Expo: Power for Land, Sea, and Air*, volume 44687, pages 1225–1233. American Society of Mechanical Engineers, 2012.

[110] Giusti, Andrea, Kotzagianni, Maria, and Mastorakos, Epaminondas. "Les/cmc simulations of swirl-stabilised ethanol spray flames approaching blow-off." *Flow, turbulence and combustion*, 97(4): 1165–1184, 2016.

[111] Smith, Gregory P., Golden, David M., Frenklach, Michael, Moriarty, Nigel W., Eiteneer, Boris, Goldenberg, Mikhail, Bowman, C. Thomas, Hanson, Ronald K., Song, Soonho, Gardiner, William C. Jr., Lissianski, Vitali V., and Zhiwei, Qin. Gri3.0 mechanism.

[112] Klarmann, Noah. *Modeling Turbulent Combustion and CO Emis-*

sions in Partially-Premixed Conditions Considering Flame Stretch and Heat Loss. Verlag Dr. Hut, 2019.

[113] Langone, Leonardo, Amerighi, Matteo, and Andreini, Antonio. "Large eddy simulations of a low-swirl gaseous partially premixed lifted flame in presence of wall heat losses." *Energies*, 15(3), 2022. ISSN 1996-1073. doi: 10.3390/en15030788. URL `https://www.mdpi.com/1996-1073/15/3/788`.

[114] Tang, Yihao and Raman, Venkat. "Large eddy simulation of premixed turbulent combustion using a non-adiabatic, strain-sensitive flamelet approach." *Combustion and Flame*, 234:111655, 2021.

[115] Donini, A, Bastiaans, RJM, Van Oijen, JA, and De Goey, LPH. "A 5-d implementation of fgm for the large eddy simulation of a stratified swirled flame with heat loss in a gas turbine combustor." *Flow, turbulence and combustion*, 98(3):887–922, 2017.

[116] Yadav, Rakesh, Verma, Ishan, Modak, Abhijit, and Li, Shaoping. A fully non-adiabatic flamelet generated manifold model for high fidelity modeling of turbulent combustion in gas turbine like conditions. In *Turbo Expo: Power for Land, Sea, and Air*, volume 84133, page V04BT04A026. American Society of Mechanical Engineers, 2020.

[117] Massey, James C, Chen, Zhi X, and Swaminathan, Nedunchezhian. "Modelling heat loss effects in the large eddy simulation of a lean swirl-stabilised flame." *Flow, Turbulence and Combustion*, 106(4): 1355–1378, 2021.

[118] Tay-Wo-Chong, Luis, Zellhuber, Mathieu, Komarek, Thomas, Im, Hong G, and Polifke, Wolfgang. "Combined influence of strain and heat loss on turbulent premixed flame stabilization." *Flow, Turbulence and Combustion*, 97(1):263–294, 2016.

[119] Tay-Wo-Chong, Luis, Scarpato, Alessandro, and Polifke, Wolfgang. Les combustion model with stretch and heat loss effects for predic-

tion of premix flame characteristics and dynamics. In *Turbo Expo: Power for Land, Sea, and Air*, volume 50848, page V04AT04A029. American Society of Mechanical Engineers, 2017.

[120] Zimont, Vladimir L, Lipatnikov, Andrei N, et al. "A numerical model of premixed turbulent combustion of gases." *Chem. Phys. Reports*, 14(7):993–1025, 1995.

[121] Schmid, Hans-Peter, Habisreuther, Peter, and Leuckel, Wolfgang. "A model for calculating heat release in premixed turbulent flames." *Combustion and Flame*, 113(1-2):79–91, 1998.

[122] Kutkan, Halit, Amato, Alberto, Campa, Giovanni, Ghirardo, Giulio, Tay Wo Chong, Luis, and Æsøy, Eirik. Modelling of turbulent premixed ch4/h2/air flames including the influence of stretch and heat losses. In *Turbo Expo: Power for Land, Sea, and Air*, volume 84942, page V03AT04A034. American Society of Mechanical Engineers, 2021.

[123] Klarmann, Noah, Sattelmayer, Thomas, Geng, Weiqun, Zoller, Benjamin Timo, and Magni, Fulvio. Impact of flame stretch and heat loss on heat release distributions in gas turbine combustors: Model comparison and validation. In *Turbo Expo: Power for Land, Sea, and Air*, volume 49767, page V04BT04A031. American Society of Mechanical Engineers, 2016.

[124] Klarmann, Noah, Sattelmayer, Thomas, Geng, Weiqun, and Magni, Fulvio. Flamelet generated manifolds for partially premixed, highly stretched and non-adiabatic combustion in gas turbines. In *54th AIAA Aerospace Sciences Meeting*, page 2120, 2016.

[125] Goodwin, David G, Moffat, Harry K, and Speth, Raymond L. "Cantera: An object-oriented software toolkit for chemical kinetics, thermodynamics, and transport processes." *Caltech, Pasadena, CA*, 124, 2009.

[126] Nassini, Pier Carlo, Pampaloni, Daniele, Meloni, Roberto, and Andreini, Antonio. "Lean blow-out prediction in an industrial gas turbine combustor through a les-based cfd analysis." *Combustion and Flame*, 229:111391, 2021.

[127] Meneveau, C and Poinsot, T. "Stretching and quenching of flamelets in premixed turbulent combustion." *Combustion and Flame*, 86(4): 311–332, 1991.

[128] Legier, Jean-Philippe, Poinsot, Thierry, and Veynante, Denis. Dynamically thickened flame les model for premixed and non-premixed turbulent combustion. In *Proceedings of the summer program*, volume 12. Citeseer, 2000.

[129] Fiorina, Benoit, Veynante, Denis, and Candel, Sébastien. Modeling combustion chemistry in large eddy simulation of turbulent flames. In *Eighth International Symposium on Turbulence and Shear Flow Phenomena*. Begel House Inc., 2013.

[130] Franzelli, Benedetta, Riber, Eleonore, Gicquel, Laurent YM, and Poinsot, Thierry. "Large eddy simulation of combustion instabilities in a lean partially premixed swirled flame." *Combustion and flame*, 159(2):621–637, 2012.

[131] Wang, Cheng, Qian, Chengeng, Liu, JianNan, and Liberman, Mikhail A. "Influence of chemical kinetics on detonation initiating by temperature gradients in methane/air." *Combustion and Flame*, 197:400–415, 2018.

[132] Franzelli, Benedetta, Riber, Eleonore, and Cuenot, Bénédicte. "Impact of the chemical description on a Large Eddy Simulation of a lean partially premixed swirled flame." *Comptes Rendus - Mecanique*, 341(1-2):247–256, 2013. ISSN 16310721. doi: 10.1016/j.crme.2012.11.007. URL `http://dx.doi.org/10.1016/j.crme.2012.11.007`.

[133] Celik, IB, Cehreli, ZN, and Yavuz, I. "Index of resolution quality for large eddy simulations." 2005.

[134] Gant, SE. Practical quality measures for large-eddy simulation. In *Direct and Large-Eddy Simulation VII*, pages 217–222. Springer, 2010.

[135] Rosenberg, David A, Allison, Patton M, and Driscoll, James F. "Flame index and its statistical properties measured to understand partially premixed turbulent combustion." *Combustion and Flame*, 162(7):2808–2822, 2015.

[136] Langone, Leonardo, Amerighi, Matteo, Mazzei, Lorenzo, Yadev, Rakesh, Orsino, Stefano, Ansari, Naseem, and Andreini, Antonio. Assessment of thickened flame model coupled with flamelet generated manifold on a low-swirl partially premixed gaseous lifted flam. In *Turbo Expo: Power for Land, Sea, and Air*. American Society of Mechanical Engineers, 2022. UNDER REVIEW.

[137] Dressler, L, Sacomano Filho, FL, Sadiki, A, and Janicka, J. "Influence of thickening factor treatment on predictions of spray flame properties using the atf model and tabulated chemistry." *Flow, Turbulence and Combustion*, 106(2):419–451, 2021.

[138] ANSYS. *Fluent 21.2 Theory Guide*, 2021.

[139] Kuenne, G, Ketelheun, A, and Janicka, J. "Les modeling of premixed combustion using a thickened flame approach coupled with fgm tabulated chemistry." *Combustion and Flame*, 158(9):1750–1767, 2011.

[140] Dressler, L, Ries, F, Kuenne, G, Janicka, J, and Sadiki, A. "Characterization of the stratification process in a turbulent premixed flame using les."

[141] Sacomano Filho, Fernando Luiz, Dressler, Louis, Hosseinzadeh, Arash, Sadiki, Amsini, and Krieger Filho, Guenther Carlos. "Investigations of evaporative cooling and turbulence flame interaction modeling in ethanol turbulent spray combustion using tabulated chemistry." *Fluids*, 4(4):187, 2019.

[142] Durand, Ludovic and Polifke, Wolfgang. Implementation of the thickened flame model for large eddy simulation of turbulent premixed combustion in a commercial solver. In *Turbo Expo: Power for Land, Sea, and Air*, volume 47918, pages 869–878, 2007.

[143] Charlette, Fabrice, Meneveau, Charles, and Veynante, Denis. "A power-law flame wrinkling model for les of premixed turbulent combustion part i: non-dynamic formulation and initial tests." *Combustion and Flame*, 131(1-2):159–180, 2002.

[144] Palanti, L, Puggelli, S, Langone, L, Andreini, A, Reveillon, J, Duret, Benjamin, and Demoulin, FX. "An attempt to predict spray characteristics at early stage of the atomization process by using surface density and curvature distribution." *International Journal of Multiphase Flow*, 147:103879, 2022.

[145] Hirt, Cyril W and Nichols, Billy D. "Volume of fluid (vof) method for the dynamics of free boundaries." *Journal of computational physics*, 39(1):201–225, 1981.

[146] Sussman, Mark, Smereka, Peter, and Osher, Stanley. "A level set approach for computing solutions to incompressible two-phase flow." *Journal of Computational physics*, 114(1):146–159, 1994.

[147]

[148] Ling, Yue, Zaleski, Stéphane, and Scardovelli, R. "Multiscale simulation of atomization with small droplets represented by a lagrangian point-particle model." *International Journal of Multiphase Flow*, 76:122–143, 2015.

[149] Chaussonnet, Geoffroy, Braun, Samuel, Wieth, Lars, Koch, Rainer, and Bauer, Hans-Jörg. Influence of particle disorder and smoothing length on sph operator accuracy. In *10th International SPHERIC Workshop*, page 8, 2015.

[150] Herrmann, Marcus. "A parallel eulerian interface tracking/lagrangian point particle multi-scale coupling procedure." *Journal of computational physics*, 229(3):745–759, 2010.

[151] Vallet, Ariane and Borghi, Roland. "Modélisation eulerienne de l'atomisation d'un jet liquide." *Comptes Rendus de l'Académie des Sciences-Series IIB-Mechanics-Physics-Astronomy*, 327(10):1015–1020, 1999.

[152] Lebas, Romain, Menard, Thibault, Beau, Pierre-Arnaud, Berlemont, Alain, and Demoulin, François-Xavier. "Numerical simulation of primary break-up and atomization: Dns and modelling study." *International Journal of Multiphase Flow*, 35(3):247–260, 2009.

[153] Anez, J, Ahmed, Aqeel, Hecht, N, Duret, B, Reveillon, Julien, and Demoulin, FX. "Eulerian–lagrangian spray atomization model coupled with interface capturing method for diesel injectors." *International Journal of Multiphase Flow*, 113:325–342, 2019.

[154] Ferrando, Diego, Palanti, Lorenzo, Demoulin, Francois-Xavier, Duret, Benjamin, and Reveillon, Julien. Spray drop size distribution and velocity distribution issued from a prefilming airblast atomizer. In *International Conference on Liquid Atomization and Spray Systems (ICLASS)*, volume 1, 2021.

[155] Ferrando, Diego Martìnez. *Advance numerical modeling of the atomization process: application to an aeronautical injection system. UNDER REVIEW*. PhD thesis, 2022.

[156] Puggelli, Stefano. *Towards a unified approach for Large Eddy Simulation of turbulent spray flames*. PhD thesis, Normandie Université; Università degli studi (Florence, Italie), 2018.

[157] Canu, Romain, Puggelli, Stefano, Essadki, Mohamed, Duret, Benjamin, Menard, Thibaut, Massot, Marc, Reveillon, Julien, and

Demoulin, FX. "Where does the droplet size distribution come from?" *International Journal of Multiphase Flow*, 107:230–245, 2018.

[158] Gepperth, Sebastian. *Experimentelle Untersuchung des Primärzerfalls an generischen luftgestützten Zerstäubern unter Hochdruckbedingungen*, volume 75. Logos Verlag Berlin GmbH, 2019.

[159] Kathrotia, Trupti, Riedel, Uwe, and Warnatz, Jürgen. A numerical study on the relation of oh*, ch*, and c2* chemiluminescence and heat release in premixed methane flames. In *Proceedings of the European combustion Meeting*, volume 2009, 2009.

[160] Nori, Venkata and Seitzman, Jerry. Chemiluminescence measurements and modeling in syngas, methane and jet-a fueled combustors. In *45th AIAA Aerospace Sciences Meeting and Exhibit*, page 466, 2007.

[161] Lauer, Martin and Sattelmayer, Thomas. "On the adequacy of chemiluminescence as a measure for heat release in turbulent flames with mixture gradients." *Journal of Engineering for Gas Turbines and Power*, 132(6), 2010.